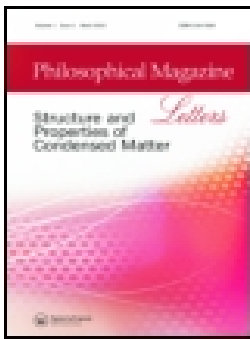# Addenda

Interrelated emission and spin–spin relaxation feature mediated by V_O^+ defects in Gd_2O_3 nanorods subjected to swift ion impact

Samiran Hazarika & Dambarudhar Mohanta

Published online: 17 May 2016.

Submit your article to this journal ↗

View related articles ↗

View Crossmark data ↗

Taylor & Francis
Taylor & Francis Group

Interrelated emission and spin–spin relaxation feature mediated by V_O^+ defects in Gd_2O_3 nanorods subjected to swift ion impact

Samiran Hazarika and Dambarudhar Mohanta [iD]

Nanoscience and Soft Matter Laboratory, Department of Physics, Tezpur University, Tezpur, India

ABSTRACT

We report on the manifestation and interconnected photolumin escence and electron paramagnetic resonance responses in gadolinium oxide (Gd_2O_3) nanorods subjected to 80 MeV carbon ion irradiation. On increasing the irradiation fluence between 1×10^{11} and 3×10^{12} ions/cm², the emission associated with neutral oxygen vacancies (V_{Ox}), positioned at ~350 nm, undergoes a steady increase compared to that associated with singly charged vacancies (V_O^+), located at ~414 nm. The enhancement of spin–spin relaxation time (τ_{ss}) is ascribed to a substantial changeover from V_O^+ to V_{Ox} defects with irradiation, the former being recognized as the major contributor to paramagnetic centres. Interconnected luminescence and spin–spin relaxation could provide insight for making advanced nanophosphors and spin valve elements.

1. Introduction

Rare-earth (RE) systems, both in pure and oxide form, are extensively used for making high-quality phosphors, superior catalysts, bio-medically relevant contrast agents, non-volatile memory and for constructing high-field RE magnets [1–4]. The growing interest in RE ceramics has taken place not only due to their high thermal, chemical and mechanical stability but also their radiation tolerant behaviour, which has great relevance in nuclear technology [5,6].

In the family of RE sesquioxides, gadolinium oxide (Gd_2O_3) finds a special place. As a contrast agent, it has great potential in advanced imaging technology [7]. Owing to higher molecular weight and shorter spin–lattice relaxation time, nanoparticles have recently emerged as alternative candidates over traditional gadolinium chelates in magnetic resonance imaging [7]. The significance of structural, morphological and optical characterization of nanoscale Gd_2O_3 systems, obtained through hydrothermal and polyol routes, has been described [8,9]. While 80 keV Ar^+ ion irradiation accounts for partial phase conversion along with the introduction of localized surface defects, 18 MeV photon irradiation was

---

CONTACT Dambarudhar Mohanta ✉ best@tezu.ernet.in

shown to create disorder-induced traps [10,11]. Unlike many conventional sulphides and oxides that exhibit nanoparticle coalescence under MeV-scale ion irradiation [12], or UV illumination [13], the RE oxides are largely radiation tolerant. Nevertheless, controlling surface defects by energetic irradiation is certainly interesting, especially when the system exists in one-dimensional form. Here, we explore the connection between defect-mediated optical emission and spin–spin relaxation associated with charged oxygen vacancies (V_O^+) in ion-irradiated Gd_2O_3 nanorod systems.

2. Experimental details

In principle, synthesizing Gd_2O_3 nanoparticles from its bulk counterpart and via a top-down approach is difficult owing to the extremely high thermal and mechanical stability of the system. However, an inexpensive solvo-hydrothermal route can be employed where the compound is first converted into a nitrate product ($Gd(NO_3)_3$) and subsequently reduced into its corresponding hydroxide ($Gd(OH)_3$) and oxide (Gd_2O_3) products [14]. In a typical procedure, 0.28 g of bulk Gd_2O_3 (Otto, 99.9% pure) is first dispersed in 35 ml deionized water followed by dropwise addition of dil. HNO_3 until a clear sol is obtained. The mixture is then transferred to a teflon-lined stainless steel autoclave after adjusting its pH to ~10, and latter subjected to oven heating at a temperature of ~140 °C, for 24 h. A white solid precipitate of $Gd(OH)_3$ is collected by filtering the precursor using a Whatman filter®. The resulting product is first washed with distilled water and then with ethanol several times and then oven dried at a temperature of ~80 °C. Finally, annealing of the hydroxide powder is performed at an elevated temperature (600 °C), for 3 h. The spontaneous decomposition and rapid dehydration of $Gd(OH)_3$ product is capable of creating Gd_2O_3 nanorods, collected in powder form.

The morphological and structural details can be revealed through transmission electron microscopy (TEM, JEOL JEM 2100) imaging and X-ray diffraction (XRD, Rigaku Miniflex, CuK_α, $\lambda = 1.543$ Å) measurements, respectively. For the irradiation experiments, the nanorods were first dispersed in a low molecular weight polyvinyl alcohol media with ~50% volume dispersion, and thin solid films (~40 μm) cast on laboratory-grade borosilicate glass substrates (1×1 cm²). We opted for 80-MeV carbon ion irradiation. The samples were irradiated in a high-vacuum chamber (pressure ~10^{-6} mbar) using 80 MeV C^{6+} ion beams (with a beam current of ~1 pnA, particle nanoampere) available from a 15UD tandem accelerator at the Inter University Accelerator Centre (IUAC), New Delhi. In order to ensure uniform irradiation condition, the ion beam was first scanned over a thick quartz plate of size 1×1 cm² fixed at the extreme end of the rectangular sample ladder. The ion fluence was chosen in the range of 1×10^{11}–3×10^{12} ions/cm². The energy of the ions was chosen such that their range (R_p) was high enough for them to pass completely through the target. The electronic energy loss S_e, the nuclear energy loss S_n and the range, R_p of the projectile ions were estimated with aid of the SRIM 2008 program [15], and are presented in Table 1.

Both un-irradiated and irradiated Gd_2O_3 nanorod samples were analyzed through two key techniques: photoluminescence (PL) spectroscopy and electron paramagnetic resonance (EPR) spectroscopy. The PL emission was measured with a PerkinElmer LS 55 luminescence spectrophotometer, and the EPR studies performed on a JES-FA200 ESR spectrometer working in the X band (~9.44 GHz) at a field modulation of 100 kHz, with a sensitivity of 7×10^9 spins/0.1 mT, and a resolution of 2.35 μT.

Table 1. Energy loss parameters in different systems for 80 MeV C^{6+} irradiation.

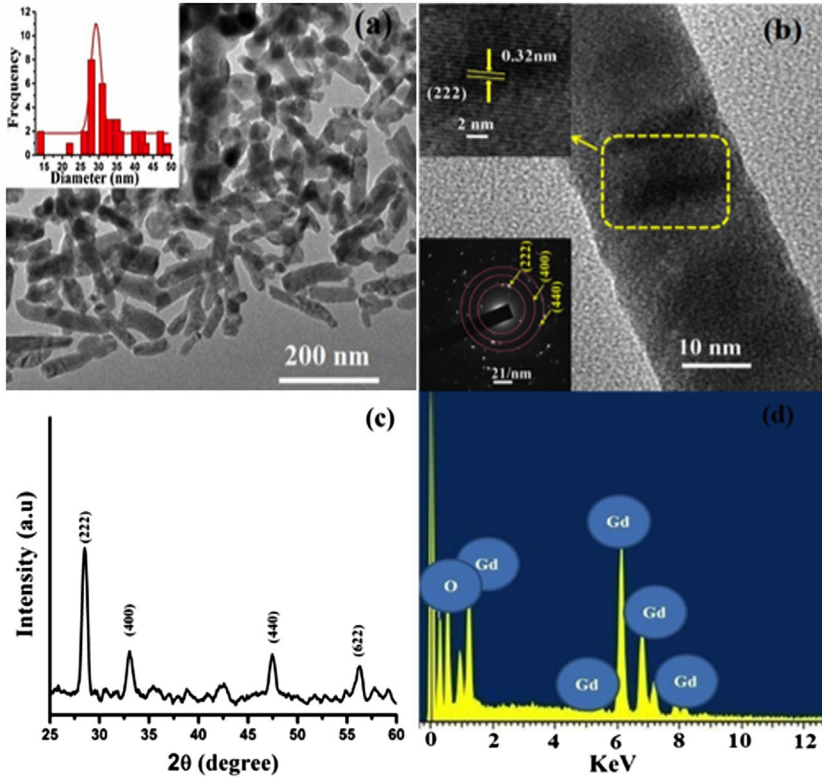| Material	S_e (eV/Å)	S_n (eV/Å)	Projectile range (μm)
PVA	27.91	1.528×10^{-2}	174.63
Gd_2O_3	78.31	4.319×10^{-2}	68.48

Figure 1. (a) TEM image of Gd_2O_3 nanorods, (b) magnified view of an isolated nanorod with zoomed view of a segment highlighting lattice fringe and defects. The SAED pattern that highlights diffused diffraction rings is shown as inset of (b). A powder XRD pattern and an EDX pattern illustrating crystal structure and composition are depicted in Figure (c) and (d), respectively.

3. Results and discussion

The development of one-dimensional Gd_2O_3 nanorods with an average diameter ~29 nm and length ~116 nm is evident from the TEM micrograph, depicted in Figure 1(a). A single nanorod with a lattice fringe pattern and a selected area electron diffraction (SAED) pattern is shown in Figure 1(b). The powder XRD pattern and EDX pattern of the nanorod system are presented in the lower panel of Figure 1. The diffractogram, shown in Figure 1(c), essentially represents a *C*-type cubic crystal structure (space group, *Ia*3) for the system and the most prominent (2 2 2) diffraction peak characterizing preferential orientation of the crystallites along the corresponding (JCPDS 12-0797) [16]. The EDX pattern on the other hand gave clear indication of Gd and O elements present in the system (Figure 1(d)).
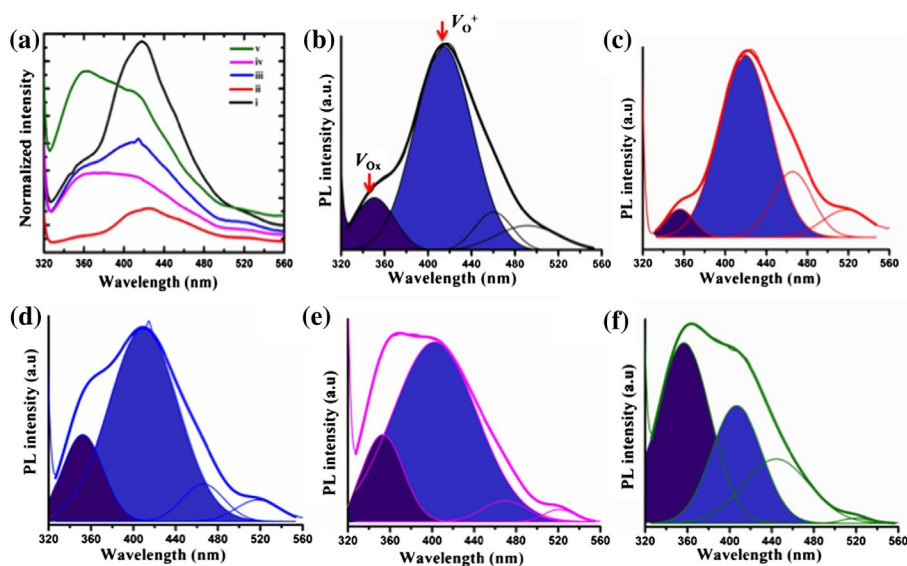
Figure 2. (a) PL spectra (λ_{ex} = 300 nm) of un-irradiated and irradiated Gd_2O_3 nanorod systems (i: 0, ii: 1×10^{11}, iii: 3×10^{11}, iv: 1×10^{12} and v: 3×10^{12} ions/cm²), and (b–f) deconvoluted PL spectra of the corresponding systems. Note the shadow areas under the curves representing mainly V_{Ox} and V_O^+ defects.

The room-temperature PL emission spectra (λ_{ex} = 300 nm) of the un-irradiated and irradiated Gd_2O_3 nanorods are depicted in Figure 2(a). The asymmetric nature of the luminescence spectra suggests that the overall trace is the superimposition of several peaks originating through different radiative events. In order to extract individual peaks, deconvolution was undertaken on the spectra by way of multi-peak Gaussian fitting employing OriginPro8.5˚ software. In the deconvolution process, the areas under the experimental and empirical curves are essentially the same. Although the strengths of the emissions were noticeably different for the pristine and irradiated nanorods, nearly unaltered emission positions could be identified for both (Figure 2(b)–(f)). The deconvoluted PL spectrum of the un-irradiated nanorods is shown in Figure 2(b), while the characteristic curves for irradiated nanorods are highlighted in Figure 2(c)–(f). The emission peak located at ~350 nm is attributed to neutral oxygen vacancies (V_{Ox}) [17]. The deep blue band positioned at ~414 nm is assigned to the recombination of delocalized electrons in the conduction band with a single charged state of surface oxygen vacancies (V_O^+), in accordance with the proposition of Wang et al. [18]. The blue emission responses at ~460 and ~491–518 nm arise from surface defects of Schottky and Frenkel types [17]. The second band is assigned to the introduction of closely spaced surface energy states within the forbidden gap arising from local departures from perfect periodicity and the introduction of degeneracy.

The characteristic signal strength, line width (peak-to-peak width i.e. ΔH_{p-p}), resonance field (H_R) and effective g (g_{eff}) values, corresponding to the un-irradiated and irradiated Gd_2O_3 nanorods, were evaluated from the first derivative EPR absorption spectra, shown in Figure 3(a) and (b). The observation of fairly broad, symmetric EPR spectra without a splitting signature discards the possibility of hyperfine splitting in the system under study. Moreover, the exchange interaction is expected to be small because in Gd^{3+} ions the inner
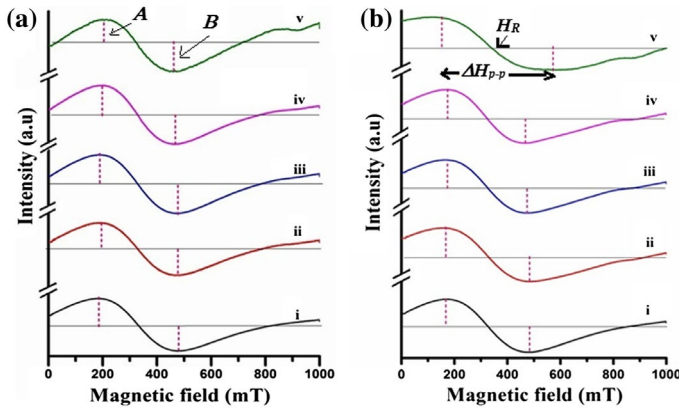
Figure 3. First-derivative EPR absorption spectra of the un-irradiated and irradiated Gd_2O_3 nanorods (i: 0, ii: 1×10^{11}, iii: 3×10^{11}, iv: 1×10^{12} and v: 3×10^{12} ions/cm^2) acquired at (a) 300 K and (b) 77 K.

Table 2. Characteristic parameters as predicted from the analysis of the EPR spectra.

	H_R (mT)		ΔH_{p-p} (mT)		g_{eff}		τ_{ss} (10^{-11} s)	
Ion fluence	RT (300 K)	LNT (77 K)	RT (300 K)	LNT (77 K)	RT (300 K)	LNT (77 K)	RT (300 K)	LNT (77 K)
0 (pristine)	331.25	325.63	294.52	311.82	2.037	2.014	3.13	3.06
1×10^{11}	328.94	327.94	284.72	328.85	2.052	2.009	3.26	2.96
3×10^{11}	327.5	325.88	289.61	311.25	2.061	2.012	3.24	3.07
1×10^{12}	326.34	325.88	268.85	295.67	2.068	2.012	3.37	3.24
3×10^{12}	321.73	344.80	257.89	451.73	2.098	1.902	4.32	2.66

$4f$ electrons are bound to the nucleus and shielded by the outermost electrons, $5s^25p^6$, via the crystal field [19]. The effective g-value can be calculated from the relation:

$$g_{eff} = hf / \mu_B H_R, \tag{1}$$

where f (= 9.44 GHz) is the frequency of the microwave source and μ_B is the Bohr magnetron. At room temperature (RT), the g_{eff} values of the pristine and irradiated (fluences: 0, 1×10^{11}, 3×10^{11}, 1×10^{12} and 3×10^{12} ions/cm^2) nanorods are estimated to be, ~2.037, 2.052, 2.06, 2.068 and 2.098 (Table 2). The liquid-nitrogen temperature (LNT) data, however, give corresponding g_{eff} values of 2.014, 2.009, 2.012, 2.012 and 1.902. It is worth mentioning here that, while values of $g_{eff} \geq 2$ mostly arise through spin contribution of holes, $g_{eff} < 2$ suggests surface electron contributions [20].

In all forms of spectroscopy, spectral lines are basically characterized by their signal strength (intensity), full width, and above all, position – ignoring occurrence of multiplets. While the intensity of EPR absorption is proportional to the concentration of paramagnetic species present in the system, the width of the resonance is dependent on the relaxation time of the spin state. If the line-width of the EPR signal is dictated by spin–lattice interaction, it should decrease with decreasing temperature [21]. Since we observed the opposite trend, yet similar to the EPR responses of Ce- and Gd-doped $NiFe_2O_4$ nanosystems [22], a dominant spin–spin relaxation is prevalent in our Gd_2O_3 nanorod-systems. The line-width of a typical EPR spectrum is given by:
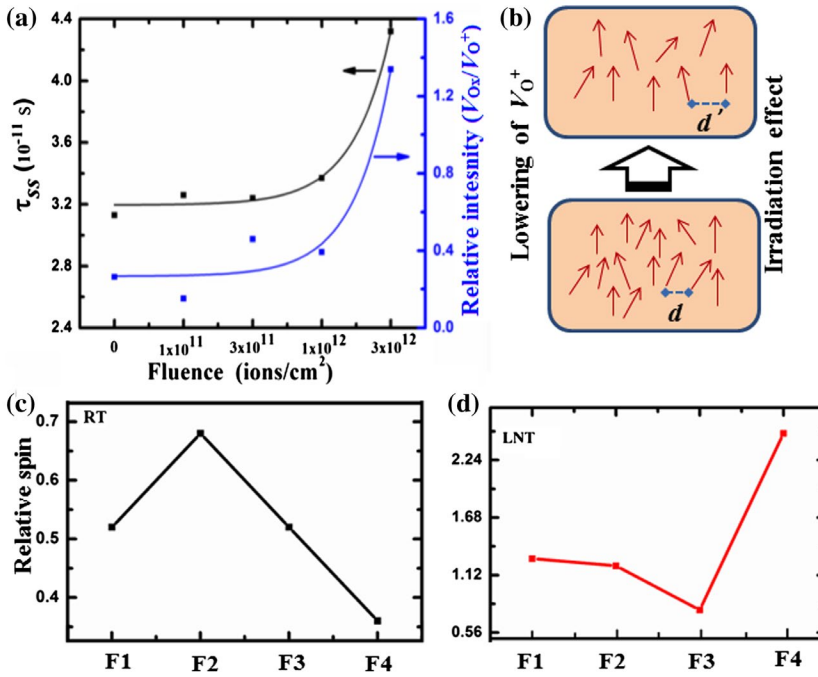
Figure 4. (a) Curves of relative PL intensity (V_{Ox}/V_O^+) and τ_{ss} with ion fluence, (b) schematic representation of V_O^+ mediated spin distribution ($d'>d$), d being the inter-spin separation in case of un-irradiated nanorods and d' that for irradiated systems. The spin factor was calculated with pristine sample as reference. The response of the irradiated nanorods, in RT and LNT environments, are highlighted in (c) and (d), respectively.

$$\Delta H_{p-p} \propto \tau_{sl}^{-1} + \tau_{ss}^{-1}, \tag{2}$$

where τ_{sl} and τ_{ss} represent spin–lattice and spin–spin relaxation time constants, respectively [21]. Normally, $\tau_{sl} > \tau_{ss}$ and τ_{ss} tend to decline with a reduction in spin–spin separation i.e. by increasing the spin concentration or paramagnetic centres. In the spin–spin relaxation process, the time constant τ_{ss} is normally determined from the peak-to-peak line width as [21,22],

$$\tau_{ss}^{-1} = \Delta H_{p-p}(\pi g/h)\mu_B. \tag{3}$$

Since intensity is directly linked to the concentration of paramagnetic centres, we evaluated the participation of V_O^+ in both PL emission and EPR absorption data. We plotted the relative PL intensity (V_{Ox}/V_O^+) of charged-to-neutral oxygen vacancies and spin–spin relaxation time as a function of ion fluence. The estimated τ_{ss} values, as for the room-temperature cases, are presented along with the relative PL intensity in Figure 4(a). The features, while exhibiting growing exponential trends, provide a direct connection between the PL and EPR results. An apparently growing trend of the 350 nm–414 nm emission peak intensity ratio with increasing ion fluence signifies an increase in neutral defects (V_{Ox}) over singly charged ones (V_O^+). It may be noted that, in wide-bandgap oxides, the presence of charged oxygen

vacancies and cationic interstitials contribute to donor states in the forbidden gap [23,24]. Here, we anticipate that the charged vacancies (V_O^+) become neutralized by free-electron capture during prolonged ion irradiation. Alternatively, a large suppression of the density of V_O^+ paramagnetic centres with increasing ion fluence would increase the inter-spin distance d, thereby enhancing the τ_{ss} values (Figure 4(b)). Even though the spin–spin relaxation is drastically suppressed at RT, the τ_{ss} values ($\sim 10^{-11}$s) are smaller at 77 K (LNT) than at RT (Table 2). This is because unpaired spins present in the Gd_2O_3 nanorod system experience slow relaxation at RT, but fast relaxation at LNT. A substantial amount of spins, which are impassive due to thermal agitation at RT, become active at LNT. A large reduction in spin–spin separation, and eventually fast relaxation, is quite feasible in a system with large spin concentrations that emerge from their unpaired existence. A comparison of relative spin factors in irradiated samples with respect to pristine ones, and estimated for RT and LNT environments, is shown in Figure 4(c) and (d).

4. Conclusion

The luminescence of the cubic-phase Gd_2O_3 nanorods exhibited several defect-related features, including those associated with neutral and charged oxygen vacancies. Upon irradiation, the V_O^+ defects, which appear as the source of paramagnetic centres, get suppressed, thereby increasing inter-spin separation. Accordingly, a higher magnitude of spin–spin relaxation time, τ_{ss} is realized on account of longer relaxation. In contrast, owing to repressed thermal agitation and active spins, the τ_{ss} values are lowered at LNT relative to those at RT. Interrelating PL and EPR features via paramagnetic defect centres can open up exciting avenues for understanding certain applications including advanced nanophosphors, luminescent elements and spin valve devices.

ORCID

Dambarudhar Mohanta http://orcid.org/0000-0002-1750-7620

References

[1] G. Kaur, S.K. Singh and S.B. Rai, J. Appl. Phys. 107 (2010) p.073514.
[2] G. Scheunert, W.R. Hendren, C. Ward and R.M. Bowman, Appl. Phys. Lett. 101 (2012) p.142407.
[3] D.J. Naczynski, M.C. Tan, R.E. Riman and P.V. Moghe, J. Mater. Chem. B 2 (2014) p.2958.
[4] J.-C. Wang, C.-T. Lin, C.-S. Lai and J.-L. Hsu, Appl. Phys. Lett. 97 (2010) p.023513.
[5] M. Tang, P. Lu, J.A. Valdez and K.E. Sickafus, J. Appl. Phys. 99 (2006) p.063514.
[6] K.E. Sickafus, R.W. Grimes, J.A. Valdez, A. Cleave, M. Tang, M. Ishimaru, S.M. Corish, C.R. Stanek and B.P. Uberuaga, Nat. Mater. 6 (2007) p.217.
[7] J.Y. Park, M.J. Baek, E.S. Choi, S. Woo, J.H. Kim, T.J. Kim, J.C. Jung, K.S. Chae, Y. Chang and G.H. Lee, ACS Nano. 3 (2009) p.3663.
[8] Z. Xu, J. Yang, Z. Hou, C. Li, C. Zhang, S. Huang and J. Lin, Mater. Res. Bull. 44 (2009) p.1850.
[9] R.M. Petoral Jr., F. Söderlind, A. Klasson, A. Suska, M.A. Fortin, N. Abrikossova, L. Selegård, P.O. Käll, M. Engström and K. Uvdal, J. Phys. Chem. C 113 (2009) p.6913.
[10] N. Paul, M. Devi and D. Mohanta, Mater. Res. Bull. 46 (2011) p.1296.
[11] H. García, S. Dueñas, H. Castán, A. Gómez, L. Bailón, R. Barquero, K. Kukli, M. Ritala and M. Leskelä, J. Vac. Sci. Technol. B 27 (2009) p.416.
[12] D. Mohanta, S.S. Nath, N.C. Mishra and A. Choudhury, Bull. Mater. Sci. 26 (2003) p.289.
[13] J. Sun, L.-H. Guo, H. Zhang and L. Zhao, Environ. Sci. Technol. 48 (2014) p.11962.
[14] H. Chen, C. He, C. Gao, Y. Ma, J. Zhang, X. Wang, S. Gao, D. Li, S. Kan and G. Zou, J. Phys.: Condens. Matter. 19 (2007) p.425229.
[15] J.F. Zeigler, M.D. Zeigler, J.P. Biersack and SRIM, *The Stopping and Range of Ions in Matter 2008*, 2008. Available at www.srim.org
[16] P. Du, L. Song, J. Xiong, Z. Xi, D. Jin and L. Wang, Nanotechnology 22 (2011) p.035602.
[17] N. Dhananjaya, H. Nagabhushana, B.M. Nagabhushana, B. Rudraswamy, S.C. Sharma, D.V. Sunitha, C. Shivakumara and R.P.S. Chakradhar, Spectrochim. Acta, Part A 96 (2012) p.532.
[18] C. Hu, H. Liu, W. Dong, Y. Zhang, G. Bao, and Z.L. Wang, Adv. Mater. 19 (2007) p.470.
[19] K. Srinivasulu, I. Omkaram, H. Obeid, A. Suresh Kumar, and J. L. Rao, J. Mol. Struct. 1036 (2013) p.63.
[20] R.F. Howe and M. Gratzel, J. Phys. Chem. 91 (1987) p.3906.
[21] D.M. Murphy, *EPR Spectroscopy of Polycrystalline Oxide Systems I: Metal Oxide Catalysis*, WILEY-VCH Verlag GmbH & Co. KGaA,Weinheim, 2009. ISBN: 978-3-527-31815-5.
[22] G. Dixit, J.P. Singh, R.C. Srivastava and H.M. Agrawal, J. Magn. Magn. Mater. 324 (2012) p.479.
[23] M.D. McCluskey and S.J. Jokela, J. Appl. Phys. 106 (2009) p.071101.
[24] B. Lin, Z. Fu and Y. Jia, Appl. Phys. Lett. 79 (2001) p.943.

Oriented attachment (OA) mediated characteristic growth of Gd$_2$O$_3$ nanorods from nanoparticle seeds

Samiran Hazarika, Dambarudhar Mohanta[*]

(Nanoscience and Soft Matter Laboratory, Department of Physics, Tezpur University, PO: Napaam, Assam 784028, India)

Abstract: Herein, we demonstrated the oriented attachment (OA) driven formation and characterization of Gd$_2$O$_3$ nanorods. The nanorods were synthesized via a surfactant free, inexpensive hydrothermal route and considering ~30 nm nanoparticles as the seed. While maintaining a cubic phase throughout the process, complete transformation of Gd$_2$O$_3$ nanoparticles to nanorods was found to occur at an elevated temperature (~180 ℃) of the hydrothermal reaction. The elongated Gd$_2$O$_3$ nanostructures, as revealed from transmission electron microscopic imaging, possessed an average diameter of ~33 nm and an approximate length of 172 nm. From the kinetics of OA process, the activation energy of formation was estimated to be ~25 kJ/mole. The existence of defect mediated radiative emission was ascertained from the asymmetric broadening of luminescence spectra. The defect emission arising from the Gd$_2$O$_3$ nanorods was nearly 1.4 times stronger than that of nanoparticles. The morphological evolution and growth kinetics were discussed along with the luminescence and electron paramagnetic resonance features.

Keywords: nanorod; hydrothermal; oriented attachment; rare-earth oxide

One dimensional (1D) nanostructured systems, such as, nanorods, nanotubes, nanowires have shown their immense potential in various fields of modern technology[1–3]. In particular, nanorods belong to the class of regular elongated structures that retain an axial symmetry, and with the characteristic property largely governed by the aspect ratio and associated surface defects. Being environmentally stable system, the rare-earth oxides (REOs) have wide spread application in the manufacturing of high field tiny magnets, high performance luminescent devices, as well as in biomedical fields. The REOs display unique electronic, optical and luminescence properties that arise from the shielded 4f electrons. In the past, nanoparticles and nanostructures of other morphologies have been synthesized via different user-friendly routes[4,5]. Knowing that, aligned ZnO nanorods exhibit polarized luminescence characteristics, REOs, which exhibit select *D-F* mediated radiative emission, can also warrant polarized luminescence characteristics when available in vertically aligned form. Moreover, the REO nanoparticle based novel ferrofluids form the basis of radiation resistant rheological responses[6,7]. The RE sesquioxide Gd$_2$O$_3$ is a well-known, industrially relevant system owing to its superb thermal stability, chemical durability, high refractive index, etc.[8]. Recently, we have demonstrated an enhanced linear dichroism and rheological behavior of gamma-irradiated Gd$_2$O$_3$ nanoparticle based ferrofluids[6,9]. As an efficient contrast agent for magneto resonance imaging (MRI), Gd$_2$O$_3$ nanoparticles are capable of displaying an improved relaxivity over Gd-based chelates[10]. In so far as development of 1D structures is concerned, numerous techniques have been employed which included solid-vapor process[11], laser vaporization method[12], hydrothermal treatment[13], etc.

Essentially, particle growth in most of the nanostructured systems is described through Ostwald ripening mechanism[14,15], and 1D growth is no exception to it. Any sort of elongation is believed to be due to the assimilation of seed crystals along the most preferred direction to minimize the surface energy of the overall system. In this report, we made an attempt to reveal the growth mechanism of the hydrothermally processed Gd$_2$O$_3$ nanorods using nanoparticles as the seed element. The growth kinetics was discussed in light of oriented attachment (OA) mechanism. The morphological evolution and luminescence features were also highlighted in this work.

1 Experimental

At first, gadolinium acetate hydrate [Gd(CH$_3$CO$_2$)$_3$.H$_2$O] (CDH, 99.9% pure) was dispersed in deionized water and then, citric acid [C$_6$H$_8$O$_7$] (CDH 99% pure) was added to prepare a 1:1 molar ratio solution. Then the mixture was subjected to vigorous stirring (~300 r/min)

for 30 min which was followed by filtration. The product was further sintered at 800 ºC in a tubular furnace for 4 h to yield Gd_2O_3 nanoparticles (GNP).

In the next step, 0.15 g of the synthesized GNP was dispersed in 35 mL distilled water. The pH was adjusted to ~10 by adding aq. NaOH in a dropwise manner. The mixture was then transferred to a teflon-lined stainless autoclave and subjected to oven-heating (for 24 h), while maintaining a temperature of 140 and 180 ºC, for two separate cases. A white solid precipitate of Gd_2O_3 was then collected by filtering the precursor by using a Whatman filter®. The as-received product was washed several times, first with distilled water and then with ethanol, and oven-dried at a temperature of 80 ºC. In order to remove away all the hydroxyl groups present in the system, the powder was finally calcined at a temperature of 600 ºC for 3 h. The hydroxyl-free Gd_2O_3 nanorods (GNR) were kept ready for subsequent experimentation. The block diagram of the complete synthesis procedure is illustrated in Fig. 1.

The crystallographic information was revealed by a Rigaku miniFlex X-ray diffractometer (XRD) that employs a Cu Kα source (λ=0.1543 nm). The diffraction angle (2θ) was varied in the range of 20º–60º and with a step of 0.05º. Transmission electron microscopy (TEM) images were obtained from a JEOL JEM 2100 machine, operating at an accelerating voltage of 200 kV. The room temperature photoluminescence emission and electron paramagnetic resonance data have been acquired by using a PerkinElmer LS 55 spectrophotometer and a JEOL: JESFA200 EPR spectrometer, respectively.

2 Results and discussion

The structural and morphological features, along with nanorod growth mechanism are as detailed below.

2.1 Structural and morphological analysis

Fig. 2(a) shows a set of XRD patterns of the as-synthesized samples of Gd_2O_3 nanoparticles, and hydrothermally processed nanorods at different temperatures. In each case, the diffraction peaks characterize cubic

phase of the Gd_2O_3 system[16]. The distinct peaks corresponded to (222), (400), (440) and (622) crystallographic planes of the samples under investigation. Moreover, we noticed a shifting of peaks towards a lower diffraction angle in case of Gd_2O_3 nanorods as compared to the particles. The shifting of peak position towards a lower diffraction angle would indicate enhancement of lattice parameters[17]. Since here (222) appeared as the most intense peak, most of the crystallites have preferred orientation along the said plane. Moreover, the average crystallite size (d) and microstrain (η) can be calculated from the popular Williamson-Hall (W-H) expression: $\beta\cos\theta = 0.9\lambda/d + 4\eta\sin\theta$, which normally represents the equation of a straight line[16]. The GNP system gives an average size (d) estimation of ~11.8 nm. Whereas, hydrothermally derived GNRs that are processed at a temperature of 140 and 180 ºC, and post-calcined at a temperature of 600 ºC offered an average crystallite size of ~12 and 14 nm; respectively. Without calcination, the GNRs experienced a relatively lower size of ~8 nm (Fig. 2(a) and Table 1). Using the diffraction equation valid for a cubic system ($d_{hkl} = a/\sqrt{h^2 + k^2 + l^2}$), the lattice parameter, a is estimated to be 1.077, 1.086, 1.091 and 1.086 nm for GNP, GNR without calcination and GNRs prepared at 140 and 180 ºC followed by calcination at a higher temperature. (Table 1). It may be noted that, particle-size dependent lattice expansion is quite common in numerous metal oxides including ABO_3 and ABO_4 types[18,19]. According to these works, the lattice expansion is due to a proportionately large content of surface defect dipoles which could improve the negative surface stress with the particle size reduction. On the contrary, in our hydrothermally processed Gd_2O_3 nanostructures, we observed an increased lattice parameter with increasing crystallite size. Our results are consistent to those of a recent article by Yang and coworkers on $GdVO_4$:Eu^{+3} system[20]. It was proposed that, calcination driven reduced negative surface stress can lead to the desired change.

Fig. 2(b), (c) and (d) depict the HRTEM images of Gd_2O_3 nanoparticles and nanorods synthesized at 140 and 180 ºC; respectively. The average size of the nanoparticles, as
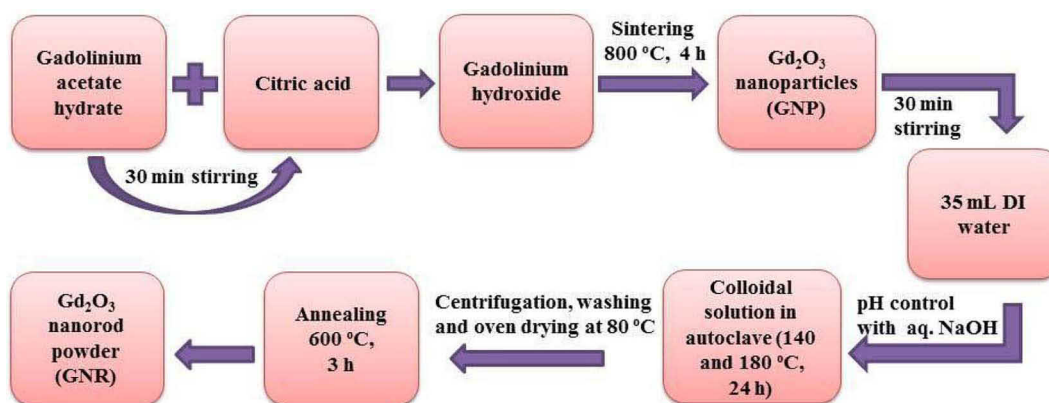

Fig. 1 Block diagram that highlights various steps involved in the synthesis of Gd_2O_3 nanorods
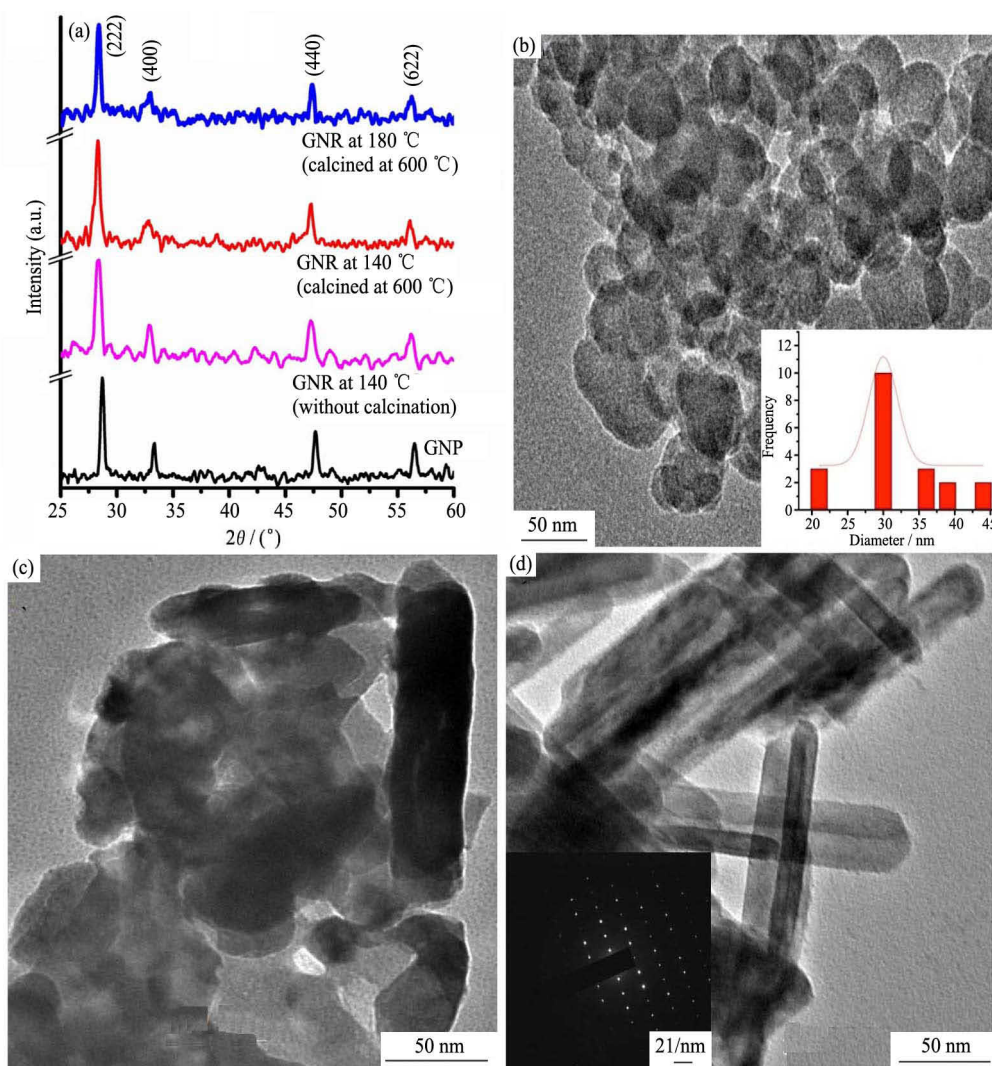
Fig. 2 XRD patterns of all the Gd$_2$O$_3$ samples (a), HRTEM images of Gd$_2$O$_3$ seed nanoparticles (b), and nanorods synthesized at a processing temperature of 140 ℃ (c), and 180 ℃ (d) (The feature shown in (d), characterize well developed nanorods with instances of hollow morphology. The SAED pattern is depicted in the inset of (d))

Table 1 Physical characteristics estimated from XRD and PL responses

Sample	Average crystallite size (d)/ nm	Micro-strain (η) (10^{-3})	Lattice parameter ($a=b=c$)/nm	Symmetry factor (Δ_R/Δ)
GNP	11.8	−2.2	1.077	0.55
GNR 140 ℃	8.0	−5.4	1.086	–
GNR 140 ℃ (calcined at 600 ℃)	12	−3.8	1.091	0.57
GNR 180 ℃ (calcined at 600 ℃)	14	−1.7	1.086	0.58

found from the micrograph, is ~30 nm (Fig. 2(b)). The sample processed at a temperature of 140 ℃ contained only a few fully grown nanorods along with many underdeveloped rods (Fig. 2(c)). While exhibiting an approximate diameter of 32 nm, nanorods as large as 170 nm could be achieved. However, the GNR sample prepared at a temperature of 180 ℃, contained a number of fully grown nanorods with occasional hollow appearances that

are evident from Fig. 2(d). The average length of the nanorods was found to vary in the range of ~155–190 nm and diameter ~33 nm (Fig. 2(d)). The inset of Fig. 2(d) basically depicts a selected area electron diffraction (SAED) pattern that highlight equi-spaced bright spots arranged in a cubic lattice. We anticipate mono-crystalline nature of the GNRs synthesized at 180 ℃.

The presence of fully evolved nanorods at an elevated hydrothermal temperature is attributed to the oriented attachment mechanism[21]. The formation of 1D nanostructure with a higher aspect ratio is essentially possible in presence of higher concentration of OH⁻ ions[22]. The reaction temperature is another factor which could affect the aspect ratio of Gd$_2$O$_3$ nanoscale structures. It is worth mentioning here that, NaOH or KOH plays an important role in the growth of 1D nanorods. The pH dependent study of Gd$_2$O$_3$ can be found in the literature[23]. A number of patterns, such as nanospheres, nanorods, nanowires, etc., have been grown through hydrothermal route and with pH control[23,24]. Plate-type morphology

are obtained for pH<7, whereas nanorods and nanowires are invariably developed at high pH values. Recently, we have also succeeded in fabricating Gd$_2$O$_3$ nanorods via a catalyst-free hydrothermal approach[25]. The effect of pH has been discussed along with the growth mechanism of nanorods and apparently, nanorods with high aspect ratios can be revealed in environment of high pH media. The addition of NaOH and KOH has also been found to help control the phase and morphology of octahedral Fe$_3$O$_4$ crystals as well as α-Fe$_2$O$_3$ platelets[26,27].

2.2 Growth mechanism mediated via oriented attachment

The growth mechanism of Gd$_2$O$_3$ nanorods is schematically shown in Fig. 3(a). The corresponding TEM imaging can be found in the lower panel of the same figure. Since the Gd$_2$O$_3$ nanorods are synthesized from Gd$_2$O$_3$ nanoparticles, we speculate that particle growth would occur along a themodynamically favorable direction. Previously, melting assisted particle growth was observed due to swift ion impact as well as prolonged sintering[28,29]. In either case, particle growth was believed to be accompanied by Ostwald ripening (OR) mechanism. In general, particles obtained by OR mechanism have regular shape and the surface defects produced during growth vanish with the particle dissolution. However, since the model is purely based on the equilibrium condition between the solubilization and precipita-

Fig. 3 (a) Schematic growth mechanism of Gd$_2$O$_3$ nanorods (upper panel); (b) A set of TEM images illustrating transformation of nanoparticle seeds to nanorods through oriented attachment (lower panel); (c) Arrhenius plot of the reaction constant k vs. inverse of temperature, T^{-1}

tion, and less amount of solubility is involved at the nanoscale level, an alternative strategy needs to be adopted. At nanoscale level the growth mechanism, under special circumstance, can be governed by oriented attachment (OA) mechanism[30]. Typically, OA mechanism is based on three factors: (1) dipole-dipole interaction that causes two oriented particles to get attached, (2) interaction prevails until perfect lattice match is ensured and (3) the adjoining interface eventually vanishes resulting in a single crystal particle[31]. In other words, the nanorod structures can be produced by energetically favorable alignment and coalescence of neighboring particles through elimination of the common boundary. This is clearly evident from the micrographs placed in the middle of the lower panel, shown in Fig. 3(b). The adjoining particles are indicated by dashed- yellow regions, and the interfaces, indicated by arrow marks in the magnified image.

Since the surface energy plays an important role in the crystal growth process, the growth of elongated nanostructures can occur by lowering the surface energy along a specific direction. The driving force of anisotropic growth of nanostructures is the crystal surface reactivity[32]. In general, Gd$_2$O$_3$ is a known REO system and possess a cubic crystal structure. Moreover, it is difficult to grow anisotropic nanostructures through classical OR mechanism. Previously, the OA mechanism was used to describe the growth process in different oxide systems, such as, TiO$_2$[33], CdTe[34], and Y$_2$O$_3$[32]. In the present situation, at first, the cubic Gd$_2$O$_3$ nanoparticles aggregate due to dipole-dipole interactions, fused gradually and then, recrystallize into single crystalline nanorods. It may be noted that, growth of the nanorods is neither surfactant assisted nor template based but purely governed by dipole-dipole interaction caused by OA.

Under hydrothermal treatment, nanoparticles are randomly oriented following Brownian motion. When two adjacent primary particles collide, the coalescence occurs and that, the particles share a common crystallographic orientation. Thus the two primary particles attach to each other and combine into a secondary one which is still very small and continue to collide and coalesce. The repetition of such an organized event leads to directed assimilation of particles, resulting in rod shaped structures. The kinetic model governed by OA mechanism can be described by the following reaction[35]:

$$A_1 + A_1 \xrightarrow{\ k\ } B \tag{1}$$

where A_1 is a primary nanoparticle, B is the product of the coalescence of two primary nanoparticles and k is the rate constant involved in the reaction between two particles.

Essentially, reaction occurs between the primary nanoparticles (monomer), whereas nanorods are the collective outcome of the repetitive events. The kinetic
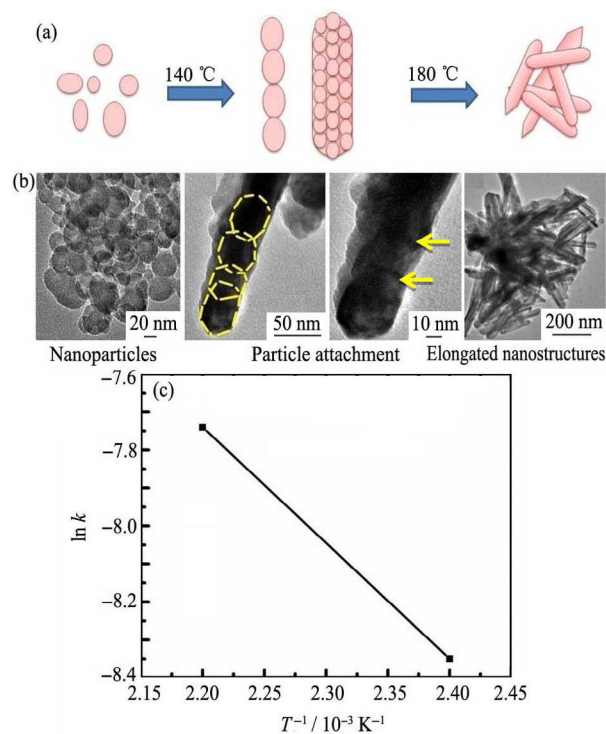
model for OA mechanism can be formulated by[35],

$$d_t = \frac{d_0(\sqrt[3]{2}kt+1)}{kt+1} \qquad (2)$$

Here, d_0 is the diameter of the precursor nanoparticles, d_t the diameter of the as grown nanocrystals at time t and k the reaction constant. The values of k can be calculated for both the reaction temperatures, 140 and 180 ºC. In the first case, substituting d_t=32 nm, d_0=30 nm and t=1440 min, in Eq. (2), k is calculated to be 2.36×10^{-4} min^{-1}. Using similar kinetics, the rate constant is found to be 4.34×10^{-4} min^{-1} for GNRs synthesized at an elevated temperature of 180 ºC (diameter, d_t≈33 nm). Note that, for evaluating k, we have not considered the whole length of the nanorods but diameter of the nanorods as predicted from the TEM analyses. This is because, fully grown elongated structures coexist with the under-developed structures that would represent different stages of growth. The formation of nanorods is believed to be as a result of directed-multi step OA processes dictated by Eq. (2). In order to explore the relationship between the kinetic constant, k and the reaction temperature, T, the Arrhenius equation can be considered which is given by[35],

$$\ln k = -\frac{E_a}{RT} + \ln A \qquad (3)$$

where A is the pre-exponential factor, E_a is the activation energy and R is the universal gas constant (8.314 J/mol/K). In general, the Arrhenius equation describes the temperature dependence of the rate constant during a chemical reaction. Considering GNP as the base material, one can use the above relation in order to calculate activation energy involved in GNRs, synthesized at different processing temperatures. By plotting calculated k values in log scale vs. $1/T$, we obtained a trace as depicted in Fig. 3(c). The activation energy involved in the transformation of nanoparticles (GNP) to nanorods (GNR) mediated via hydrothermal treatment can be estimated from the slope and is found as, 25.3 kJ/mol. As predicted earlier, (222) crystallographic plane that corresponded to the most dense (111) plane in the cubic cell can become responsible for the preferential growth owing to minimum surface energy conformation[36]. We anticipate that, nanorod growth, in the present case, is preceded along this plane following multi OA events in an organized manner (Fig. 3(a)).

2.3 Photoluminescence and EPR studies

The room temperature photoluminescence spectra of the synthesized samples (λ_{ex}=300 nm) are shown in Fig. 4(a). The spectra of all the samples are characterized by
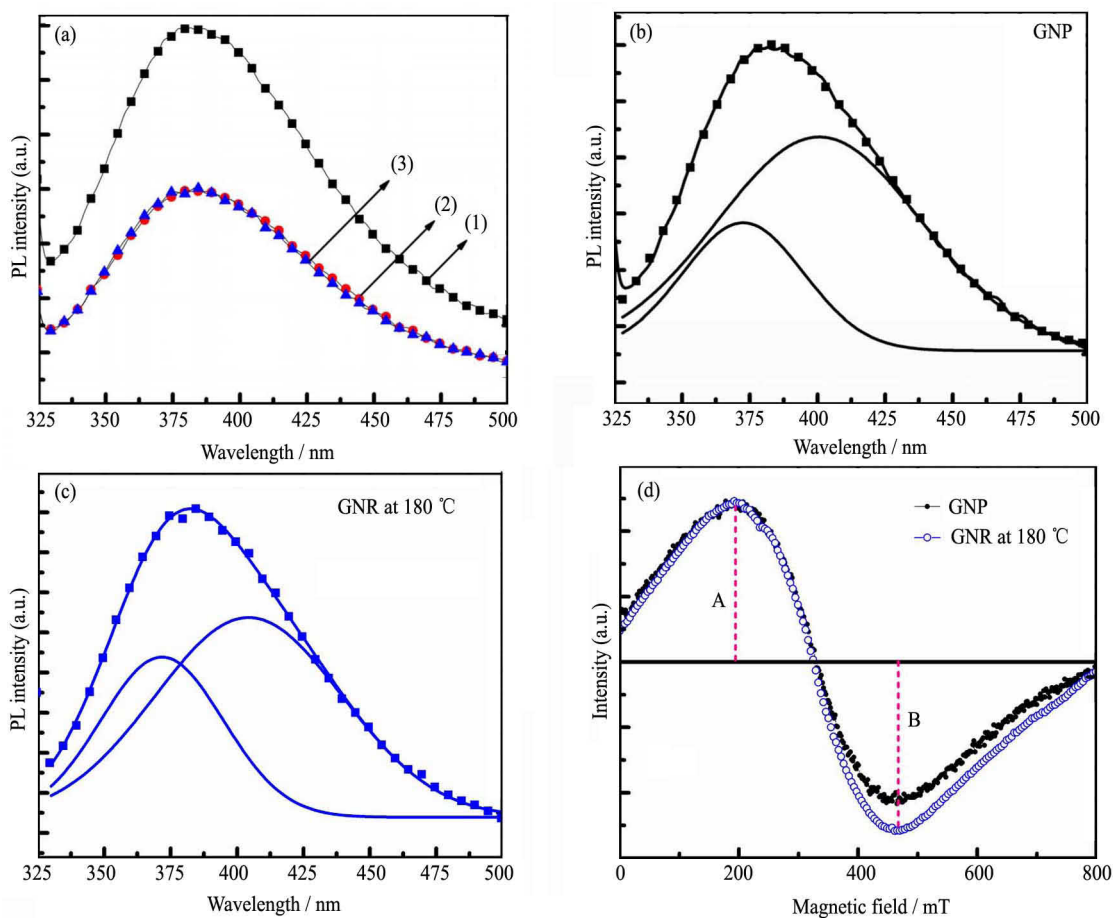

Fig. 4 (a) PL emission spectra of different Gd$_2$O$_3$ samples: nanoparticles (GNP) (1), and hydrothermally processed nanorods (GNR) at a temperature of 140 ºC (2) and 180 ºC (3); (b, c) The deconvoluted PL curves of GNP and GNR systems separately; (d) Room temperature EPR spectra of the corresponding GNP and GNR systems

an intense emission located at ~373 nm. This peak can be attributed to the recombination of a delocalized electron close to the conduction band with a single charged state of the surface oxygen vacancy according to the proposition made by Wang et al. and Zhang et al.[37,38]. The overall luminescence response of the GNRs is found to be less intense with respect to the GNP counterpart. The deconvoluted PL spectra of the GNP and the GNR (processed at a temperature of 180 ℃) are shown in Fig. 4(b) and (c), respectively. Upon deconvolution, an intense defect emission peak can be found at ~405 nm. After assessment of all the spectra, the intensity ratio between ~373 and 405 nm peaks, is observed to be nearly 1.4 times larger in GNRs than that of GNPs. Not surprisingly, it is the defect mediated emission which is mainly responsible for causing asymmetry in the PL spectra. The right symmetry factor (Δ_R/Δ), as defined by the ratio of the wavelength share on the right side of the peak maxima to the full width wavelength at half maxima, is slightly improved with the processing temperature (Table 1). Furthermore, a high concentration of dislocations and point defects can be anticipated when two particles merged into one eliminating the interface in OA process[39]. We invoke that, transformation of particles to nanorods may not necessarily offer new kinds of defects but the latter system is likely to possess ample defect centers that give rise to significant recombination events.

Electron paramagnetic resonance (EPR), often referred to as electron spin resonance (ESR), is a widely used spectroscopic technique to study paramagnetic centers on various oxide surfaces[40]. The room temperature, first derivative EPR spectra of the GNP and GNR (processed at 180 ℃) systems were recorded in the X-band (9.37 GHz) of the electromagnetic spectrum and with a field modulation of 100 kHz. The variation of signal intensity with the magnetic field is shown in Fig. 4(d). The effective *g* value was determined from the relation

$$g_{eff} = \frac{hf}{\mu_B H_R} \tag{4}$$

where *f* is the frequency (~9.37 GHz) of the microwave source, μ_B the Bohr magnetron and H_R the resonant magnetic field. A fairly symmetric nature can be evident for each of the spectra, with resonance fields centered at 328.9 and 330 mT, as for GNP and GNR systems; respectively. The effective *g* value is calculated to be ~2.02, which can account for effective hole trapping in the system (*g*>2). The respective asymmetry parameters (A/B ratio) for the GNP and GNR systems are ~1.2 and 1. Though vast number of defect types could influence the EPR spectra drastically, presence of adequate point defects (say, oxygen vacancies) at the edge boundaries keep the spectra symmetric with no further splitting and additional doublet[41]. At this juncture, it is difficult to correlate EPR results with PL spectra owing to the non-availability of detailed picture of charged defects, donor and acceptor kinds. However, such an investigation can be made on GNRs subjected to ion irradiation and with a controlled fluence variation. A detailed study in this direction is in progress.

3   Conclusions

The cubic phase, Gd₂O₃ nanorods were synthesized via a surfactant free hydrothermal method. Mediated by oriented attachment (OA) mechanism, a complete growth of nanorods was realized when the hydrothermal reaction was carried out at a temperature of 180 ℃. The nanorods were expected to have formed through multi-step OA, accompanied with an activation energy of 25 kJ/mol. The asymmetry nature of the photoluminescence curve accounted for the intense defect mediated emission located at ~405 nm. As compared to the Gd₂O₃ nanoparticles, though the overall emission in case of nanorods was less intense, the defect emission response to that of recombination emission via delocalized electrons close to the conduction band, was marginally enhanced. The EPR spectrum of the nanorods was more isotropic than that of the nanoparticles, while both gave g_{eff}>2. Apart from interrelated defect emission and spin-spin relaxation characteristics, more investigations with respect to aspect ratio dependent EPR responses would certainly shed light on spin-spin and spin-lattice relaxation contributions in different temperature environments.

References:

[1] Xia Y N, Yang P D, Sun Y G, Wu Y Y, Mayers B, Gates B, Yin Y D, Kim F, Yan H. One dimensional nanostructures: synthesis, characterization and application. *Adv. Mater.*, 2003, **15**(5): 353.

[2] Jin R, Cao Y W, Mirkin C A, Kelly K L, Schatz G C, Zheng J G. Photoinduced conversion of silver nanospheres to nanoprisms. *Science*, 2001, **294**(5548): 1901.

[3] Wu Y L, Xu X Z, Li Q L, Yang R C, Ding H X, Xiao Q. Synthesis of bifunctional Gd₂O₃:Eu³⁺ nanocrystals and their applications in biomedical imaging. *J. Rare Earths*, 2015, **33**(5): 529.

[4] Abdullah M M, Rahman M M, Bouzid H, Faisal M, Khan S B, Al-Sayari S A, Ismail A A. Sensitive and fast response ethanol chemical sensor based on as-grown Gd₂O₃ nanostructures. *J. Rare Earths*, 2015, **33**(2): 214.

[5] Jia G, Liu K, Zheng Y H, Song Y H, Yang M, You H P.

Highly uniform $Gd(OH)_3$ and $Gd_2O_3:Eu^{3+}$ nanotubes: Facile synthesis and luminescence properties. *J. Phys. Chem. C*, 2009, **113**(15): 6050.

[6] Paul N, Hazarika S, Saha A, Mohanta D. Optical emission, vibrational feature, and shear-thinning aspect of Tb^{3+}-doped Gd_2O_3 nanoparticle-based novel ferrofluids irradiated by gamma photons. *J. Appl. Phys.*, 2013, **114**(13): 134903.

[7] Paul N, Mohanta D, Saha A. Optical and rheological study of gamma irradiated rare-earth nanoparticle based ferrofluids. *Nucl. Instrum. Methods B*, 2012, **292**: 45.

[8] Guo H, Dong N, Yin M, Zhang W P, Lou L R, Xia S D. Visible upconversion in rare earth ion-doped Gd_2O_3 nanocrystals. *J. Phys. Chem.*, 2004, **108**(50): 19205.

[9] Paul N, Devi M, Mohanta D, Saha A. Magnetically induced optical activity and dichroism of gadolinium oxide nanoparticle-based ferrofluids. *J. Appl. Phys.*, 2012, **111**(4): 044904.

[10] Park J Y, Baek M J, Choi E S, Woo S, Kim J H, Kim T J, Jung J C, Chae K S, Chang Y, Lee G H. Paramagnetic ultrasmall gadolinium oxide nanoparticles as advanced T_1 MRI contrast agent: Account for large longitudinal relaxivity, optimal particle diameter, and *in Vivo* T_1 MR images. *ACS Nano.*, 2009, **3**(11): 3663.

[11] Pan Z W, Dai Z R, Wang Z L. Nanobelts of semiconducting oxides. *Science*, 2001, **291**(5510): 1947.

[12] Zhou Y, Yu S H, Cui X P, Wang C Y, Chen Z Y. Formation of silver nanowires by a novel solid-liquid phase arc discharge method. *Chem. Mater.*, 1999, **11**(3): 545.

[13] Du G, Tendeloo G V. Preparation and structure analysis of $Gd(OH)_3$ nanorods. *Nanotechnology*, 2005, **16**(4): 595.

[14] Baldan A. Review: Progress in Ostwald ripening theories and their applications to nickel-base superalloys, Part I: Ostwald ripening theories. *J. Mater. Sci.*, 2002, **37**(11): 2171.

[15] Joesten R L. Kinetics of coarsening and diffusion-controlled mineral growth. *Rev. Mineral.*, 1991, **26**(1): 507.

[16] Hazarika S, Mohanta D. Production and optoelectronic response of Tb^{3+} activated gadolinium oxide nanocrystalline phosphors. *Eur. Phys. J. Appl. Phys.*, 2013, **62**(3): 30401.

[17] Ningthoujam R S, Shukla R, Vatsa R K, Duppel V, Kienle L, Tyagi A K. $Gd_2O_3:Eu^{3+}$ particles prepared by glycine-nitrate combustion: Phase, concentration, annealing, and luminescence studies. *J. Appl. Phys.*, 2009, **105**(8): 084304.

[18] Akdogan E K, Rawn C J, Porter W D, Payzant E A, Safari A. Size effects in $PbTiO_3$ nanocrystals: effect of particle size on spontaneous polarization and strains. *J. Appl. Phys.*, 2005, **97**(8): 084305.

[19] Tong W M, Li L P, Hu W B, Yan T J, Li G S. Systematic control of monoclinic $CdWO_4$ nanophase for optimum photocatalytic activity. *J. Phys. Chem. C*, 2010, **114**(3): 1512.

[20] Yang L S, Li L P, Zhao M L, Fu C C, Li G S. Is there lattice contraction in multicomponent metal oxides? Case

study for $GdVO_4:Eu^{3+}$ nanoparticles. *Nanotechnology*, 2013, **24**(30): 305701.

[21] Nguyen T D, Mrabet D, Do T O. Controlled self-assembly of Sm_2O_3 nanoparticles into nanorods: simple and large scale synthesis using bulk Sm_2O_3 powders. *J. Phys. Chem. C*, 2008, **112**(39): 15226.

[22] Yang J, Li C X, Cheng Z Y, Zhang X M, Quan Z W, Zhang C M, Lin J. Size-tailored synthesis and luminescent properties of one-dimensional $Gd_2O_3:Eu^{3+}$ nanorods and microrods. *J. Phys. Chem. C*, 2007, **111**(49): 18148.

[23] Lee K H, Byeon S H. Extended members of the layered rare-earth hydroxide family, $RE_2(OH)_5NO_3 \cdot nH_2O$ (RE= Sm, Eu, and Gd): Synthesis and anion-exchange behavior. *Eur. J. Inorg. Chem.*, 2009, **8**(7): 929.

[24] Wang X, Li Y D. Rare-Earth-compound nanowires, nanotubes, and fullerene-like nanoparticles: Synthesis, characterization, and properties. *Chem. Eur. J.*, 2003, **9**: 5627.

[25] Hazarika S, Paul N, Mohanta D. Rapid hydrothermal route to synthesize cubic-phase gadolinium oxide nanorods. *Bull. Mater. Sci.*, 2014, **37**(4): 789.

[26] Peng D F, Beysen S, Li Q, Jian J K, Sun Y F, Jiwuer J. Hydrothermal growth of octahedral Fe_3O_4 crystals. *Particuology*, 2009, **7**: 35.

[27] Peng D, Beysen S, Li Q, Sun Y F, Yang L Y. Hydrothermal synthesis of monodisperse α-Fe_2O_3 hexagonal platelets. *Particuology*, 2010, **8**: 386.

[28] Mohanta D, Nath S S, Mishra N C, Choudhury A. Irradiation induced grain growth and surface emission enhancement of chemically tailored ZnS:Mn/PVOH nanoparticles by Cl^{+9} ion impact. *Bull. Mater. Sci.*, 2003, **26**(3): 289.

[29] Mohanta D, Nath S S, Bordoloi A, Choudhury A, Dolui S K, Mishra N C. Optical absorption study of 100-MeV chlorine ion-irradiated hydroxyl-free ZnO semiconductor quantum dots. *J. Appl. Phys.*, 2002, **92**(12): 7149.

[30] Penn R L, Banfield J F. Imperfect oriented attachment: dislocation generation in defect-free nanocrystals. *Science*, 1998, **281**(5379): 969.

[31] Zhang J, Huang F, Zhang L. Progress of nanocrystalline growth kinetics based on oriented attachment. *Nanoscale*, 2010, **2**(1): 18.

[32] Zhang Y X, Guo J, White T, Tan T T Y, Xu R. Y_2O_3:Tb nanocrystals self-assembly into nanorods by oriented attachment mechanism. *J. Phys. Chem. C*, 2007, **111**(22): 7893.

[33] Polleux J, Pinna N, Antonietti M, Niederberger M. Ligand-directed assembly of pre formed titania nanocrystals into highly anisotropic nanostructures. *Adv. Mater.*, 2004, **16**(5): 436.

[34] Tang Z, Kotov N A, Giersig M. Spontaneous organization of single CdTe nanoparticles into luminescent nanowires. *Science*, 2002, **297**(5579): 237.

[35] He W, Dickerson J H. Thermally driven isotropic crystallinity breaking of nanocrystals: Insight into the assembly of EuS nanoclusters and nanorods with oleate ligands. *Appl. Phys. Lett.*, 2011, **98**(8): 081914.

[36] Guo H, Yang X D, Xiao T, Zhang W P, Lou L R, Mugnier J, Structure and optical properties of sol-gel derived Gd_2O_3 waveguide films. *Appl. Surf. Sci.*, 2004, **230**: 215.

[37] Hu C G, Liu H, Dong W T, Zhang Y Y, Bao G, Lao C S , Wang Z L. $La(OH)_3$ and La_2O_3 nanobelts—synthesis and physical properties. *Adv. Mater.*, 2007, **19**(3): 470.

[38] Zhang N, Yi R, Zhou L B, Gao G H, Shi R R, Qiu G Z, Liu X H. Lanthanide hydroxide nanorods and their thermal decomposition to lanthanide oxide nanorods. *Mater. Chem. Phys.*, 2009, **114**(1): 160.

[39] Zheng J S, Huang F, Yin S G, Wang Y J, Lin Z, Wu X L, Zhao Y B. Correlation between the photoluminescence and oriented attachment growth mechanism of CdS quantum Dots. *J. Am. Chem. Soc.*, 2010, **132**(28): 9528.

[40] Murphy D M. EPR Spectroscopy of Polycrystalline Oxide Systems I: Metal Oxide Catalysis. Edited by S David Jackson, Justin S J Hargreaves. Weinheim: WILEY-VCH Verlag GmbH, 2009. ISBN: 978-3-527-31815-5.

[41] Wertz J E, Auzins P, Weeks R A, Silsbee R H. Electron spin resonance of *F* centers in magnesium oxide confirmation of the spin of magnesium-25. *Phys. Rev.*, 1957, **107**: 1535.

Rapid hydrothermal route to synthesize cubic-phase gadolinium oxide nanorods

SAMIRAN HAZARIKA, NIBEDITA PAUL and DAMBARUDHAR MOHANTA*

Department of Physics, Tezpur University, Tezpur 784 028, India

Abstract. An inexpensive fabrication route and growth mechanism is being reported for obtaining quality gadolinium oxide (Gd_2O_3) nanoscale rods. The elongated nanoscale systems, as produced via a hydrothermal process, were characterized by X-ray diffraction (XRD), high resolution transmission electron microscopy (HRTEM), optical absorption spectroscopy, photoluminescence (PL) spectroscopy, Raman spectroscopy and magnetic hysteresis measurements. XRD patterns of the nanorods, as-prepared from independent precursors of different pH, depict a cubic crystal phase and an average crystallite size of 5–6·5 nm. As revealed from HRTEM micrographs, diameter of the nanorods prepared at pH = 13·3 (~7 nm) was much smaller than the rods prepared at pH = 10·8 (~19 nm). However, the aspect ratio was more than double in the former case than the latter case. PL response was found to be dominated by defect mediated emissions, whereas Raman spectrum of a given specimen (pH = 10·8) has revealed characteristic $F_g + A_g$ modes of cubic phase of Gd_2O_3 nanorods, apart from other independent modes. Furthermore, $M \sim H$ plot of the nanorod system (pH = 10·8) exhibited slight departure from the ideal superparamagnetic behaviour, with low remanence and coercive field values. The exploitation of one-dimensional Gd_2O_3 nanorods have immense potential in the production of advanced contrast agents, smart drives and also in making novel ferrofluids of technological relevance.

Keywords. Hydrothermal; nanostructure; rare-earth; gadolinium oxide.

1. Introduction

In recent years, compared to bulk and other low dimensional structures, elongated nanostructures such as nanowires, nanorods and nanotubes have gained remarkable research interest owing to their novel electrical, optical and magnetic properties (Du and Tendeloo 2005). Organized, but anisotropic growth of one-dimensional (1-D) systems, under specific environment, has emerged as an area of topical interest with immense potential in the field of nanophotonics, high performance nanophosphors and other functional elements (Holmes *et al* 2000; Bockrath *et al* 2001; Huang *et al* 2001; Li and Xia 2003; Xia *et al* 2003). On the other hand, rare-earth (RE) oxide based nanostructures are found to be promising candidates in the field of high throughput luminescent devices, catalysis and other functional devices based on their excellent electronic, optical and physicochemical responses arising from $4f$ electrons (Tang *et al* 2003). Not surprisingly, all these properties could be largely influenced by their chemical composition, crystal structure, shape and dimensionality (Xu *et al* 2009).

1-D nanostructures can be developed by several methods, such as chemical and physical vapour processes (Yu *et al*

2004), laser ablation (Duan and Lieber 2000), solution phase (Trentler *et al* 1995), arc discharge (Choi *et al* 2000), hydrothermal treatment (Du *et al* 2001, 2003; Dhananjaya *et al* 2012a, b), vapour-phase transport process (Wu and Yang 2000) and template-based method (Huang *et al* 2000). Above all, hydrothermal synthesis technique has a unique advantage as it is capable of providing high purity and high yield, apart from homogeneously grown anisotropic nanostructures. Besides, hydrothermal technique does not use any catalyst and template. Production of 1-D gadolinium oxides and hydroxides by hydrothermal method have been reported by many authors. Gadolinium oxide (Gd_2O_3) exists in three different crystallographic forms: hexagonal, monoclinic and cubic (Bai *et al* 2009). Owing to its thermal and chemical stabilities, narrow emission (Gai *et al* 2011) and having a wide direct bandgap of 5·3 eV (Singh *et al* 2004), Gd_2O_3 is believed to be a promising host for a number of applications. It can be an useful candidate in the deployment of waveguide devices (Guo *et al* 2004), high dielectric constant components and other such devices. On the other hand, elongated RE oxides have recently been applied to drug delivery and competitive immunoassays (Liu *et al* 2012). However, transforming bulk Gd_2O_3 powder into its hydroxide product and later to 1-D nanorods by subsequent dehydration is rarely found

---

*Author for correspondence (best@tezu.ernet.in)

in the literature. To be specific, obtaining elongated RE nanorods from the bulk powder, short synthesis time along with a catalyst free approach are the main features of the present work.
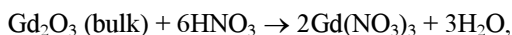
Herein, we demonstrate production of 1-D Gd_2O_3 nanorods via a user-friendly and cost-effective hydro-thermal route, without using any sort of catalyst or template. The effect of pH was discussed in the light of growth mechanism of the nanorods. Characteristic properties with respect to structural, optical emission and magnetic responses of the synthesized nanorods are discussed.
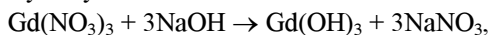
2. Experimental

2.1 *Synthesis of Gd_2O_3 nanorod powder*

A simple hydrothermal procedure was carried out to pro-duce quality Gd_2O_3 nanorods (Dhananjaya *et al* 2011). In a typical procedure, 0·28 g of bulk Gd_2O_3 (Otto, 99·9% purity) was first dispersed in 35 mL distilled water and dilute HNO_3 was added dropwise until a clear sol was obtained. pH was then adjusted to 9·2, 10·8 and 13·3 by adding several drops of 5 M NaOH solution under vigorous stirring. The mixture was then transferred to a teflon-lined stainless steel autoclave and subjected to oven heating at ~ 140 °C for 24 h. A white solid product of $Gd(OH)_3$ was then collected by filtering the precursor using a Whatman filter®. The product was washed several times, first with distilled water and then with ethanol, followed by oven-drying at 80 °C. Finally, the hydroxide powder was annealed at 600 °C, for 3 h so as to facilitate spontaneous decomposition of $Gd(OH)_3$ and consequently, dehydration to yield Gd_2O_3 nanopowder. The flow chart of hydrothermally synthesized Gd_2O_3 nanorods is shown in figure 1.
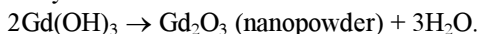
Acidification:
Gd_2O_3 (bulk) + $6HNO_3$ → $2Gd(NO_3)_3$ + $3H_2O$,

Hydrolysis:
$Gd(NO_3)_3$ + $3NaOH$ → $Gd(OH)_3$ + $3NaNO_3$,

Dehydration:
$2Gd(OH)_3$ → Gd_2O_3 (nanopowder) + $3H_2O$.

2.2 *Characterization techniques*

The crystallographic information was revealed by a Rigaku miniFlex X-ray diffractometer (XRD) that uses a CuKα source (λ = 1·54 Å). The diffraction angle was varied in the range of 20–60° and with a step angle of 0·05°. Transmission electron microscopy (TEM) images were recorded by a JEOL JEM 2100 machine, operating at an accelerating voltage of 200 kV. Thermogravimetric analysis (TGA) was performed on the hydroxide product

$Gd(OH)_3$ of the sample (prepared at pH 10·8) using a TGA-50 Shimadzu thermogravimetric analyser. The opti-cal absorption study was performed by a UV–Visible spectrophotometer (UV 2450, Shimadzu), while photo-luminescence excitation and emission responses were assessed by a Perkin-Elmer LS 55 spectrophotometer. Finally, Raman measurements were recorded by using a Renishaw In-Via Raman spectrometer (Renishaw, Wotton-under-Edge, UK) equipped with an Ar^+ laser of λ = 514·5 nm, used as the excitation source. The spectrum was obtained with a measured resolution of 0·3 cm^{-1}. Lastly, magnetic hysteresis measurement was carried out on a particular specimen (prepared at pH = 10·8) at room temperature using a MPMS SQUID VSM (Quantum Design, USA).

3. Results and discussion

3.1 *Structural and morphological features along with growth mechanism*

XRD patterns of the as-synthesized $Gd(OH)_3$ prepared at pH = 10·8 and Gd_2O_3 nanorod-products prepared at pH = 9·2, 10·8 and 13·3 are depicted in figure 2(a). The hydro-xide product exhibited hexagonal crystal structure with observable diffraction planes indexed as (1 1 1), (1 0 1), (2 0 1) and (0 0 2) (JCPDS no. 83-2037) (Thongtem *et al* 2010). After annealing at 600 °C, prominent, but appa-rently broadened diffraction peaks corresponding to (2 2 2), (4 0 0), (4 4 0) and (6 2 2) crystallographic planes suggest that nanocrystallites would crystallize into a cubic phase (JCPDS no. 86-2477) (Dhananjaya *et al* 2011). No peak due either to hydroxides, impurities or byproducts was detected. With symbols having their usual meanings and using the diffraction formula relevant to cubic phase: $d_{hkl} = (h^2 + k^2 + l^2/a^2)^{1/2} = \lambda/2 \sin\theta$, for a first-order diffrac-tion, the crystal cell parameters ($a = b = c$) could be esti-mated. The lattice parameters of the samples synthesized at pH of 9·2, 10·8 and 13·3, were estimated to be 10·80, 10·83 and 10·79 Å, respectively. Earlier, a cubic-phase cell parameter of 10·81 Å was predicted for Gd_2O_3 sys-tem (Ningthousam *et al* 2009). The average crystallite size (d) and microstrain (η) can also be calculated from the popular Williamson–Hall (W–H) expression

$$\beta \cos\theta = 0·9\lambda/d + 4\eta\sin\theta,$$

which represents the equation of a straight line. The aver-age crystallite size was found to be ~ 5·19, 6·46 and 6·09 nm for pH 9·2, 10·8 and 13·3 cases, respectively along with a negative microstrain value of the order ~ 10^{-3} (table 1). A negative strain could be due to the relaxed nature of the nanocrystallites present in the nanorods.

HRTEM images of the nanorod samples, prepared at pH 10·8 and 13·3, are shown in figures 2(b) and (c). As for pH 10·8, a number of nanorods with an average diameter ~ 19 nm and length ranging from 76 to 115 nm are evident
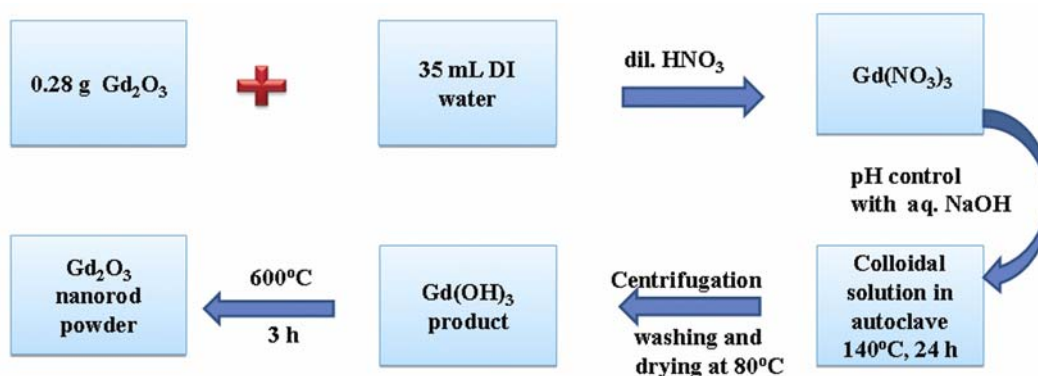
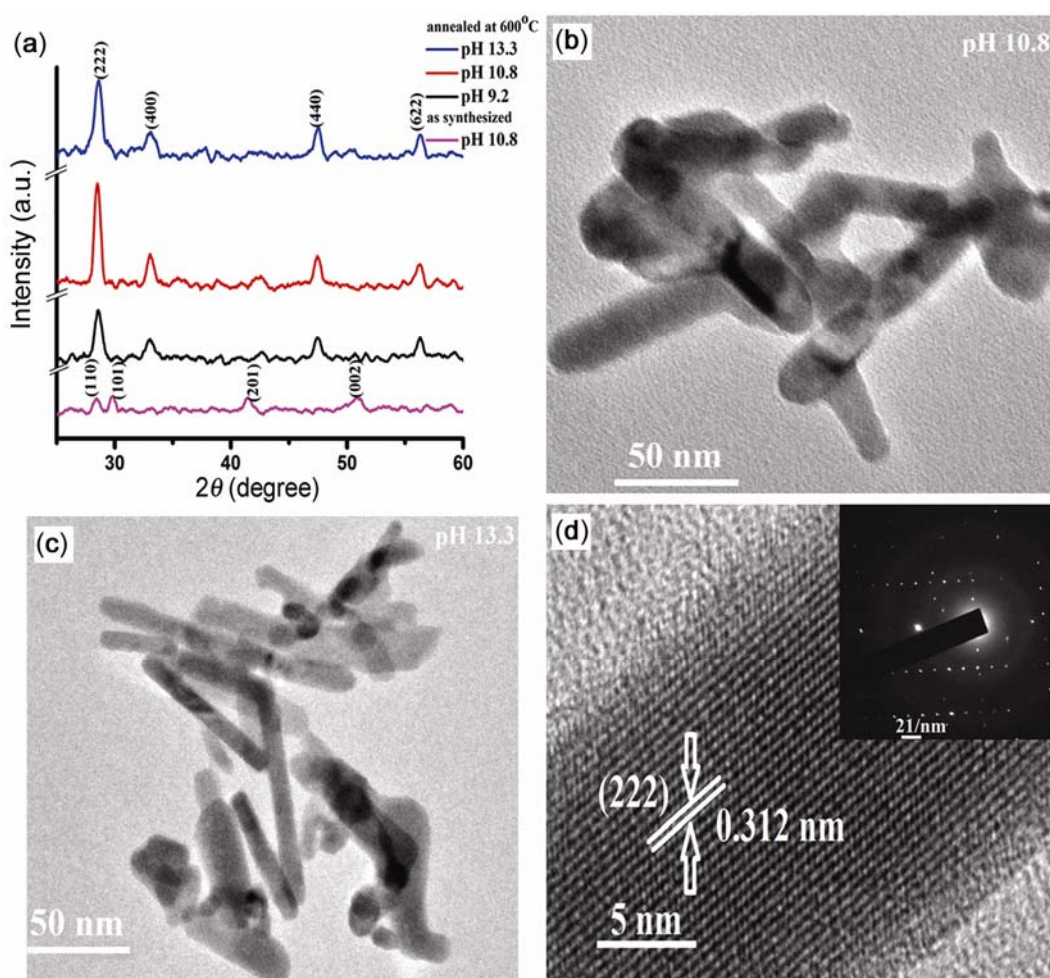**Figure 1.** Block diagram of hydrothermally synthesized Gd_2O_3 nanorods.

Figure 2. (**a**) XRD patterns of as-synthesized $Gd(OH)_3$ product (pH 10·8) and Gd_2O_3 nanorods derived from precursors of different pH, (**b**) and (**c**) represent HRTEM images of nanorod samples synthesized at pH 10·8 and 13·3, respectively. Magnified image of an isolated Gd_2O_3 nanorod (derived from pH 10·8 precursor) with crystal lattice fringes depicted in (**d**). The SAED pattern is being highlighted in the inset of (**d**).

in the micrograph (figure 2b). The rods resemble the structure of 'unfold fingers', with smoothened surfaces but without a branching effect. For any nanorod, the diameter at the middle of the rod was much larger than at the extreme-edge. This is ascribed to the spontaneous decom-position of gadolinium hydroxide into its oxide product followed by subsequent assimilation of crystallites along (2 2 2) plane and instant termination at the end. Also, all Gd_2O_3 nanorods were not found in the same focal plane and that is why we observed a reasonable difference in

Table 1. Average crystallite size (nm), lattice parameter (nm), microstrain and dimension of nanorods (nm) of as-synthesized Gd_2O_3 nanorod systems.

Nanorods synthesized from precursors	Avg. crystallite size (d) (nm)	Lattice parameter ($a = b = c$) (nm)	Microstrain ($\times 10^{-3}$)	Dimension of nanorods		
				Length (nm)	Diameter (nm)	Aspect ratio
pH 9·2	5·19	1·080	−12·69	–	–	–
pH 10·8	6·46	1·083	−8·93	75–115	19	∼4
pH 13·3	6·09	1·079	−8·54	60–128	7	∼8·5

the image contrast of many off-aligned rods. In case of sample synthesized from a precursor of pH 13·3, the range of average nanorod length was found to be wider, i.e. 60–128 nm, but having a reduced average diameter of ∼7·1 nm (figure 2c). Thus, both shorter and longer rods were achievable at a higher pH. We speculate that, unrestricted preferential growth of nanocrystallites might have led to longer sized rods. But shorter nanorods could have been developed due to obstruction of one nanorod growing in the vicinity of the other or, thermodynamic instability that would keep surface energy of the overall system minimum. Consequently, the diameter of the rods can also be reduced in this case. As diameter is close to the average crystallite dimension (see XRD analysis), we expect that the aligned growth is manifested by just piling up of single crystallites along a preferred direction. Whereas, nanorods derived from a precursor of lower pH (10·8), comprise of several crystallites along a direction normal to the *c*-axis preferential growth, thereby resulting in a larger diameter (∼19 nm) of the rods. Considering the lower limit of the nanorod length, the aspect ratio was estimated to be ∼4 and 8·5 corresponding to pH = 10·8 and 13·3 cases, respectively. A higher pH value represents a higher concentration of OH^- ions and a higher chemical potential of the precursor solution. A higher chemical potential is necessary for the growth of higher aspect ratio 1-D nanostructures (Yang *et al* 2007). In contrary to the results of Yang *et al* (2007) here, we realized that, nanorods with a higher aspect ratio could be obtained from a high pH precursor, but along with some amount of inhomogeneity. Figure 2(d) shows an enlarged view of the selected region of a nanorod of figure 2(c). A clear lattice fringe pattern suggests that the nanorod specimen is highly crystalline one with an interplanar spacing of ∼0·312 nm which corresponded to the (2 2 2) crystallographic plane of the nanosystem. This is, in fact, consistent to the XRD pattern of the nano-Gd_2O_3 specimen derived from pH = 10·8. The selected area electron diffraction (SAED) pattern of the nanorods (prepared at pH 10·8) characterizes a number of arrayed bright spots thus indicating highly crystalline nature of the specimen under study.

The growth mechanism of Gd_2O_3 nanorods can be illustrated in a block diagram, shown in figure 3. The growth of Gd_2O_3 nanorods was believed to be governed by a solution-solid phase process (Wang *et al* 2004). In the hydrothermal process, several drops of aq. NaOH were added to adjust pH of the solution. According to Xu *et al* (2009), the growth morphology is neither governed by a catalyst nor directed by any template (Xu *et al* 2009). On adding aq. NaOH, the Gd^{3+} ions tend to interact with OH^- ions formed from aq. NaOH. On adding NaOH, a gentle white solution is formed which comprised of colloidal particles. The colloids, while partially dissolved in water results in a metastable supersaturated solution under hydrothermal environment. On cooling back to room temperature, a large number of seed particles of $Gd(OH)_3$ were formed through homogeneous nucleation process. It is the seed which becomes the basis of 1-D elongated nanostructures formed as a result of coherent re-crystallization process. Accordingly, the whole supersaturated solution is recrystallized to yield highly crystalline rod-shaped structures (Xu *et al* 2009). A high temperature sintering step is needed to facilitate instant dehydration thereby resulting in the desired product of Gd_2O_3 nanorods.

Thermogravimetric analysis (TGA) was carried out to assess the progressive weight loss of $Gd(OH)_3$ within a range of temperature (27–600 °C). Typically, TGA curve in figure 4 characterizes four successive, uneven steps. The first step, observable within 27–250 °C experiences a weight loss of 2·1% and is due to the (partial) dehydration of adsorbed H_2O in $Gd(OH)_3$. The second step was in the range of 250–335 °C and having a loss of ∼8·02%, whereas third step was between 335 and 440 °C and with a weight loss of ∼1·8%. The second and third steps, ranging from 250 to 440 °C, collectively represent decomposition of $Gd(OH)_3$ to the intermediate product of GdOOH, prior to the complete oxide product. The transformation of intermediate GdOOH to final Gd_2O_3 product is obtained in the fourth step (440–594 °C) and with a weight loss of 1·7%. The total weight loss is ∼13·62%, which is comparable to an earlier prediction (∼13·03%) for complete decomposition of $Gd(OH)_3$ to form Gd_2O_3 (Xu *et al* 2009).

3.2 *Optical absorption, emission and phononic features*

UV–Visible absorption spectroscopy is the most common but an important spectroscopy tool which is capable of revealing electronic transitions of a particular valence
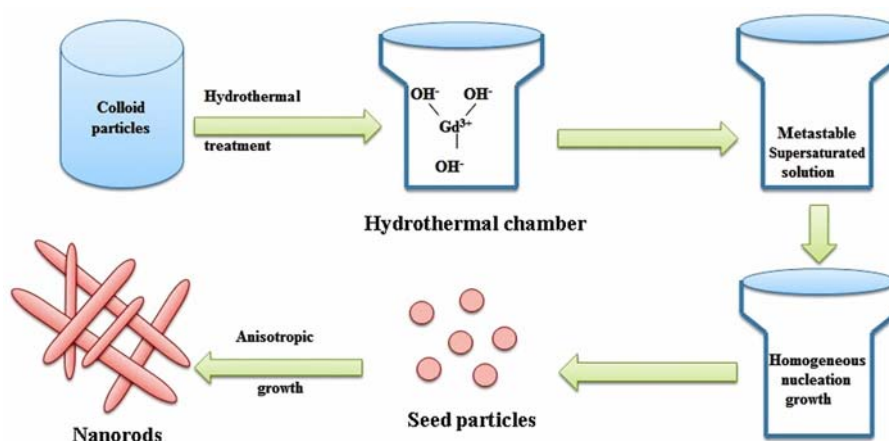
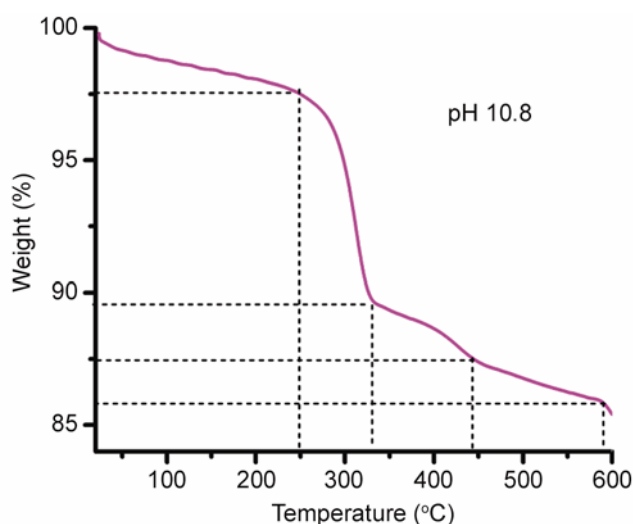**Figure 3.** A scheme of growth mechanism illustrating formation of Gd_2O_3 nanorods.

Figure 4. Thermogravimetric analysis of unsintered $Gd(OH)_3$ product (pH 10·8).
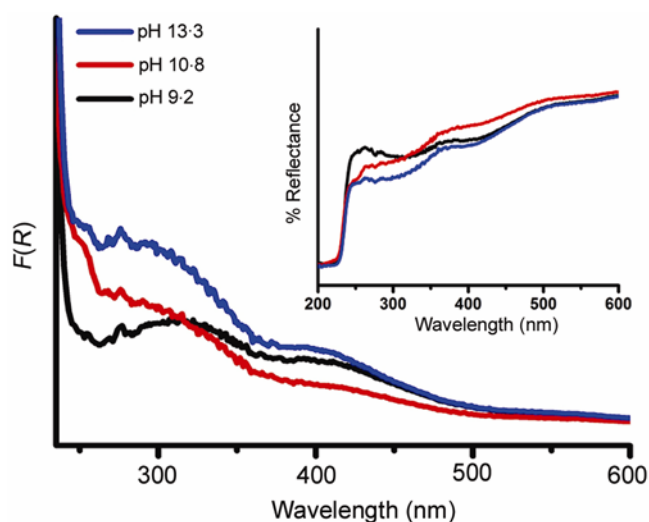

Figure 5. Kubelka–Munk plot representing $F(R)$ as absorbance (inset shows actual reflectance spectra).

state. Either absorbance or reflectance (where absorption is not strong) can be employed to determine such transitions. The absorption spectra as obtained from the reflectance data of our nanorod samples are shown in figure 5. The reflectance spectra being shown as the inset of figure 5. For conversion, we have used popular Kubelka–Munk equation

$$F(R) = (1 - R)^2/2R,$$

where R represents reflectance and $F(R)$ the corresponding absorbance (Han *et al* 2007). Gd^{3+} has [Xe] $4f^7$ configuration, which means it has half-filled shell having a $^8S_{7/2}$ ground state. The energy absorption in Gd is mediated via transition of $4f$ electrons to $5d$ level and then reorganization of $4f$ electrons into various multiplets. The seven electrons in $4f$ orbitals of Gd have as many as 3432 multiplets and the ground state is $^8S_{7/2}$ (Rahman *et al* 2011; Hazarika and Mohanta 2013). Among these multiplets, the low lying multiplet above the ground state is $^6P_{7/2}$. Essentially, two absorption peaks were observed in the spectra. The absorption peak positioned at ~274 nm is typical for Gd_2O_3 nanorods and is attributed to $^8S_{7/2} \rightarrow {}^6I_{7/2}$ transition (Rahman *et al* 2011). The peak positioned at ~398 nm, may be attributed to recombination of delocalized electrons close to the conduction band with a single charged state of surface oxygen vacancy as per Wang's proposition (Hu *et al* 2007; Zhang *et al* 2009). The peak at ~274 nm has a strong absorption feature, particularly for the nanorod specimen derived at a higher pH value.

Photoluminescence spectroscopy is a powerful technique to understand the nature of radiative transitions and defect related emission response of a material system. Figure 6(a) shows room temperature photoluminescence excitation (PLE) spectra of pH 10·8 Gd_2O_3 nanorods monitored at an emission wavelength of ~480 nm. The peaks, in PLE spectra, often represent absorption characteristics of the system under study. Basically, Gd^{3+} has a simpler absorption spectrum in comparison to the other
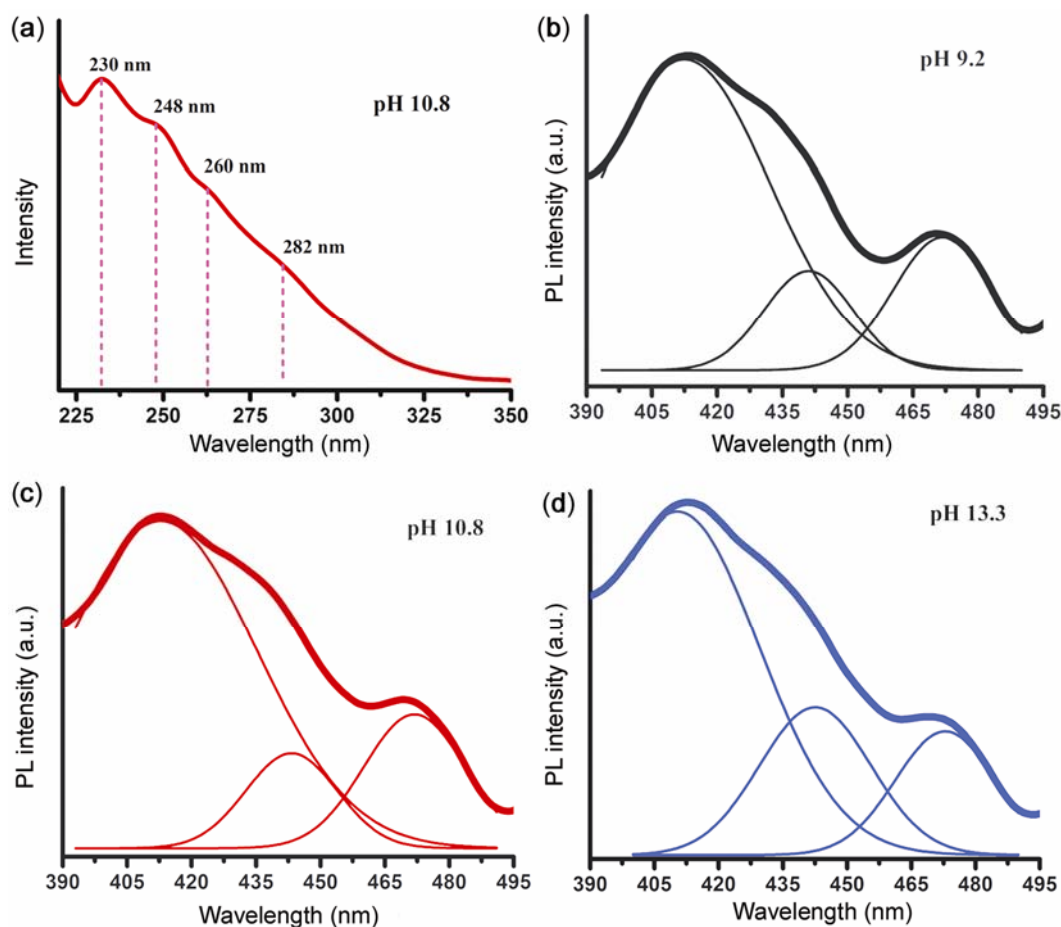
Figure 6. Room temperature (**a**) PL excitation spectrum of nanorod sample (pH 10·8) considering $\lambda_{em} = 480$ nm and PL emission spectra (with deconvolution) corresponding to $\lambda_{ex} = 300$ nm, obtained for all three samples derived at (**b**) pH 9·2, (**c**) pH 10·8 and (**d**) pH 13·3.

trivalent RE ions. Note that, the ground state energy level for Gd^{3+} is $^8S_{7/2}$ level. As can be found, the excitation spectra have clearly revealed four important peaks, positioned at ~ 230, 248, 260 and 282 nm. The 230 nm emission peak is attributed to the excitation band of Gd_2O_3 host (Pang *et al* 2003). The peak at ~ 248 nm is ascribed to one of the transitions corresponding to $^8S_{7/2} \rightarrow ^6I_{j/2}$ multiplets, where $j = 9, 12, 13, 15$ and 17 (Mukherjee *et al* 2008). The band observed at ~ 260 nm is assigned to $^8S_{7/2} \rightarrow ^6D_{9/2}$ transition (Kripal and Mishra 2010). The peak at ~ 282 nm is attributed to $^8S_{7/2} \rightarrow ^6I_{7/2}$ transition (Mukherjee *et al* 2008). On the other hand, room temperature emission spectra of Gd_2O_3 nanorods, excited at a wavelength of ~ 300 nm are shown in figures 6(b–d) representing characteristic features of the nanorods synthesized at a pH of 9·2, 10·8 and 13·3, respectively. The asymmetrically broadened spectra signify the superimposition of several peaks of different origin. The deconvolution of each of the spectra through multiple Gaussian fitting could help extracting independent peaks, which are presented in figures 6(b–d). All the samples have showed three prominent peaks, at ~ 413, 442 and 472 nm. The

band to band emission was not observable due to the improved defect related emission response. The peak maxima at ~ 413, 442 and 472 nm could be attributed to surface defects of different Schottky and Frenkel types (Dhananjaya *et al* 2012a, b). The normalized intensity ratio of ~ 413 to 472 nm peak increases with increasing pH value of the desired precursor. In oxide systems, typically oxygen vacancies and interstitials are vastly prevalent and the manifestation of such defects, contribute significantly to the modified photoluminescence response.

Raman spectroscopy is a versatile but non-destructive tool to explore vibrational, rotational and other low frequency modes in the systems under study. The micro-Raman spectrum of the nanorod sample synthesized at a pH of 10·8, is highlighted in figure 7. Apparently, three peaks were observed, which were characterized by Raman shifts located at ~ 314, 359 and 446 cm^{-1}. The peak at ~ 314 cm^{-1} is identified as the mixed modes of $F_g + E_g$ and the one at ~ 446 cm^{-1} as an independent F_g mode (Dilawar *et al* 2008). Most importantly, the prominent peak at ~ 359 cm^{-1} is assigned to $F_g + A_g$ modes, which mainly corresponds to the cubic phase of Gd_2O_3.

3.3 *Magnetic response of Gd$_2$O$_3$ nanorod system*

In order to assess magnetic behaviour of the synthesized product, Gd$_2$O$_3$ nanorod sample (prepared at a pH 10·8) was assessed by a SQUID magnetometer. It is known that, magnetic response changes with the pH value of the precursor solution. In particular, saturation magnetization value (M_s) varies with the particle dimension that depends largely on pH of the precursor. In this context, modified magnetic features due to an increased fraction of superparamagnetic particles was observed in an earlier work (Thakur *et al* 2009). Although magnetic measurements were not performed on all the samples, it is
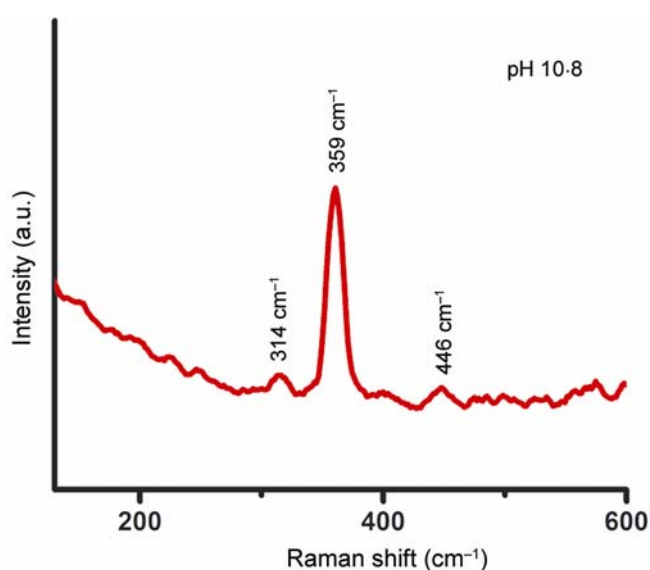

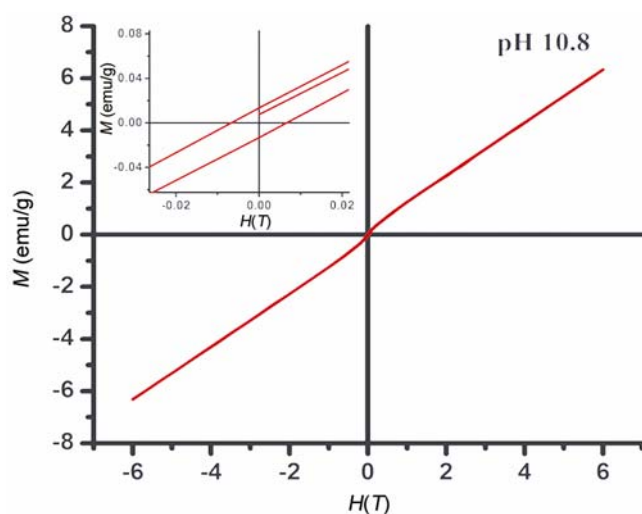**Figure 7.** Raman spectrum of Gd$_2$O$_3$ nanorod sample synthesized at pH 10·8.

Figure 8. Room temperature $M \sim H$ plot of Gd$_2$O$_3$ nanorods synthesized at pH 10·8. Inset shows enlarged view of plot near zero-field.

likely that, M_s value may vary with the aspect ratio of the nanorods (and thus with pH of the sol). As a means of general assessment (if the system is magnetic or not), magnetic measurement was performed on a well-characterized sample (pH = 10·8) the results of which are as discussed below.

Figure 8 depicts response of magnetization vs magnetic field (M–H), measured at room temperature (300 K). The magnetization feature was recorded when the applied field was varied in the range –6 to 6 T. Since no clear hysteresis was observed, we speculate that the sample is likely to be superparamagnetic. Even the saturation magnetization could not be predicted exactly. The paramagnetic nature of the nanorods containing Gd^{3+} centres is due to the presence of half-filled f orbitals with seven electrons (Mukherjee *et al* 2008). Note that characteristic paramagnetic feature of a system is caused by a number of magnetic dipole moments summing up to zero in the absence of an applied field. But the net moment becomes non-zero when the system is subjected to a field. However, superparamagnetism arises when thermal energy is strong enough to orient individual moments randomly. As far as superparamagnetism is concerned, in the past, most of the studies were devoted mostly to iron based nanostructures. We anticipate that, the paramagnetism in Gd$_2$O$_3$ nanorods has arisen from non-interacting localized nature of the magnetic moments. The magnetic properties of Gd^{3+} ions come from seven unpaired inner $4f$ electrons, which are closely bound to the nucleus and effectively shielded by the outer closed shell electrons $5s^25p^6$ from the crystal field. Among various paramagnetic RE ions, Gd^{3+} ions possess a high magnetic moment due to isotropic electronic ground state $^8S_{7/2}$. In order to explore further, we zoomed in $M \sim H$ response near zero field. Remarkably, M value was found to experience a non-zero value in the absence of the field ($H = 0$). This suggests that the investigated sample cannot represent an idealistic superparamagnetic system. The coercive field (H_c) and remanence (M_r) were found to be 0·0066 T and 0·0136 emu/g, respectively. A low coercive field indicates that magnetic moments can be reversed even by changing the direction of a weak applied field. In other words, order of the moments is lost at a higher magnetic field and considering a small remanence magnitude, the Gd$_2$O$_3$ nanorod sample under study behaved closely to a superparamagnetic system.

4. Conclusions

We have demonstrated production and characterization of cubic phase Gd$_2$O$_3$ nanorods, synthesized by a surfactant free hydrothermal method. XRD studies on Gd$_2$O$_3$ systems have revealed cubic phase of the as-synthesized nanorods while unsintered Gd(OH)$_3$ product showed a hexagonal phase. HRTEM analyses have revealed a remarkable distribution of nanoscale rods, with aspect

ratio nearly doubled when the precursor used was changed from pH = 10·8 to 13·3. Moreover, the evidence of a clear lattice fringe pattern of the rods and ordered bright spots as observable from SAED, suggests that the samples were highly crystalline in nature. TGA analysis on the hydroxide product has revealed the total weight loss ~ 13·62% up to a temperature of ~ 600 °C. The photoluminescence response was found to be manifested by various kinds of defects such as Schottky and Frenkel types. The prominent peak in the Raman spectra attributed to the cubic phase of the nanorods. The magnetic measurements have revealed non-ideal superparamagnetic nature of the Gd_2O_3 nanorods at room temperature.

Acknowledgements

References

Bai L, Liu J, Li X, Jiang S, Xiao W, Li Y, Tang L, Zhang Y and Zhang D 2009 *J. Appl. Phys.* **106** 073507

Bockrath M, Liang W, Bozovic D, Hafner J H, Lieber C M, Tinkham M and Park H 2001 *Science* **291** 283

Choi Y C *et al* 2000 *Adv. Mater.* **12** 746

Duan X F and Lieber C M 2000 *Adv. Mater.* **12** 298

Du G H, Chen Q, Che R C, Yuan Z Y and Peng L M 2001 *Appl. Phys. Lett.* **79** 3702

Du G H, Chen Q, Han P D and Peng L M 2003 *Phys. Rev.* **B67** 035323

Du G and Tendeloo G V 2005 *Nanotechnology* **16** 595

Dhananjaya N, Nagabhushana H, Nagabhushana B M, Rudraswamy B, Shivakumara C, Ramesh K P and Chakradhar R P S 2011 *Physica* **B406** 1645

Dhananjaya N, Nagabhushana H, Nagabhushana B M, Rudraswamy B, Sharma S C, Sunitha D V, Shivakumara C and Chakradhar R P S 2012a *Spectrochim. Acta Part A: Mol. Biomol. Spectr.* **96** 532

Dhananjaya N, Nagabhushana H, Nagabhushana B M, Rudraswamy B, Shivakumara C and Chakradhar R P S 2012b *Bull. Mater. Sci.* **35** 519

Dilawar N, Varandani D, Mehrotra S, Poswal H K, Sharma S M and Bandyopadhyay A K 2008 *Nanotechnology* **19** 115703

Gai S, Yang P, Wang D, Li C, Niu N, He F and Li X 2011 *Cryst. Eng. Commun.* **13** 5480

Guo H, Yang X, Xiao T, Zhang W, Lou L and Mugnier J 2004 *Appl. Surf. Sci.* **230** 215

Han T Y, Wu C F and Hsieh C T 2007 *J. Vac. Sci. Technol.* **B25** 430

Holmes J D, Johnston K P, Doty R C and Korgel B A 2000 *Science* **287** 1471

Hu C G, Liu H, Dong W T, Zhang Y Y, Bao G, Lao C S and Wang Z L 2007 *Adv. Mater.* **19** 470

Huang M H, Choudrey A and Yang P 2000 *Chem. Commun.* **12** 1063

Huang Y, Duan X, Wei Q and Lieber C M 2001 *Science* **291** 630

Hazarika S and Mohanta D 2013 *Eur. Phys. J. Appl. Phys.* **62** 30401

Kripal R and Mishra I 2010 *Physica* **B405** 425

Li D and Xia Y 2003 *Nano Lett.* **3** 555

Liu Z, Liu X, Yuan Q, Dong K, Jiang L, Li Z, Ren J and Qu X 2012 *J. Mater. Chem.* **22** 14982

Mukherjee S, Dasgupta P and Jana P K 2008 *J. Phys. D: Appl. Phys.* **41** 1

Ningthoujam R S, Shukl R, Vatsa R K, Duppel V, Kienle L and Tyagi A K 2009 *J. Appl. Phys.* **105** 084304

Pang M L, Lin J, Fu J, Xing R B, Luo C X and Han Y C 2003 *Opt. Mater.* **23** 547

Rahman A T M, Vasilev K and Majewski P 2011 *J. Colloid. Interf. Sci.* **354** 592

Singh M P, Thakur C S, Shalini K, Banerjee S, Bhat N and Shivashankar S A 2004 *J. Appl. Phys.* **96** 5631

Tang Q, Liu Z, Li S, Zhang S, Liu X and Qian Y 2003 *J. Cryst. Growth* **259** 208

Thakur S, Katyal S C and Singh M 2009 *J. Magn. Magn. Mater.* **321** 1

Thongtem T, Phuruangrat A, Ham D J, Lee J S and Thongtem S 2010 *Cryst. Eng. Commun.* **12** 2962

Trentler T J, Hickman K M, Goel S C, Viano A M, Gibbons P C and Buhro W E 1995 *Science* **270** 1791

Wang G, Wang Z, Zhang Y, Fei G and Zhang L 2004 *Nanotechnology* **15** 1307

Wang Z, Quan Z and Lin J 2007 *Inorg. Chem.* **46** 5237

Wu Y and Yang P 2000 *Chem. Mater.* **12** 605

Xia Y, Yang P, Sun Y, Wu Y, Mayers B, Gates B, Yin Y, Kim F and Yan H 2003 *Adv. Mater.* **15** 353

Xu Z, Yang J, Hou Z, Li C, Zhang C, Huang S and Lin J 2009 *Mater. Res. Bull.* **44** 1850

Yu J, Yu J C, Ho W, Wu L and Wang X C 2004 *J. Am. Chem. Soc.* **126** 3422

Yang J, Li C, Cheng Z, Zhang X, Quan Z, Zhang C and Lin J 2007 *J. Phys. Chem.* **C111** 18148

Zhang N, Ran Y, Zhou L, Gao G, Shi R, Qiu G and Liu X 2009 *Mater. Chem. Phys.* **114** 160

Regular Article

Production and optoelectronic response of Tb^{3+} activated gadolinium oxide nanocrystalline phosphors

Samiran Hazarika and Dambarudhar Mohanta[a]

Nanoscience and Soft Matter Laboratory, Department of Physics, Tezpur University, PO Napaam,
Tezpur 784 028, Assam, India

Abstract. We report on the fabrication and optoelectronic features of Tb^{3+} doped gadolinium oxide (Gd$_2$O$_3$) nanpowders. The nanosystems were found to exhibit cubic crystalline structure with an average crystallite size in the range of 11–24 nm. Inclusion of Tb^{3+} into Gd$_2$O$_3$ host has led to suppression of the optical gap but resulted in the enhanced refractive index of the corresponding nanophosphor. In the PL spectra, apart from the oxygen defect related emissions, Tb^{3+} mediated (0.5% of doping level) improved radiative emissions owing to $^5D_4 \rightarrow {}^7F_6$ and $^5D_4 \rightarrow {}^7F_5$ transitions were found to be located at $\sim$492 and $\sim$548 nm; respectively. Rare earth ion doped rare earth oxide nanopowders may find immediate scope in smart optoelectronic elements and advanced nanometric phosphors.

1 Introduction

Rare earth (RE) oxide nanoparticle systems have gained increased scientific interest in recent time. Pure RE systems, or their oxides have potential in imaging, optoelectronic and biomedical applications as they exhibit remarkable magnetic and optical properties [1]. The unusual luminescent properties of RE elements have been found extremely useful for fabricating devices such as plasma panels, flat panel displays, luminescent lighting, IR windows, etc. [2,3]. The RE elements are unique in the sense that, the f-shell containing unpaired electrons is interlocked unlike transition elements. Subject to selection rules, luminescence is caused through definite D-F transitions. Gadolinium oxide (Gd$_2$O$_3$) is a well-known RE sesquioxide which can act as a promising contrast agent in the application of magneto-resonance imaging (MRI) [4]. Basically, Gd$_2$O$_3$ has three types of crystal structures: hexagonal, cubic and monoclinic [5]. Due to its high thermal stability, chemical stability and low phonon energy (phonon cutoff $\approx$600 cm^{-1}) it can act as a promising host material for doping with suitable impurities including RE ions [6]. The cubic phase of Gd$_2$O$_3$ is rather an adequate host for suitable RE doping [6,7]. In particular, Tb^{3+} is chosen as a dopant due to its narrow green emission band arising via $4f$ carrier transitions [8]. In the past, researchers have employed several methods to synthesize RE oxide nanoscale systems (typically, in the range of dimensions 2–100 nm) which include high temperature solid state reaction [9], liquid-phase method [10,11],

combustion method [12], or gas-phase condensation technique [13], hydrothermal synthesis [14–16], template method [17,18], co-precipitation wet chemical route [19].

In this report, we discuss preparation and optoelectronic characterization of Gd$_2$O$_3$ nanophosphor obtained via a solvothermal cum reduction route with a special emphasis on Tb doping. The optical and radiative emission features, due to substitutional doping of Tb^{3+} into Gd$_2$O$_3$ host lattice, are also discussed.

2 Experimental details

First, gadolinium acetate hydrate (GdAc) [Gd(CH$_3$CO$_2$)$_3$· H$_2$O] [CDH, 99.9% pure] was dissolved in deionized water and then a 1:1 molar sol was prepared with citric acid [%99.0 pure, CDH] under vigorous stirring for 30 min. The mixture was placed in an open-air oven at 100 °C so as to facilitate chemical reduction of GdAc to Gd(OH)$_3$ and remove out unwanted water content. The product was further sintered at 400 °C in a tubular furnace for 4 h and then calcined at 800 °C for 2 h to remove the byproducts and carbon-rich compounds. For synthesizing Tb^{3+} doped Gd$_2$O$_3$ product, terbium acetate (TbAc) [Tb (CH$_3$CO$_2$)$_3$ · H$_2$O] [CDH, 99.9% pure] was added to the reaction mixture in the initial stage of the reaction, whereas rest of the reaction steps were kept similar. In order to make 0.5%, 1%, 3% and 5% Tb doped Gd$_2$O$_3$ nanoscale powders, the respective molar ratio of Gd to Tb was varied as 0.005, 0.01, 0.03 and 0.05.

The crystallographic information was revealed by a Rigaku miniFlex X-ray diffractometer (XRD) that uses

a e-mail: best@tezu.ernet.in

a Cu K$_\alpha$ source (λ = 1.54 Å) and collects data in 2θ-θ geometry. The diffraction angle was varied in the range of 20 to 60° and with a step width of 0.05°. Transmission electron microscopy (TEM) images were recorded by a JEOL JEM 2100 machine operating at 200 kV. Fourier transform infrared spectroscopy (FTIR) was used to study the bending, bonding and stretching modes present in the synthesized product. The optical absorption study was performed by a UV-Visible spectrophotometer (UV 2450, Shimadzu), while luminescence response was explored by a PerkinElmer LS 55 spectrophotometer.

3 Results and discussion

Figure 1 shows a set of the XRD patterns, of undoped and Tb^{3+} doped Gd$_2$O$_3$ nanoparticles. The four prominent peaks located at 28.51, 33.10, 47.58 and 56.55° which corresponded to (2 2 2), (4 0 0), (4 4 0) and (6 2 2) crystallographic planes. With a preferred crystallographic orientation along (2 2 2) plane, the diffractograms represent a cubic crystalline structure of Gd$_2$O$_3$ (JCPDS No. 76-0155). As no appreciable peak shifting was noticeable in case of Tb doped Gd$_2$O$_3$ systems, the Tb^{3+} ions were expected to occupy substitutional sites replacing Gd^{3+}. The average crystallite size (d) and microstrain (η) can be calculated from the Williamson-Hall (W-H) expression: $\beta \cos \theta = 0.9\lambda/d + 4\eta \sin \theta$, where β is the full width at half maxima, θ is the diffraction angle in degree and λ is the wavelength of X-ray (1.54 Å). From the W-H plots (not shown), the average crystallite size was found to be in the range of 11–24 nm with the average size of Tb^{3+} doped Gd$_2$O$_3$ systems nearly doubled, as compared to the undoped counterpart (Table 1). The microstrains are of the order of 10^{-3} and 10^{-4}. It can be speculated that, with a
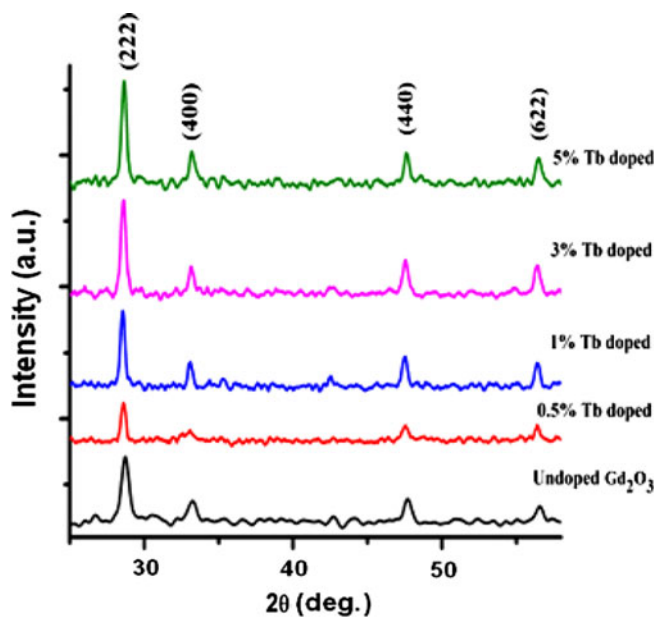

Fig. 1. X-ray diffractograms of undoped and Tb^{3+} doped Gd$_2$O$_3$ nanophosphors.

Table 1. Properties of Tb^{3+} doped Gd$_2$O$_3$ nanocrystalline phosphors.

Tb conc.	Avg. crystallite size (d) in nm	Microstrain (ε)	Refractive index (μ)
0	11.8	-2.15×10^{-3}	1.97
0.5	21.6	2.35×10^{-4}	1.976
1.0	24.7	2.18×10^{-4}	1.977
3.0	24.7	1.98×10^{-4}	1.979
5.0	24.4	4.32×10^{-4}	1.982

negative microstrain (10^{-3}), the undoped Gd$_2$O$_3$ nanopowder is comprising of much relaxed crystallites. With the Tb^{3+} doping, microstrain flips to positive (10^{-4}) values. Though the magnitude is about 10 times lower than the undoped case, a reasonable lattice mismatch (ionic radii: Gd^{3+} ∼94 pm; Tb^{3+} ∼92 pm) [20] might have caused inbuilt stress due to inclusion of Tb^{3+} into the Gd$_2$O$_3$ host lattice. In reference to low Tb^{3+} doping case (∼0.5%), the positive microstrain is nearly doubled when the doping concentration was increased to ∼5%.

TEM studies could not reveal a collective view of significantly large number of particles owing to interfering phosphorescence response under electron beam. Most of the time they were found to exist in the form of clumps in a shiny background (Fig. 2a). In a magnified version, an aggregate of 5–6 crystallites (labeled as, 1, 2 . . .) and with different orientations is shown in Figure 2b. The two red-encircled features depict distinct crystallographic fringes of two independent crystallites (3 and 4) thus ensuring a high degree of crystallinity. The fringe patterns were not clear in case of other marked crystallites as they were not present in the same focal plane. The enlarged view of an isolated nanocrystallite, with distinct lattice fringes, is shown in Figure 2c. The interplanar spacing corresponding to (400) crystallographic plane was found to be ∼0.27 nm. The average diameter of the crystallites, that make up an aggregate, is expected in the range of 10–15 nm. The SAED pattern, shown as inset, has revealed diffused concentric rings along with a few array of bright spots. Thus the sample is mostly polycrystalline in nature though some amount of monocrystallinity may also be present.

As can be found from Figure 3a, optical absorption spectra of the undoped and Tb-doped Gd$_2$O$_3$ nanopowders depict a broad absorption feature over a wide wavelength range. However, all the samples were characterized by three characteristic peak maxima located at ∼254, ∼274 nm and ∼350 nm. The energy absorption in Gd is mediated via transition of $4f$ electrons to $5d$ level and then reorganization of the $4f$ electrons into various multiplets [21]. The seven electrons in $4f$ orbitals of Gd have as many as 3432 multiplets and the ground state is $^8S_{7/2}$ [21]. Among these multiplets, the low-lying multiplet above the ground state is $^6P_{7/2}$. The absorption peak at ∼274 nm is typical for Gd$_2$O$_3$ particles and is attributed to $^8S_{7/2} \rightarrow {}^6I_{7/2}$ transition. Possibly, the weak peak at 254 nm is due to the one of the transition corresponding to $^8S_{7/2} \rightarrow {}^6I_{j/2}$ multiplets where $j = 9, 12, 13, 15$
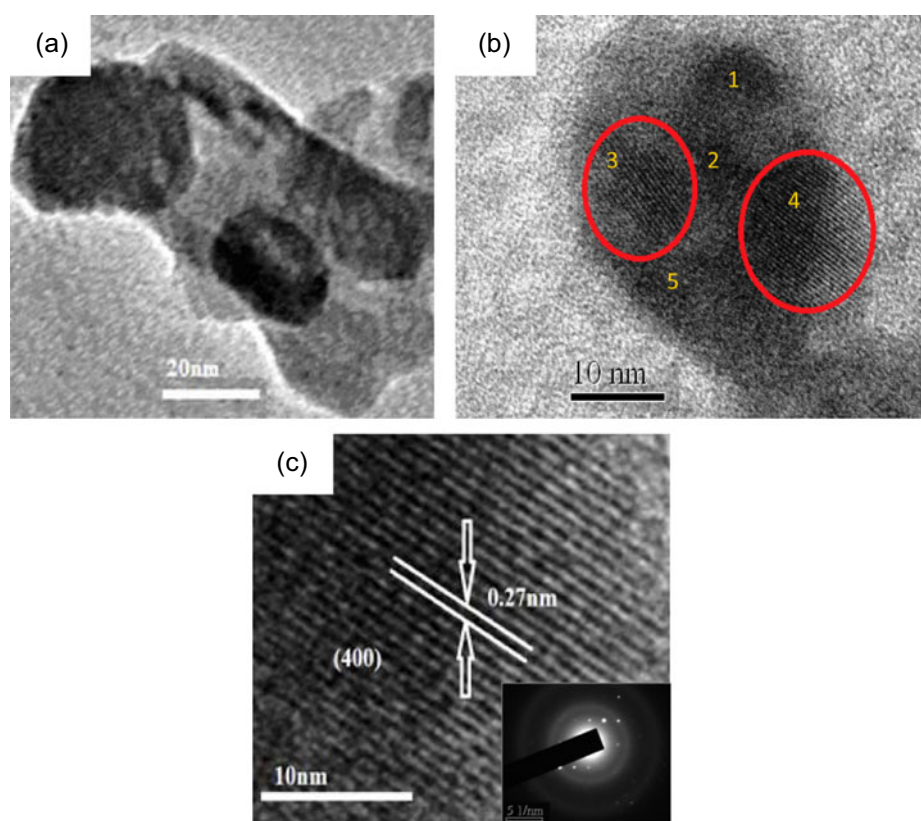
Fig. 2. HRTEM micrographs of nanoscale Gd_2O_3 specimen: in the form of (a) several clumps, (b) an aggregate comprising several crystallites, (c) isolated particle with distinct lattice fringes and with SAED pattern as inset.
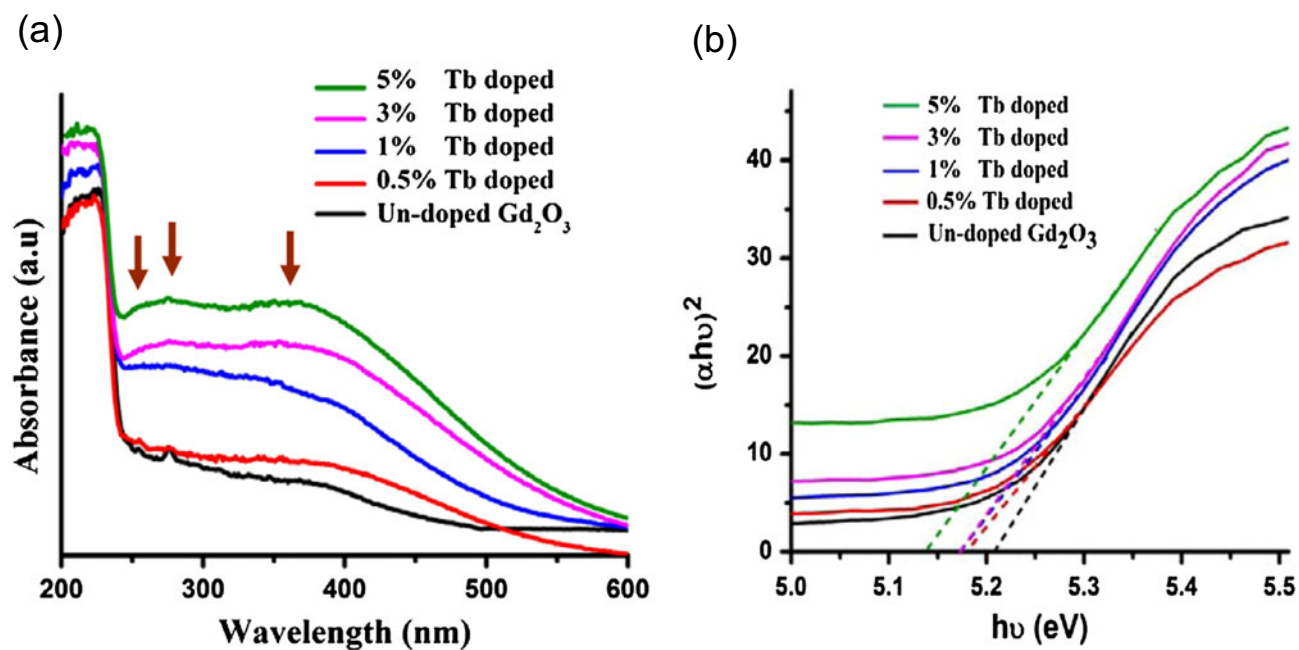

Fig. 3. (a) Optical absorption spectra of undoped and Tb^{3+} doped Gd_2O_3 nanophosphors. Tauc plots of respective samples are shown in (b).

and 17 [22]. The peak at ∼350 nm is ascribed to the $^6P_{7/2} \rightarrow ^8S_{7/2}$ of Gd(III) [23]. With the symbols having their usual meaning, using generalized Tauc relation [24]: $(\alpha h\nu)^{1/n} = A(h\nu - E_g)$, one can estimate optical band gap of the systems under investigation. Here $h\nu$ is the incident photon energy, α is the absorption coefficient, E_g is the optical band gap and A is the system-dependent parameter. Assuming all transitions are direct, and allowed type ($n = 1/2$), the estimated E_g values are found to decrease with Tb doping level. For undoped Gd_2O_3 phosphor, it was 5.22 eV in consistency with an earlier report [25]. For 0.5, 1, 3 and 5% Tb doped Gd_2O_3 systems, the gap was estimated as 5.18, 5.17, 5.16 and 5.14; respectively. The reduction of the fundamental band gap with increasing doping concentration suggests the creation of intermediate states below the bottom of the conduction band. The localized states could either be due to the presence of adequate oxygen vacancies or/and impurity states due to Tb incorporation. Also, band gap follows a decreasing trend with the increase in size of the crystallites [26].

Furthermore, we have calculated the refractive indices (μ) of the nanophosphors using popular *Dimitrov* formula [27] $\mu^2 - 1/\mu^2 + 2 = 1 - \sqrt{(E_g/20)}$. For undoped Gd_2O_3 phosphor the index is 1.97 [28]. It has increased to 1.976, 1.977, 1.979 and 1.982 for 0.5, 1, 3 and 5% doped Gd_2O_3 systems (Tab. 1). In other words, refractive index is improved by ∼0.6% for a maximum value of Tb doping (∼5%). Accordingly, the doped systems are optically more dense as compared to the undoped Gd_2O_3 phosphor. It is anticipated that, material system becomes optically more active in view of inclusion of more localized states into the system.

FTIR spectra of the undoped and Tb^{3+} doped Gd_2O_3 phosphors are shown in Figure 4. The main bands are 2858 cm^{-1}, 2921 cm^{-1} which can be assigned to the symmetric, asymmetric stretching vibration of -CH$_2$ [8].
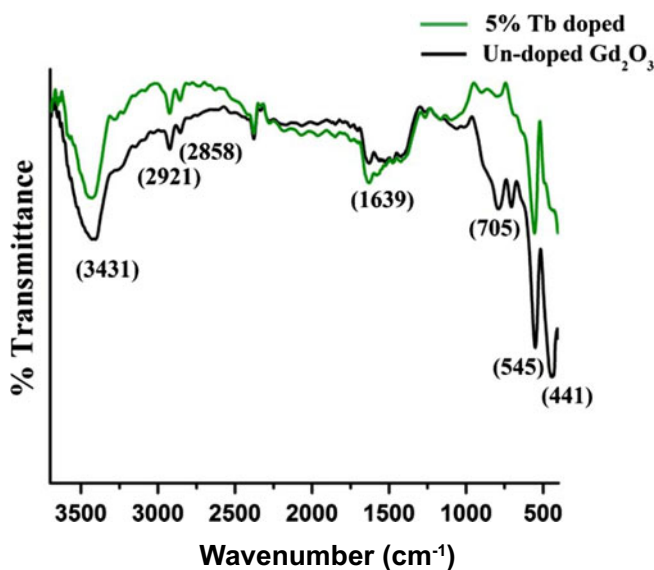

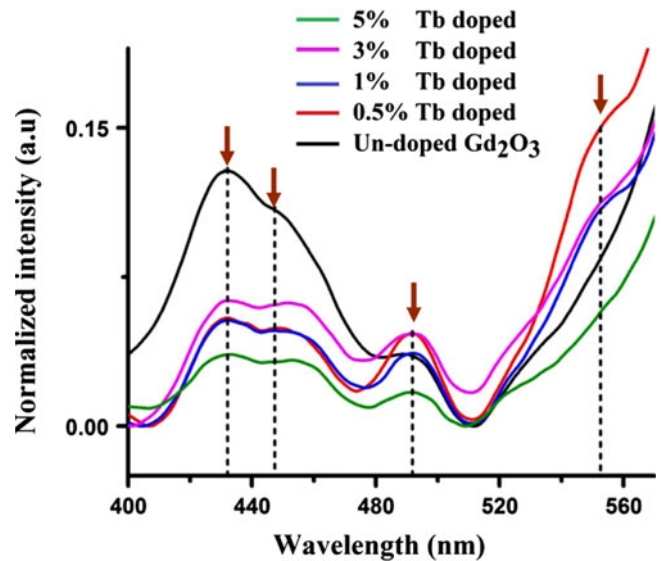**Fig. 4.** Fourier transform infrared (FTIR) spectra of undoped and Tb^{3+} doped Gd_2O_3 samples.

Fig. 5. Room temperature photoluminescence spectra of undoped and Tb^{3+} doped Gd_2O_3 nanophosphors ($\lambda_{ex} = 300$ nm). Arrows indicate different emission peaks.

The band at 705 cm^{-1} is the C-O vibration of the synthesized sample [29]. The bands at ∼3431 cm^{-1} and 1639 cm^{-1} were attributed to O-H stretching vibration and bending of water molecules. Whereas, the bands at ∼545 cm^{-1} and ∼441 cm^{-1} are caused by the stretching vibration of Gd-O of cubic Gd_2O_3 [6]. It may be noted that, while other vibrational modes are not substantially modified, the strength of Gd-O vibrational stretching is adequately improved for Tb doped Gd_2O_3 system.

The PL emission spectra of undoped and Tb^{3+} doped Gd_2O_3 nanophosphors (under 300 nm excitation) are depicted in Figure 5. In a typical spectrum, three main emission peaks were found to be located at ∼432 nm, 450 nm and 492 nm but with variable intensities. The peaks positions were extracted through normalized multi-peak Gaussian fitting such that area under the experimental curve and the fitted curve remains same. The peak maxima at ∼432 and 450 nm can be attributed to surface defects of Schottky and Frankel types, whereas the peak maxima at ∼492 nm are attributed to self-trapped exciton luminescence [30]. Note that, in case of Tb^{3+} doped Gd_2O_3 system, the emission peak at ∼492 nm is adequately improved owing to superimposition of $^5D_4 \rightarrow ^7F_6$-related transitions of Tb^{3+}, which occur almost in the same wavelength regime. However, the transitional events are rather low for a higher level of Tb- doping. Interestingly, the broad emission peak at ∼548 nm is most intense for 0.5% Tb doped Gd_2O_3 system relative to other samples. This green emission due to the Tb^{3+} mediated $^5D_4 \rightarrow ^7F_5$ transition, which was absent in case of the undoped system, was found to get quenched for higher Tb doping level. We anticipate that, this transition is governed by innumerable Tb^{3+} ions present in the interstitial sites and not in their regular Gd^{3+} sites. This was also predicted from the weak diffraction signals for 0.5% Tb doped nanophosphor sample. The PL intensity ratio

between $^5D_4 \rightarrow {}^7F_5$ and $^5D_4 \rightarrow {}^7F_6$ transitions was estimated as 3.8 for 0.5% of Tb doping and 2.4 for 1% and 3% Tb-doping level. Thus it is clear that, only an increment of Tb^{3+}-doping level cannot induce intense green emission. Although in a solvent media, Eu^{3+} or Tb^{3+} doped nanometric Gd$_2$O$_3$ gives a maximum emission corresponding to a dopant concentration of 5–6% [31], we predict that solid Gd$_2$O$_3$ powder could act as an efficient green-phosphorescent candidate when the doping level is ∼0.5%. This is because, the presence of hydroxyl groups, present on the nanocrystallites, can quench the emission response significantly. It is also worth mentioning here that, for a low doping level one may have to sacrifice some amount of crystallinity as can be evident from the weak diffraction peaks. In this regard, one has to work out for optimum crystallinity while protecting selective radiative emission features that will form the basis of numerous technological assets.
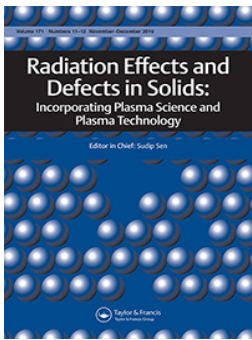
4 Conclusion

To summarize, Tb^{3+} doped Gd$_2$O$_3$ nanophosphors were synthesized by a physicochemical reduction route followed by adequate calcination steps. The XRD studies have revealed cubic crystalline phase of the Gd$_2$O$_3$ phosphor. With Tb incorporation, though optical band gap experienced a decreasing trend, refractive index gets substantially enhanced. The room temperature photoluminescence studies have revealed several emission peaks due to defect or impurity states. The nanophosphors also exhibited the green emission (∼548 nm) resulting from $^5D_4 \rightarrow {}^7F_5$ transition of Tb^{3+}, whereas $^5D_4 \rightarrow {}^7F_6$ transition was found to be overlapped with the blue band of the luminescence pattern. Size and shape-dependent emission and carrier lifetime aspects of these emission responses are in progress.

References

1. S. Mornet, S. Vasseur, F. Grasset, E. Duguet, J. Mater. Chem. **14**, 2161 (2004)
2. J. Feng, G. Shan, A. Maquieira, M.E. Koivunen, B. Guo, B.D. Hammock, I.M. Kennedy, Anal. Chem. **75**, 5282 (2003)
3. M. Nichkova, D. Dosev, S.J. Gee, B.D. Hammock, I.M. Kennedy, Anal. Chem. **77**, 6864 (2005)
4. J. Lue Bridot, A.C. Faure, S. Laurent, C. Riviere, C. Billotey, B. Hiba, M. Janier, V. Josserand, J.L. Coll, L.V. Elst, R. Muller, S. Roux, P. Perriat, O. Tillement, J. Am. Chem. Soc. **129**, 5076 (2007)
5. L. Bai, J. Liu, X. Li, S. Jiang, W. Xiao, Y. Li, L. Tang, Y. Zhang, D. Zhang, J. Appl. Phys. **106**, 073507 (2009)
6. H. Guo, N. Dong, M. Yin, W. Zhang, L. Lou, S. Xia, J. Phys. Chem. B **108**, 19205 (2004)
7. M.L. Pang, J. Lin, J. Fu, R.B. Xing, C.X. Luo, Y.C. Han, Opt. Mater. **23**, 547 (2003)
8. P. Du, L. Song, J. Xiong, Z. Xi, D. Jin, L. Wang, Nanotechnology **22**, 035602 (2011)
9. A.M.G. Massabni, G.J.M. Montandon, M.A. Couto dos Santos, Mater. Res. **1**, 1 (1998)
10. M. Haase, K. Riwotzki, H. Meyssamy, A. Kornowski, J. Alloys Compd. **303**, 191 (2000)
11. R. Si, Y.W. Zhang, H.P. Zhou, L.-D. Sun, C.-H. Yan, Chem. Mater. **19**, 18 (2007)
12. B. Allieri, L.E. Depero, A. Marino, L. Sangaletti, L. Caporaso, A. Speghini, M. Bettinelli, Mater. Chem. Phys. **66**, 164 (2000)
13. H. Eilers, B.M. Tissue, Mater. Lett. **24**, 261 (1995)
14. Y.-P. Fang, A.-W. Xu, L.-P. You, R.-Q. Song, J.C. Yu, H.-X. Zhang, Q. Li, H.-Q. Liu, Adv. Funct. Mater. **13**, 955 (2003)
15. G. Wang, Z. Wang, Y. Zhang, G. Fei, L. Zhang, Nanotechnology **15**, 1307 (2004)
16. H. Assaaoudi, Z. Fang, J.E. Barralet, A.J. Wright, I.S. Butler, J.A. Kozinski, Nanotechnology **18**, 445606 (2007)
17. M. Yada, M. Mihara, S. Mouri, M. Kuroki, T. Kijima, Adv. Mater. **14**, 309 (2002)
18. H. Yang, D. Zhang, L. Shi, J. Fang, Acta. Mater. **56**, 955 (2008)
19. C.-C. Lin, K.-M. Lin, Y.-Y. Li, J. Lumin. **126**, 795 (2007)
20. R.D. Shannon, C.T. Prewitt, Acta Crystallogr. **B26**, 1046 (1970)
21. A.T.M. Anishur Rahman, K. Vasilev, P. Majewski, J. Coll. Interf. Sci. **354**, 592 (2011)
22. S. Mukherjee, P. Dasgupta, P.K. Jana, J. Phys. D: Appl. Phys. **41**, 215004 (2008)
23. D.L. Rogow, C.H. Swanson, A.G. Oliver, S.R.J. Oliver, Inorg. Chem. **48**, 1533 (2009)
24. D.L. Wood, J. Tauc, Phys. Rev. B. **5**, 3144 (1972)
25. D. Jia, L. Lu, W.M. Yen, Optics Commun. **212**, 97 (2002)
26. B. Mercier, C. Dujardin, G. Ledoux, C. Louis, O. Tillement, P. Perriat, J. Appl. Phys. **96**, 650 (2004)
27. V. Dimitrov, S. Sakka, J. Appl. Phys. **79**, 1736 (1996)
28. C. Martinet, A. Pillonnet, J. Lancok, C. Garapon, J. Luminesc. **126**, 807 (2007)
29. Y. Liu, P. Yang, W. Wang, H. Dong, J. Lin, Cryst. Engg. Commun. **12**, 3717 (2010)
30. N. Dhananjaya, H. Nagabhushana, B.M. Nagabhushana, B. Rudraswamy, S.C. Sharma, D.V. Sunitha, C. Shivakumara, R.P.S. Chakradhar, Spectrochim. Acta Part A: Mol. Biomol. Spectr. **96**, 532 (2012)
31. B. Mutelet, P. Perriat, G. Ledoux, D. Amans, F. Lux, O. Tillement, C. Billotey, M. Janier, C. Villiers, R. Bazzi, S. Roux, G. Lu, Q. Gong, M. Martini, J. Appl. Phys. **110**, 094317-1-10 (2011)

Sol-hydrothermally derived gadolinium oxide (Gd$_2$O$_3$) nanorods and tamarind-like shape evolution under 80 MeV C^{6+} ion impact

Samiran Hazarika & Dambarudhar Mohanta

Published online: 14 Dec 2016.

Submit your article to this journal ↗

View related articles ↗

View Crossmark data ↗

Taylor & Francis
Taylor & Francis Group

Sol-hydrothermally derived gadolinium oxide (Gd$_2$O$_3$) nanorods and tamarind-like shape evolution under 80 MeV C^{6+} ion impact

Samiran Hazarika and Dambarudhar Mohanta ⃝iD

Department of Physics, Tezpur University, Tezpur, Assam, India

ABSTRACT

The present work highlights swift heavy ion irradiation-induced shape evolution of gadolinium oxide (Gd$_2$O$_3$) nanorods synthesized via a sol-hydrothermal route. Upon dispersing Gd$_2$O$_3$ nanorods in the polyvinyl alcohol matrix, thin solid films were cast on borosilicate glass substrates. The films were then exposed to 80 MeV carbon-ion irradiation, while fluence was varied in the range of 1×10^{11}–3×10^{12} ions/cm^2. The post analyses were carried out by using X-ray diffraction, high resolution transmission electron microscopy (TEM) and Raman spectroscopy studies. An apparently observable shortening of length (L) and diameter (D) of the nanorods can be revealed through the TEM imaging analyses. Moreover, while exhibiting an aspect ratio (L/D) between 3.3 and 4.7, the nanorods were found to exist in the form of bunching at higher fluences. The irradiation-induced tamarind-like shape evolution at higher fluences was attributed to the overlapping of ion impacts on certain regions of the nanorods. The most intense Raman active peak of the pristine sample located at ~ 360 cm^{-1} was seen to experience blue-shifting (~ 375 cm^{-1}) when irradiated at the highest fluence ($\sim 3 \times 10^{12}$ ions/cm^2). An altered shape evolution of a thermally and mechanically stable oxide system by the energetic ion impact would bring in new insights as regards construction of surface patterns and their potential use in miniaturized devices.

1. Introduction

Rare-earth (RE) oxides, both in micro and nanoscale form, have received significant interest in the field of high-performance luminescent devices, magnets and catalysts and because of the fact that, its optoelectronic response chiefly emerge from the participation of inter-shielded 4f electrons ([1]). The device properties also depend strongly on chemical composition, crystal structure, shape as well as dimensionality of the system ([2, 3]). The lanthanide elements, in particular, exhibit remarkable optoelectronic and magnetic properties. They also act as promising candidate for deployment in nuclear technology as radiation tolerant ceramics ([4, 5]). Among RE sesquioxide-based phosphors, gadolinium

---

CONTACT Dambarudhar Mohanta ✉ best@tezu.ernet.in ⬛ Department of Physics, Tezpur University, PO - Napaam, Tezpur, Assam 784028, India

oxide (Gd_2O_3) has taken the lead to host transition metal (TM) and other RE ions of desired interest. Supported by its excellent optoelectronic feature, nano-dimensional Gd_2O_3 system has already demonstrated its immense scope in biomedical applications, for example, in magneto-resonance imaging replacing traditionally used gadolinium chelates ([6], [7]).

On the other hand, ion irradiation is a nifty technique that is capable of manifesting structural and morphological properties in a controlled manner. The energetic ions deliver energy through different energy loss mechanisms: electronic (S_e) and nuclear (S_n) losses ([8], [9]). The electronic energy loss is due to the inelastic collision of incident ions with the atoms of the target material and becomes dominant in the MeV scale of energy regime (> 1 MeV/nucleon). The nuclear energy loss is due to the elastic collision of the incident ions and becomes effective in the low energy regime (a few keV/nucleon). In MeV irradiation, owing to high energy deposition, within a very short span of time, columnar tracks of the molten zone are generally formed along the ion trajectories ([8], [9]). Moreover, the MeV scale swift ion irradiation could lead to either particle growth or fragmentation of ZnO nanostructures depending on the nature of energy deposition and specimens under study ([10], [11]). The keV ions, are however, employed either for creating point defects and nano-ripples, and while allowing for implantation on the solid targets ([12]–[14]). On the other hand, beta-irradiation effect on oxide glasses and with TM and RE inclusions was shown to block the development of defects in the host ([15]). While irradiation-induced modification of structural, optical and physicochemical responses have been studied mostly in semiconductor oxides and alloys ([11], [16], [17]), the impact of irradiation has been examined in stable RE sesquioxides ([4], [18], [19]). While excellent thermal and mechanical stability of the RE oxides make them useful in certain applications, irradiation-induced modification in a controlled manner remained a challenge till date. In this regard, a detailed account as regards morphological evolution and shape alteration has not been addressed on these sesquioxides when subjected to MeV scale ion impact.
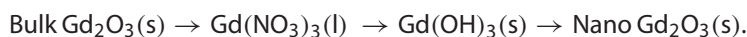
Herein, we demonstrate microstructural and morphological characteristics of sol-hydrothermally grown Gd_2O_3 nanorods irradiated by swift energetic ions. A brief theoretical treatment as regards observation of irradiation-led tamarind-like shape evolution is also highlighted.

2. Experimental details

2.1. Fabrication of elongated Gd_2O_3 nanoscale systems

For synthesizing Gd_2O_3 nanorods, a simple solvo-hydrothermal route was adopted. In a typical procedure, 0.28 g of bulk Gd_2O_3 (Otto, 99.9% pure) is first dispersed in 35 mL deionized water followed by addition of dil. HNO_3 until a clear sol is obtained. The pH of the mixture is adjusted to $\sim$10 by adding several drops of 5 M aq. NaOH under vigorous stirring ($\sim$300 rpm). In the next step, the mixture was transferred to a teflon-lined stainless steel autoclave and then, subjected to oven heating at a temperature of $\sim$140°C, for 24 h. Subsequently, a white solid product of $Gd(OH)_3$ was collected by filtering the precursor using a Whatman filter$^{®}$. The product was subjected to washing several times, first with distilled water and then with ethanol, prior to oven-drying at a temperature of 80°C. Finally, the hydroxide powder was annealed at an elevated temperature of 600°C for 3 h. Mediated by a rapid dehydration process, the spontaneous decomposition of $Gd(OH)_3$ was believed to

yield our desired Gd_2O_3 product. The three-step reaction process on conversion of bulk Gd_2O_3 to its nanoscale form can be shown as follows:

$$Bulk\, Gd_2O_3(s) \rightarrow Gd(NO_3)_3(l) \rightarrow Gd(OH)_3(s) \rightarrow Nano\, Gd_2O_3(s).$$

2.2. Irradiation of Gd_2O_3 nanorod systems

First, the synthesized Gd_2O_3 nanorods are dispersed in 5% polyvinyl alcohol (PVA) matrix media with a $\sim$50% volume dispersion. The nanorod-dispersed PVA films (thickness $\sim$40 μm) were then cast on laboratory grade, sodium borosilicate glass slides ($1 \times 1\, cm^2$) for the irradiation experiment. The samples were irradiated in a high vacuum chamber (pressure $\sim 10^{-6}$ mbar) using 80 MeV C^{6+} ion beams (with a beam current of $\sim$1 pnA, particle nanoampere) available from a 15UD tandem accelerator of Inter University Accelerator Centre (IUAC), New Delhi. In order to ensure homogeneous irradiation condition, the ion beam was first scanned over a thick quartz plate of size $1 \times 1\, cm^2$ fixed at the extreme end of the rectangular sample ladder. The ion fluence could be estimated by integrating the ion charge on the sample ladder, insulated from the vacuum chamber. With a dominant electronic energy loss (S_e) of the chosen ions over the nuclear energy loss (S_n), the ion fluence (φ) was varied in the range of 1×10^{11}–3×10^{12} ions/cm^2. The energy of the ions was chosen in such a way that, the projectile range (R_p) of the ions is good enough to allow ions pass through the target material without stop. It may be noted that, in any embedded system, both the matrix as well as the dispersed objects (nanorods) experience differently on subsequent impact of ions during irradiation. The S_e, S_n and R_p of the projectile ions were estimated accordingly through the SRIM 2008 program ([20]), and presented in Table 1.

2.3. Characterization techniques employed

Both un-irradiated and irradiated nanorod samples are characterized by different analytical instruments. The structural characterization of pristine and irradiated samples are performed by a Rigaku miniFlex X-ray diffractometer (XRD) that uses a copper target (CuK_α, $\lambda = 1.543$ Å). The diffraction intensity was monitored in response to the Bragg's diffraction angle (2θ) varied in the range of 25–60°, while considering a step angle of 0.05° and a scan rate of 2°/min. Transmission electron microscopy (TEM) imaging was performed by a JEOL JEM 2100 machine, operating at an accelerating voltage of 200 kV. In HRTEM measurement, a sliced specimen was first dispersed in the DI water, and then subjected to ultra-sonication for 1 h. Then, a micro drop of the sample was placed on the carbon coated copper grid for imaging purposes. The Raman spectra have been acquired by using a Renishaw In-Via Raman spectrometer (Renishaw, Wottonunder-Edge, UK) equipped with an Ar^+ laser line ($\lambda = 514.5$ nm) as the excitation source, and having a detector resolution of 0.3 cm^{-1}.

Table 1. Energy loss parameters for 80 MeV C^{6+} ions in the host matrix and target material systems.

Material	Electronic energy loss, S_e (eV/Å)	Nuclear energy loss, S_n (eV/Å)	Projectile range, R_p (μm)
PVA	27.91	1.528×10^{-2}	174.63
Gd_2O_3	78.31	4.319×10^{-2}	68.48

3. Results and discussion

3.1. Structural and morphological evolution

The XRD patterns of pristine and 80 MeV carbon-ion-irradiated Gd_2O_3 nanorods are shown in Figure 1(a)(i–iv). As can be found, the pristine nanorod powder is characterized by four prominent peaks located at $\sim$28.60°, 33.20°, 47.60° and 56.30° which corresponded to (222), (400), (440) and (622) crystallographic planes of the cubic phase (type-C) of the Gd_2O_3 system (JCPDS No. 11-0604) (21, 22). The PVA-dispersed Gd_2O_3 nanorods subjected to irradiation at moderate fluences gave relatively noisy diffraction peaks (Figure 1(a)(ii,iii)). However, sharp peaks are regained at very high fluence owing to recovery from matrix encapsuation (Figure 1(a)(iv)). Moreover, the diffraction peaks experienced a noticeable shifting toward higher Bragg angles owing to introduction of adequate strain in the system. The average crystallite size (d) and microstrain (η) can be calculated using the popular Williamson–Hall (W–H) expression:

$$\beta \cos \theta = 0.9\lambda/d + 4\eta \sin \theta, \qquad (1)$$

where β is the full width at half maxima (FWHM), θ is the diffraction angle in degrees and λ is the wavelength (1.543 Å) of the X-rays employed. While the average crystallite sizes vary in the range of 5.4–8.6 nm, the calculated microstrain is in of the order of 10^{-3}, the values being presented in Table 2.

Figure 1. (a) XRD patterns of the (i) pristine and irradiated Gd_2O_3 nanorods at fluences of (ii) 1×10^{11}, (iii) 3×10^{11} and (iv) 1×10^{12} ions/cm^2. The HRTEM imaging of (b) pristine and irradiated (c) 1×10^{11}, (d) 3×10^{11}, (e) 1×10^{12} and (f) 3×10^{12} ions/cm^2 Gd_2O_3 nanorods. The histograms, shown as figure inset, represent size distribution of the nanorods.

Table 2. Energy deposition and structural parameters associated with the Gd_2O_3 nanorods subjected to 80 MeV C^{6+} ion irradiation (through XRD and TEM analyses).

Ion fluence, φ (ions/cm^2)	Energy absorbed (J/cm^2)	Average crystallite size, d (nm)	Microstrain, ε ($\times 10^3$)	Lattice parameter (Å)	Average dimension of the nanorods		
					Length, L (nm)	Diameter, D (nm)	Aspect ratio (L/D)
0	0	6.46	−0.89	10.82	114	29	3.9
1×10^{11}	1.28	8.41	−1.55	10.78	83.9	17.9	4.6
3×10^{11}	3.84	5.68	−1.22	10.82	53	16	3.3
1×10^{12}	12.8	5.4	−7.9	10.53	34.9	9	3.8
3×10^{12}	38.4	–	–	–	74.1	20	3.7

The visual information as regards irradiation effect of Gd_2O_3 nanorods can be revealed in TEM micrographs, shown in Figure 1(b–f). The average diameter of the rods, for each fluence case, can be assessed from the figure-insets depicted in the form of histogram plots. With an average length (L) of ∼114 nm and diameter (D) of ∼29 nm, the un-irradiated rods gave an aspect ratio (L/D) of ∼3.9 (Figure 1(b)). When subjected to a low fluence (1×10^{11} ions/cm^2) irradiation, both the average length (∼83.9 nm) and diameter (∼18 nm) get substantially reduced along with their existence in the clustering form (Figure 1(c)). As the fluence is increased further (up to 1×10^{12} ions/cm^2), both the average length and diameter of the rods, experienced a declining trend along with pronounced bunching effect noticeable in the micrographs (Figure 1(c–e)). The fluence dependent alteration of dimension and aspect ratios are presented in Table 2. In particular, the aspect ratio of the irradiated Gd_2O_3 nanorods was observed to vary between ∼3.3 and 4.6 and without giving any definite trend with regard to altering of ion fluence (Table 2).

It is worth mentioning here that, the RE oxides are mechanically, chemically and thermally stable as compared to many conventional oxides. The irradiated nanorods, therefore, would not necessarily be melted wholly by the swift ion impact. But normal impact of the ions at the edges and surfaces of the nanorods could result in the dislodgement of atoms owing to sudden rise in temperature. Apparently, the ion induced massive transport of the atoms from the nanorod surfaces would lead to diminishing dimension of the Gd_2O_3 nanorods, which exist in the form of bunches. The number of bunching patterns is likely to increase with the ion fluence. This was attributed to the assimilation of interlocked nanorods that underwent significant surface shape deformation and occurred at a fluence of 1×10^{12} and 3×10^{12} ions/cm^2 (Figure 1(e,f)). The unusual development of tamarind-shaped Gd_2O_3 nanostructures is highlighted in an enlarged micrograph, shown in Figure 2(a,b). For the sake of comparison, the digital image of a few matured tamarinds has also been provided (Figure 2(c)). On a comparative note, the un-irradiated nanorod has a smooth surface, while the irradiated one experienced a bumpy surface, as can be found in Figure 2(d,e). Earlier banana-shaped nanorods were successfully produced through femtosecond laser irradiation (23). The authors also argued that, the twin-plane, single crystal structure of the nanorods with surface defects have facilitated on transforming it into polycrystalline particles (23). The transformation is likely to start at the surface and would then propagate into the interior of the nanorods. Sun et al. (24) have offered a qualitative account with regard to structural and shape evaluation of several RE oxides subjected to a plasma torch. To the best of our survey, no work has been directed to the shape modification of
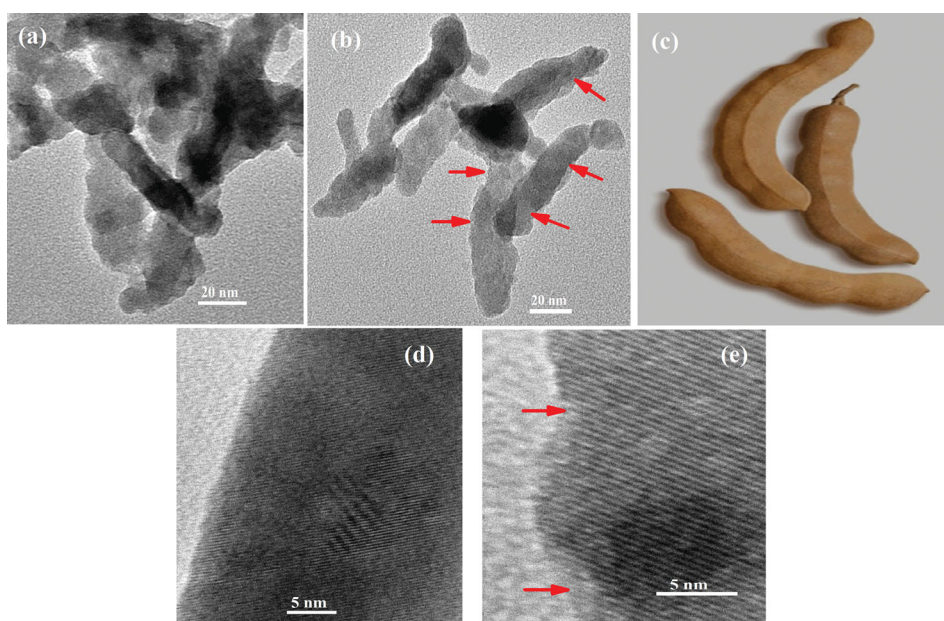
Figure 2. Tamarind-like shape evolution upon irradiation at a fluence of 1×10^{12} ions/cm^2 is depicted in (a), with regular deformation indicated by arrow marks for the case (b) 3×10^{12} ions/cm^2 and (c) image on real look of mature tamarinds (Source: http://www.in.all.biz/img/in/catalog/23346.jpeg). The smooth and bumpy surface features can be visualized in magnified TEM images meant for the (d) un-irradiated nanorod and the one (e) irradiated at a fluence of 1×10^{12} ions/cm^2.

one-dimensional RE oxides under MeV irradiation. In the present case, tamarind-like shape evolution is attributed to a collective effect that has arisen due to the ion induced variation of the internal strain and regular dislodgement of atoms from the nanorod surface structure. The shape evolution, as a result of multi-ion impact has also been deliberated separately towards the end of the discussion part.

3.2. Raman spectroscopy analysis

Raman spectroscopy is an effective tool to investigate the phononic modes within a system under study. According to factor group theory analysis the optical and acoustic mode of cubic RE oxide can be expressed by (25)

$$\Gamma_{op} = 4A_g + 4E_g + 14F_g + 5A_{2u} + 5E_u + 16F_u, \; \Gamma_{ac} = F_u, \tag{2}$$

where A_g, E_g and F_g are Raman active, F_u is IR active and A_{2u} and E_u are inactive modes. On the whole, 22 Raman modes have been predicted for the C-type RE sesquioxides (25). The Raman spectra of pristine and 80 MeV carbon-ion-irradiated Gd$_2$O$_3$ nanorods are depicted in Figure 3(a–c). In RE sesquioxides, the strong Raman bands are normally observed in the range $\sim$330–420 cm^{-1}. In the present case, apart from a strong peak positioned at $\sim$360 cm^{-1}, two subsidiary peaks can be found to be located at $\sim$313 and 446 cm^{-1} (Figure 3(a)). The peak at $\sim$313 cm^{-1} is attributed to the mixed modes of $F_g + E_g$ and the one at $\sim$446 cm^{-1} existed due to an independent Fg mode (26, 27). The most
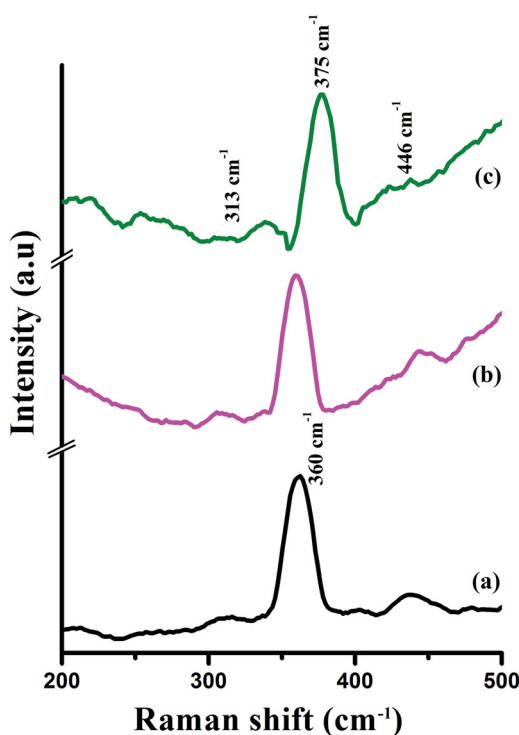
Figure 3. Raman spectra of (a) pristine, and irradiated Gd_2O_3 nanorods at a fluence of (b) 1×10^{12} and (c) 3×10^{12} ions/cm². Note the shifting of the prominent peak ($F_g + A_g$ mode) at the highest fluence.

prominent peak at $\sim 360\,cm^{-1}$ is assigned to the $F_g + A_g$ mode, that characterize a sustained mixed mode present in the cubic phase of Gd_2O_3 (*26*). Furthermore, the peak at $\sim 360\,cm^{-1}$ experiences a blue-shifting (to $\sim 375\,cm^{-1}$) after ion irradiation. Moreover, the FWHM of the Raman peak ($F_g + A_g$ mode) is slightly decreased from a magnitude of $\sim 21.7\,cm^{-1}$ to a value of $19.6\,cm^{-1}$ for the Gd_2O_3 nanorods irradiated at a very high fluence (3×10^{12} ions/cm²). At this ion fluence, the energy of deposition is extremely high ($38.4\,J/cm^2$) and thus can be responsible to bring in adequate surface deformation through overlapping impact of ions, yielding tamarind-like shape of nanorods (Figure 1(f)).

The assigned Raman active mode is likely to be upshifted due to inclusion of surface optic mode or other permissible low frequency modes. Previously, shifting of the Raman peak to high frequency side was assigned to the reduction of particle size (*28*). Since the post irradiated systems showed a significant reduction with regard to the length and diameter of the nanorods, phonon confinement is generally effective to cause the desired shift. Semiconductor oxides, which offer an ample source of oxygen vacancies were shown to be responsible for shifting and broadening of the Raman peak positions (*29*). Thus in Gd_2O_3 systems, role of oxygen vacancies for Raman peak shifting cannot be completely eluded. Owing to the generation of irradiation-led oxygen vacancies and dislodgement of atoms, the lattice is believed to be compressed locally at the nanorod surfaces. Consequently, phononic feature is manifested. The presence of oxygen defects has also been predicted through theoretical treatments discussed in the following Section 3.3.

3.3. Theoretical treatment on energy deposition

Let's consider an ideal, one-dimensional nanorod that consists of N number of atoms and that, the volume of the nanorod is equal to the total volume of the N atoms. If x_i ($i = 1, 2, 3 \ldots$) is the atomic percentage of each element of diameter d_i ($i = 1, 2, 3 \ldots$) present in the nanorod of diameter D and length L, then the number of atoms present in the nanorod will be given by (16)

$$N = \frac{1.5fD^2}{\sum x_i d_i^3} L,$$ (3)

where f is the packing fraction (≈ 0.68) of Gd_2O_3 (30) and $\sum x_i = 1$. Knowing the respective atomic diameters of gadolinium and oxygen as, 0.18 and 0.06 nm, we obtain $N = 53.68\,D^2L$.

It was believed that, the impact of an MeV scale ion will spread its energy while forming some cylindrical zones (16). If δ and l are the diameter and length of any cylindrical zone, then the number of atoms that would be present in it can be given by

$$n = \frac{N\delta^2 l}{D^2 L}.$$ (4)

The amount of energy deposited during the thermal spike event refers to the product of the electronic energy loss (S_e) and electron–phonon coupling efficiency (g). The total energy deposited along the path of the projectile ion is $gS_e l$ and the amount of energy received by each of the atoms in the cylindrical region of diameter δ can be expressed as

$$E = \frac{gS_e l}{N\delta^2 l/D^2 L},$$

or

$$E = \frac{gS_e D^2 L}{N\delta^2}.$$ (5)

Assuming $g \sim 0.4$ (31) and using Equation (5), the variation of the energy received per atom of the cylindrical regions can be plotted as a function of δ, which is shown in Figure 4(a).

Gd_2O_3 and yttrium oxide (Y_2O_3), which share a number of physical properties, are popular oxides in the family of RE sesquioxides. The respective lattice parameters (a) of cubic phase Gd_2O_3 and Y_2O_3 are, 10.79 and 10.60 Å (32). In Y_2O_3 system, the oxygen vacancy ($V\ddot{o}$) and yttrium vacancy (V_Y''') related formation energies are predicted as, ~ 20.31 and 47.37 eV, respectively (32). With an assumption that, the formation energy of yttrium and gadolinium vacancies (V_{Gd}''') are close, the above mentioned energies would correspond to the cylindrical regions of diameter (δ) ~ 0.53 and ~ 0.35 nm (indicated by * marks in Figure 4(a)). Since the number of atoms, n, present in the effective cylindrical region is directly proportional to the square of diameter, δ as per Equation (4), oxygen-related defects are manifested to a great extent.

3.4. Mechanism of formation of tamarind-shaped nanorods at a higher fluence

During irradiation both the matrix as well as (dispersed) nanoscale objects experience the impact of ions differently and to different extent. While polymer is believed to be damaged at high fluences, it is only the inorganic solid-state object which matters the most after
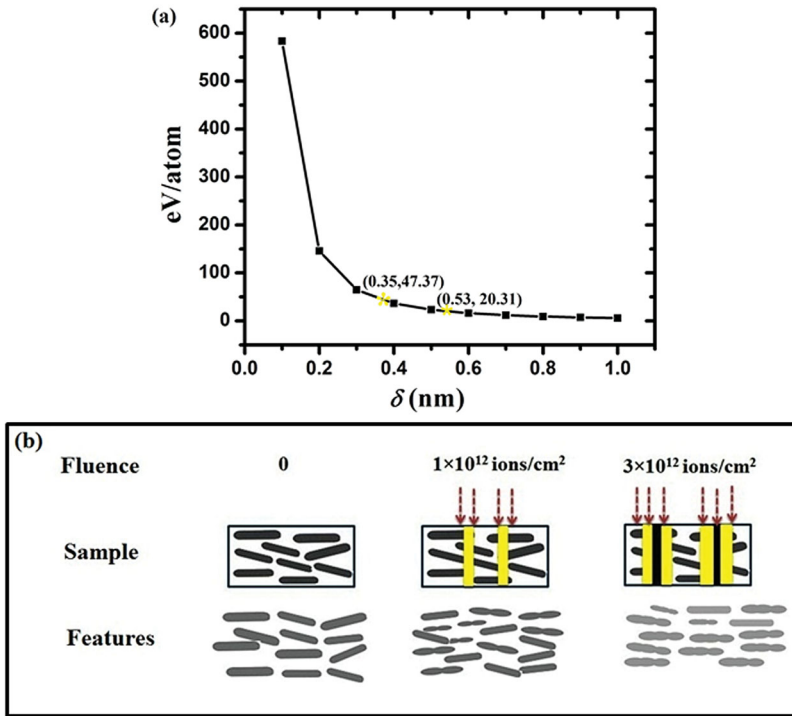
Figure 4. (a) Variation of energy deposited per atom during irradiation vs. effective diameter of the cylindrical zones created due to swift ion impact and (b) scheme illustrating the shape evolution of Gd_2O_3 nanorods in overlapping regions of influence caused by impact of multiple ions.

irradiation. Earlier, ion irradiation-led structural transition and shape evolution have been discussed independently in Gd_2O_3 and Gd_2TiO_5 systems (*18, 33*). It is known that, a swift heavy ion while traversing through a material system, is capable of creating an ion track of typical diameter ~ 5 nm (*8*). In the recent past, also amorphous latent tracks of diameter ~ 5 nm have been witnessed due to 74 MeV Kr ion irradiation on $Y_2Ti_2O_7$ nanoparticles in EP450 ODS steel (*34*).

In the present case, assuming that the nanorods are spread uniformly all throughout the matrix and remain normal to the ion impact, each of the nanorods is expected to receive quite uniform amount of ion exposure. Referring to the 1st fluence (1×10^{11} ions/cm^2), each of the nanorods is to receive about 11 independent normal impacts. Since the pristine nanorods are of approximate length ~ 116 nm, the impact of incoming ions is likely to affect only up to ~ 55 nm of its total length (assuming the region of influence on the nanorod surface as ~ 5 nm). This is, essentially suggest single ion impact feature with a fairly low chance of overlapping effect (multi-ion impact). In this case, no shape deformation is predicted as evident from the HRTEM image (Figure 1(c)). On a quantitative note, the respective number of ion impacts as for the 2nd (3×10^{11}), 3rd (1×10^{12}) and 4th (3×10^{12} ions/cm^2) fluences are ~ 32, 105 and 317. Accordingly, with an increasing fluence, the effective region of influence over the nanorod length can be increased to ~ 160, 525 and 1585 nm, provided that the single ion impact is ensured. But, since the apparent length

of the nanorods is much shorter a strong overlapping effect can be realized at very high (especially, 3rd and 4th) fluences causing multi-ion impact mechanism to hold (Figure 4(b)). In contrast to the single ion impact regions, the multi-ion impact-led overlapping of regions of influence at the nanorod surface sites is chiefly responsible for the dislodgement of sufficiently large number of atoms at regular intervals. Consequently, in view of flying off the surface atoms from the impact zones, the shape is deformed locally yet in regular intervals. The multi-impact region may also experience localized pressure effect and contributing to shape manifestation. The overall impact on the nanorods give rise to aperiodic, distorted morphology which resemble tamarind-like shape evolution (Figure 2(a,b)). The schematic representation on the manifested shape evolution of the Gd_2O_3 nanorods has been illustrated in Figure 4(b).

4. Conclusions

The impact of 80 MeV C^{6+} ions on the morphological evolution of one-dimensional Gd_2O_3 nanorods has been demonstrated along with a brief theoretical account. With an aspect ratio varying between 3.3 and 4.7, the nanorods were found to experience local shape deformation when subjected to irradiation at higher fluences. The unusual surface deformation occurred for fluences $> 1 \times 10^{12}$ ions/cm^2 and resulted in tamarind-like shape evolution. In the Raman spectra, a prominent Raman peak located at ~ 360 cm^{-1} and assigned to the $F_g + A_g$ mode, get blue-shifted for the nanorods irradiated at very high fluence (3×10^{12} ions/cm^2). Irradiation-induced modified characteristics in thermally and mechanically stable oxide systems will find immense scope in nanoscale mechanics, electronics and hybrid photonics where surface reconstruction and shape evolution form the basis for control and optimization. More rigorous study in this direction is needed to unravel underlying mechanism for controlling surface pattern generation and manipulation in a precise manner.

Disclosure statement

No potential conflict of interest was reported by the authors.

ORCID

Dambarudhar Mohanta 🆔 http://orcid.org/0000-0002-1750-7620

References

(1) Hasegawa, Y.; Thongchant, S.; Wada, Y.; Tanaka, H.; Kawai, T.; Sakata, T.; Mori, H.; Yanagida, S. *Angew. Chem.* **2002,** *114,* 2177.

(2) Xu, Z.; Yang, J.; Hou, Z.; Li, C.; Zhang, C.; Huang, S.; Lin, J. *Mater. Res. Bull.* **2009,** *44,* 1850.

(3) Paek, J.; Lee, C.H.; Choi, J.; Choi, S-Y; Kim, A.; Lee, J.W.; Lee, K. *Cryst. Growth Des.* **2007,** *7,* 1378.

(4) Tang, M.; Lu, P.; Valdez, J.A.; Sickafus, K.E. *J. Appl. Phys.* **2006,** *99,* 063514.

(5) Sickafus, K.E.; Grimes, R.W.; Valdez, J.A.; Cleave, A.; Tang, M.; Ishimaru, M.; Corish, S.M.; Stanek, C.R.; Uberuaga, B.P. *Nat. Mater.* **2007,** *6,* 217.

(6) Zhou, L.; Gu, Z.; Liu, X.; Yin, W.; Tian, G.; Yan, L.; Jin, S.; Ren, W.; Xing, G.; Li, W.; Chang, X.; Hu, Z.; Zhao, Y. *J. Mat. Chem.* **2012,** *22,* 966.

(7) Park, J.Y.; Baek, M.J.; Choi, E.S.; Woo, S.; Kim, J.H.; Kim, T.J.; Jung, J.C.; Chae, K.S.; Chang, Y.; Lee, G.H. *ACS Nano* **2009,** *3,* 3663.

(8) Fleischer, R.L.; Price, P.B.; Walker, R.M., Eds. *Nuclear Tracks in Solids*; University of California Press: Berkeley, CA, **1975**.

(9) Nastasi, M.; Mayer, J.W.; Wang, Y. *Ion Beam Analysis: Fundamentals and Applications*; CRC Press: Boca Raton, **2014**.

(10) Mohanta, D.; Nath, S.S.; Bordoloi, A.; Choudhury, A.; Dolui, S.K.; Mishra, N.C. *J. Appl. Phys.* **2002,** *92* (12), 7149.

(11) Bayan, S.; Mohanta, D. *Phys. E: Low-Dimen. Syst. Nanostruct.* **2013,** *54,* 288.

(12) Lian, J.; Zhou, W.; Wei, Q.M.; Wang, L.M.; Boatner, L.A.; Ewing, R.C. *Appl. Phys. Lett.* **2006,** *88,* 093112.

(13) Carter, G.; Vishnyakov, V. *Phys. Rev. B.* **1996,** *54,* 17647.

(14) Valbusa, U.; Boragno, C.; de Mongeot, F.B. *J. Phys.: Cond. Matt.* **2002,** *14,* 8153.

(15) Malchukova, E.; Boizot, B.; Petite, G.; Ghaleb, D. *Euro. Phys. J.: Appl. Phys.* **2009,** *45* (1), 10701.

(16) Bayan, S.; Mohanta, D. *Nuclr. Instrum. Methods B.* **2011,** *269,* 374.

(17) Lee, J.; Lear, C.R.; Zhang, X.; Bellon, P.; Averback, R.S. *Metal. Mater. Trans. A.* **2015,** *46,* 1046.

(18) Antic, B.; Kremenovic, A.; Draganic, I.; Colomban, Ph.; Vasiljevic-Radovic, D.; Blanusa, J.; Tadic, M.; Mitric, M. *Appl. Surf. Sci.* **2009,** *255,* 7601.

(19) Paul, N.; Devi, M.; Mohanta, D. *Mater. Res. Bull.* **2011,** *46,* 1296.

(20) Zeigler, J.F.; Zeigler, M.D.; Biersack, J.P. *SRIM (2008) – The Stopping and Range of Ions in Matter 2008*. www.srim.org.

(21) Du, P.; Song, L.; Xiong, J.; Xi, Z.; Jin D.; Wang, L. *Nanotechnology.* **2011,** *22,* 035602.

(22) Hazarika, S.; Mohanta, D. *Eur. Phys. J. Appl. Phys.* **2013,** *62,* 30401.

(23) Gordel, M.; Olesiak-Banska, J.; Matczyszyn, K.; Nogues, C.; Buckle, M.; Samoc, M. *Phys. Chem. Chem. Phys.* **2014,** *16,* 71.

(24) Sun, X.L.; Tok, A.I.Y.; Huebner, R.; Boey, F.Y.C. *J. Europ. Ceram. Soc.* **2007,** *27,* 125.

(25) Ubaldini, A.; Carnasciali, M.M. *J. Alloys Comp.* **2008,** *454,* 374.

(26) Rajan, G.; Gopchandran, K.G. *Appl. Surf. Sci.* **2009,** *255,* 9112.

(27) Paul, N.; Mohanta, D. *Appl. Phys A.* **2016,** *122,* 845.

(28) Choi, H.C.; Jung, Y.M.; Kim, S.B. *Vib. Spectr.* **2005,** *37,* 33.

(29) Parker, J.C.; Siegel, R.W. *Appl. Phys. Lett.* **1990,** *57,* 943.

(30) Jacobsohn, L.G.; Bennett, B.L.; Muenchausen, R.E.; Tornga, S.C.; Thompson, J.D.; Ugurlu, O.; Cooke, D.W.; Lima Sharma, A.L. *J. Appl. Phys.* **2008,** *103,* 104303.

(31) Szenes, G.; Pászti, F.; Péter, Á.; Popov, A.I. *Nuclr. Instrum. Methods B.* **2000,** *166–167,* 949.

(32) Putilov, L.P.; Varaksin, A.N.; Tsidilkovski, V.I. *J. Phys. Chem. Sol.* **2011,** *72,* 1090.

(33) Zhang, J.; Zhang, F.; Lang, M.; Lu, F.; Lian, J.; Ewing, R.C. *Acta. Mater.* **2013,** *61,* 4191.

(34) Monnet, I.; Grygiel, C.; Lescoat, M.L.; Ribis, J. *J. Nuclr. Mater.* **2012,** *424,* 12.

Applied Physics A
Materials Science & Processing

CrossMark

Noticeable red emission and Raman active modes in nanoscale gadolinium oxyfluoride (Gd$_4$O$_3$F$_6$) systems with Eu^{3+} inclusion

Samiran Hazarika[1] · **Dambarudhar Mohanta**[1]

Abstract Eu^{3+} doped gadolinium oxyfluoride (Gd$_4$O$_3$F$_6$, GOF) nanoscale systems have been synthesized following a modified Pechini method. While exhibiting a tetragonal crystal structure, the GOF nanosystem gave an average crystallite size (d) of $\sim$21–26 nm. The Lotgering factor (L_F), which is a measure of orientation of crystallites along the preferred direction was found to vary between 0.22 and 0.48. In the photoluminescence spectra, $\sim$595 and $\sim$613 nm peaks were identified as magnetically driven ($^5D_0 \rightarrow {}^7F_1$) and electrically driven ($^5D_0 \rightarrow {}^7F_2$) transitions with latter (red emission) being strongly manifested with Eu^{3+} doping concentration and intrinsic defects. Moreover, several Raman active modes have been probed in the Raman spectra with low frequency peaks ($<$300 cm^{-1}) and moderate frequency peaks ($\sim$481 and 567 cm^{-1}) assigned to observable vibration of heavy atom Gd–Gd pairs and Gd–O groups, respectively. Apart from manifestation of phononic features, inclusion of Eu^{3+} in the host lattice would bring new insight on improving the red emission response prior to concentration quenching.

1 Introduction

Though scarcely available in the earth crust, rare earth (RE) elements are known for their extraordinary quality and durability under extreme conditions. The non-radiative lanthanides, especially in the form of oxides and sulfides offer immense potential due to their unique electrical, optical and photoluminescence properties. For instance, the role of Y$_2$O$_3$ is inevitable for making YBCO type superconductors and also in the deployment of solid-state lasers. On the other hand, the use of Er$_2$O$_3$ in the design consideration of display monitors and optical fibers is noteworthy. Similarly, the importance of EuS is unforgettable when it comes to making of insulating ferromagnets, ferromagnetic semiconductors, laser window materials, etc. Additionally, rare–earth fluorides (REF) and oxyfluorides (REOF) have received a great deal of attention owing to their unique optical, electrical, electrochemical responses, thus making their role indispensable in specific optoelectronic, photonic and sensing devices [1–3]. To improve biomedical imaging and contrast, emphasis is also given to RE based nano-dimensional luminescent agents [4, 5]. The RE fluorides are known to be efficient luminescent hosts, as they are characterized by low phonon energy and consequently, display luminescence due to the low probability of multi-phonon non-radiative processes [6, 7]. The lanthanide oxyfluoride, while exhibiting high ionicity, thermal and chemical stability can act as a suitable host as it could easily accommodate luminescent lanthanide ions as dopants. Earlier numerous studies were focused to synthesize Eu^{3+} (or Tb^{3+}) doped lanthanum, gadolinium and yttrium oxyfluorides [8, 9] in bulk form, or in thin film form [10]. Moreover, Eu^{3+} doped gadolinium oxyfluoride (Gd$_4$O$_3$F$_6$, GOF) nanoparticles have been synthesized in an amorphous media, like silica matrix [11]. The oxyfluoride glass has also been employed to accommodate crystalline materials [12]. A comparative account on the upconversion responses of Er^{3+}, Tm^{3+}, Yb^{3+} doped GOF nanoparticles has been reported in a previous work [13], whereas, a modified crystal structure along with manifested

✉ Dambarudhar Mohanta
best@tezu.ernet.in

1   Nanoscience and Soft Matter Laboratory, Department of Physics, Tezpur University, PO: Napaam, Tezpur, Assam 784028, India

luminescence characteristics was realized in Eu^{3+} doped GOF systems [14].

In the past, sol–gel [14, 15] and hydrothermal [16, 17] techniques have been employed to synthesize RE oxyfluorides. Often, the methods either rely on annealing of REF_3 in air atmosphere or allow a solid-state reaction between RE_2O_3 and REF_3 or, NH_4F. While every route has its own advantage and shortcoming, a reliable strategy that avoids punitive reaction environment and complicated aspects is generally accepted for synthesis and large scale production. The present study highlights processing of a matrix-free, RE oxyfluoride nanoscale system (e.g., Eu^{3+} doped $Gd_4O_3F_6$) following a modified Pechini method. The microstructural, radiative emission response, vibrational, and Raman active modes are discussed in this work.

2 Experimental: materials and methods

2.1 Synthesis procedure

To synthesize nanoscale $Gd_4O_3F_6$ system, a modified Pechini method has been adopted [14]. In a typical procedure, 0.28 g of bulk Gd_2O_3 (Otto, 99.9% purity) is first dispersed in 35 ml deionized water followed by addition of an appropriate amount of dil. HNO_3 and until a clear sol is obtained. Then 3.6 g of citric acid ($C_6H_8O_7$, CDH, 99% purity) and 0.6 ml of ethylene glycol ($C_2H_6O_2$, Merck, 99% purity) are refluxed with the as-prepared sol. To inhibit precipitation, citric acid was added in excess amount. During rigorous stirring (~ 300 rpm), aqueous ammonium fluoride (NH_4F, Merck, 99% purity) was gently mixed with the aforesaid solution. The as-prepared sol was cleansed several times, first with distilled water and then with ethanol, and subsequently oven-dried at a temperature of 70 °C. Finally, the prepared precursor was subjected to annealing at a temperature of 500 °C, for 2 h. For synthesizing Eu^{3+} doped GOF product, an appropriate amount of europium oxide (Eu_2O_3, Otto, 99.9% purity) was added to the chamber during the initial step of the reaction, whereas, rest of the steps remained unchanged. To synthesize different GOF nanosystems with typical Eu doping concentrations (e.g., 3, 5 and 7%), 0.0084, 0.0075, and 0.0196 g of Eu_2O_3 were taken with proportionate amount of bulk Gd_2O_3 powder. The purpose of Eu^{3+} doping was to manifest optical and vibrational characteristics with regard to pure GOF system.

2.2 Characterization tools and techniques

Structural and crystallographic information were revealed by a Rigaku miniFlex X-ray diffractometer (XRD) that is equipped with a CuK_α source ($\lambda = 1.54$ Å). The diffraction angle (2θ) was varied in the range of 20°–60° and data acquisition were made in steps of 0.05°. Transmission electron microscopy (TEM) imaging was performed on a TECNAI G2 20 S-TWIN machine, operating at an accelerating voltage of 200 kV. The optical absorption study was carried out on a UV–Visible-NIR spectrophotometer (UV 2450, Shimadzu). On the other hand, room temperature photoluminescence response has been revealed by a PerkinElmer LS 55 spectrophotometer. Moreover, molecular vibrational characteristics were exploited through Fourier transform infrared spectroscopy (FT-IR, Nicolet Impact 410). In contrast, Raman active vibrational modes have been acquired with the help of a high precision Raman spectrometer (Horiba Jobin Vyon, LabRam HR) and employing a red diode laser ($\lambda_{ex} = 632$ nm) as the excitation source. All the measurements were carried out at room temperature (300 K).
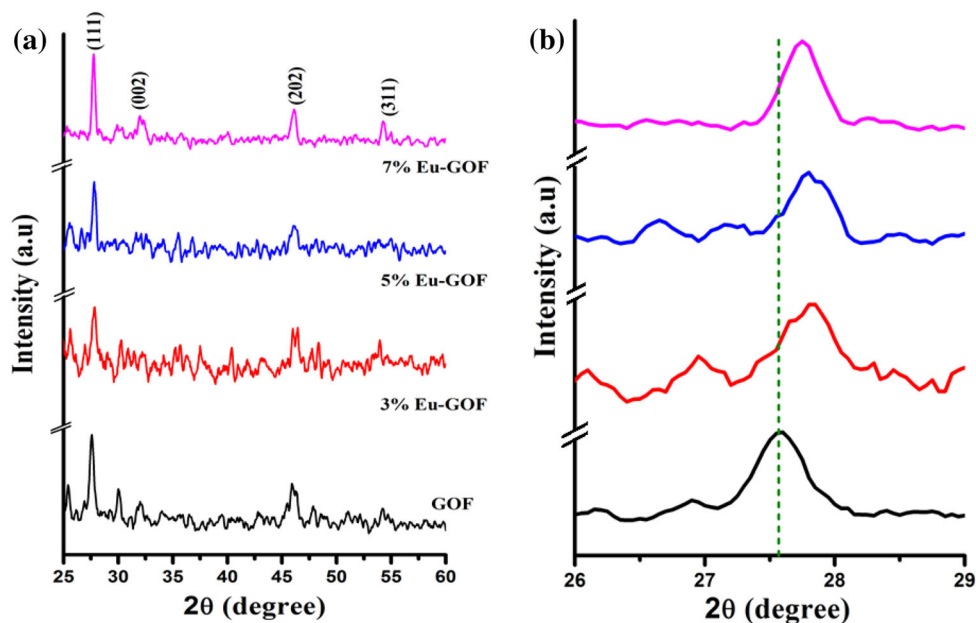
3 Results and discussion

The structural, optical, IR active and Raman active vibrational characteristics of the undoped and Eu^{3+} doped GOF nanosystems are as discussed below.

3.1 Structural and morphological analyses along with degree of orientation aspect

XRD patterns of the undoped and Eu^{3+} doped $Gd_4O_3F_6$ nanoparticles are shown in Fig. 1. The four diffraction peaks located at $\sim 27.65°$, 32.30°, 46.20°, and 54.35° corresponded to (111), (002), (202) and (311) crystallographic planes (JCPDS No. 76-0155) [13]. With a preferred crystallographic orientation along the (111) plane, the diffractograms characterize a tetragonal crystal structure of the $Gd_4O_3F_6$ system [13]. An appreciable peak-shifting can also be noticed in case of Eu^{3+} doped GOF nanosystems, thereby indicating possible changes in microstrain and lattice parameter after incorporation of Eu^{3+} into the host lattice [18]. The average crystallite size (d) can be calculated by employing single line fitting of the preferred (111) peak and using the Scherrer expression: $d = 0.91 \, \lambda / \beta \cos \theta$, where β is the full width at half maxima (FWHM), 2θ is the diffraction angle in degrees and λ is the wavelength of the X-rays (1.543 Å). The lattice parameters are computed using a formula which relates inter-planar spacing and parameters that satisfy 1st order diffraction ($2d_{hkl} \sin \theta = \lambda$) while exhibiting tetragonal symmetry. We write,

$$\frac{1}{d_{hkl}^2} = \frac{h^2 + k^2}{a^2} + \frac{l^2}{c^2}, \qquad (1)$$

Fig. 1 **a** XRD patterns of undoped and Eu^{3+} doped Gd$_4$O$_3$F$_6$ nanosystems, **b** zoomed version of the XRD patterns to highlight peak-shifting with Eu^{3+} doping

where d_{hkl} is the inter-planar spacing for the (hkl) plane (h, k and l are Miller indices), a ($=b$) and c represent lattice parameters of the tetragonal unit cell. The average crystallite size and lattice parameters are estimated from the diffraction data and are presented in Table 1.

To make a quantitative assessment of degree of orientation normally Lotgering factor is introduced. The Lotgering factor, L_F is based on the evaluation between the measured XRD patterns and that expected for the randomly oriented powders. In reference to a specific crystallographic plane, the L_F is defined as [19]:

$$L_F(hkl) = \frac{P(hkl) - P_o(hkl)}{1 - P_o(hkl)}. \qquad (2)$$

Here $P(hkl)$ is the ratio of the XRD intensity of (hkl) reflection over the scanned range, and $P_o(hkl)$ is an equivalent value for a randomly oriented Gd$_4$O$_3$F$_6$ system (JCPDS file No. 76-0155) [13]. The L_F would vary from a value 0, for a non-orientation case to ~ 1, for complete orientation. In reference to (111) peaks, the L_F value is found to increase from a value of 0.20–0.48 with increasing

Eu^{3+} content (Table 1). In other words, inclusion of Eu^{3+} ions into the host would facilitate orientation of the crystallites along the preferred direction. Consequently, a higher L_F value is witnessed.

The TEM images of the undoped and 7% Eu^{3+} doped Gd$_4$O$_3$F$_6$ nanosystems are shown in Fig. 2a, b. Both the undoped and doped systems showed the presence of spheroidal particles with occasional instances of sharp edges, indicated by short arrows. The average dimension of the GOF nanoparticles is ~ 30–45 nm. Figure 2c depicts an isolated nanoparticle with prominent lattice fringe pattern. The inter-planar spacing is estimated to be ~ 0.31 nm which corresponds to the (111) crystallographic plane of the tetragonal GOF system. The EDX patterns of the undoped and 7% Eu^{3+} doped nanosystems are shown in Fig. 2d. Apart from signals corresponding to Gd, O, and F elements; a peak due to the Eu dopant is distinctly observable for the doped system. A prominent peak due to Cu has arisen due to the fact that the GOF specimen was loaded on a copper grid for the EDX measurements. Nevertheless, all other peaks due to presence of prime elements are observable at large.

Table 1 Physical parameters derived through XRD analyses of Eu^{3+} doped Gd$_4$O$_3$F$_6$ nanosystems

% Eu	Average crystallite size, d (nm)	Lattice parameter (Å)		Lotgering factor (L_F)
		a	c	
0	25.1	5.54	5.57	0.20
3	21.2	5.48	5.58	0.22
5	22.1	5.50	5.58	0.24
7	26.1	5.57	5.53	0.48

Fig. 2 **a** HRTEM images of $Gd_4O_3F_6$ (GOF) nanoparticles, and **b** 7% Eu^{3+} doped GOF sample, **c** an isolated GOF nanoparticle illustrating lattice fringe pattern, **d** EDX patterns of (*lower*) undoped and (*upper*) 7% Eu^{3+} doped GOF specimens
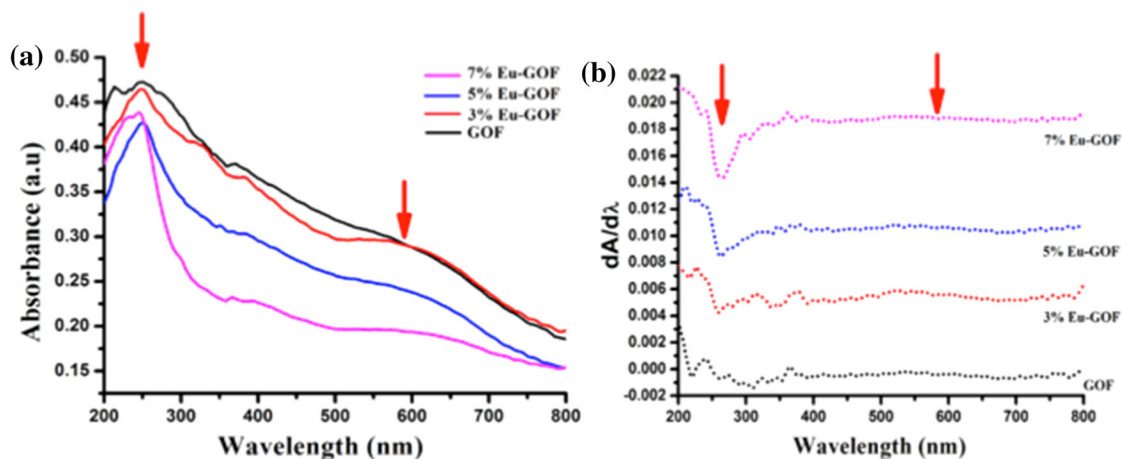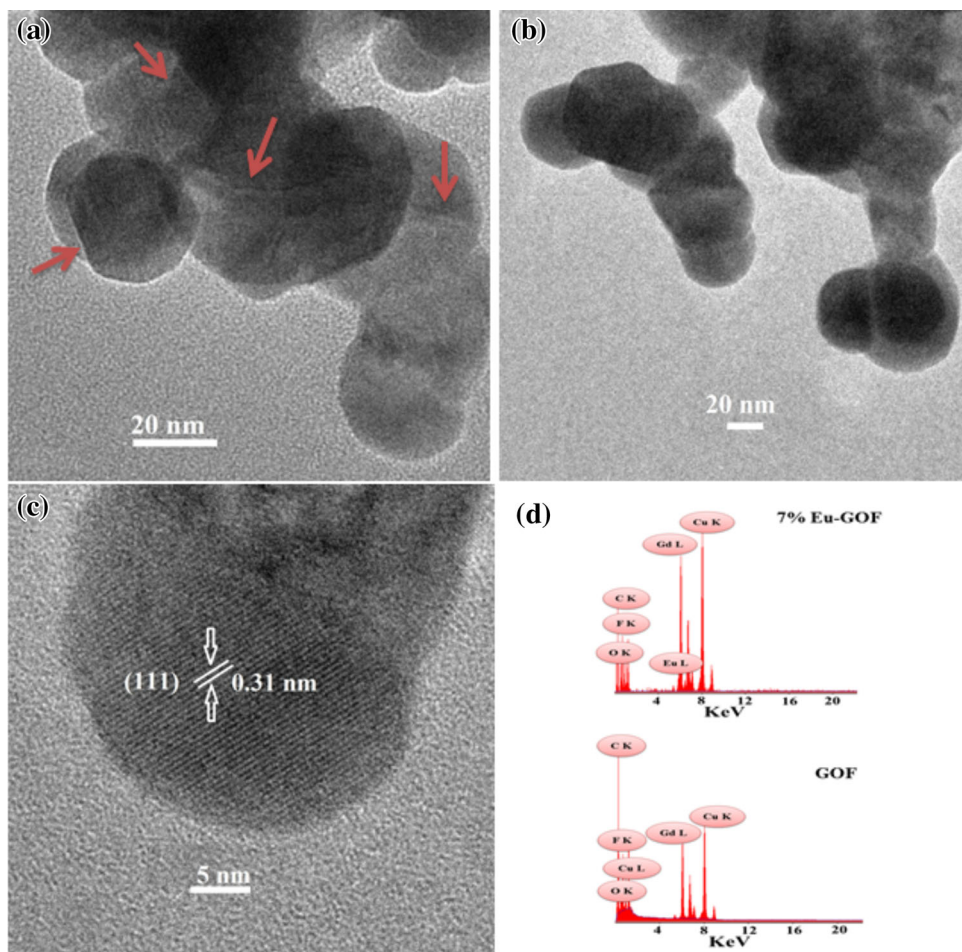

Fig. 3 **a** Optical absorption spectra of the undoped and Eu^{3+} doped $Gd_4O_3F_6$ nanosystems, **b** corresponding first derivative spectra of the samples

3.2 Optical absorption and photoluminescence responses with emphasis on $D \rightarrow F$ transitions

Figure 3a shows the optical absorption spectra of the synthesized $Gd_4O_3F_6$ nanosystems. As can be found, the absorption spectra of the undoped and Eu^{3+} doped GOF nanoparticles depict a broad absorption feature over a wide range of wavelength. The absorption peak at ~ 248 nm is due to the one of the transition of Gd^{3+} corresponding to $^8S_{7/2} \rightarrow {}^6I_{j/2}$ multiplets (where, $j = 9,12,13,15$ and 17). To

be specific, the Eu^{3+} doped nanosystems are essentially characterized by two broad peak maxima, located at ~ 252 and ~ 590 nm. The peak at ~ 590 nm can be assigned to the magnetically driven $^5D_0 \rightarrow {}^7F_1$ transitions [20]. It may be noted that, Gd^{3+} has [Xe] $4f^7$ configuration, which means that it has half-filled shells and having a $^8S_{7/2}$ ground state [21]. The energy absorption in Gd is mediated via transition of $4f$ electrons to $5d$ level. The seven electrons in the $4f$ orbitals of Gd can have as many as 3432 multiplets with the ground state represented by $^8S_{7/2}$. Among these multiplets the low lying multiplet above the ground state is $^6P_{7/2}$ [21]. While the undoped system gives a nearly featureless characteristics over a broad spectrum, inclusion of Eu^{3+} ions into the GOF host offered distinct absorption features owing to introduction of localized states. The individual absorption bands, that illustrate strong absorption signature, could also be identified in the first derivative spectra (Fig. 3b).

Figure 4a depicts a series of the photoluminescence emission spectra ($\lambda_{\mathrm{ex}} = 400$ nm) of nanoscale GOF systems without and with inclusion of Eu^{3+} ions (3, 5, and 7%). Upon excitation, strong emission has been revealed at ~ 490, ~ 572, ~ 595, and ~ 613 nm, which can be ascribed to substantial $D \rightarrow F$ transitions accompanied by Eu^{3+} ions. The peak positions were identified through multi-peak Gaussian fitting of the overall spectrum. In this process, the area under the experimental curve is kept equal to the area under the empirical curve, which is the sum total of the area under each of the deconvoluted curves. A normalized Gaussian fitting of 3% Eu^{3+} doped GOF nanosystem can be found in Fig. 4b. Here, the ~ 490 nm emission peak can be assigned to the higher energy level (f–f) transitions of Eu^{3+} [20]. The respective peak maxima at ~ 572 nm, 595 nm and 613 nm would correspond to $^5D_0 \rightarrow {}^7F_0$, $^5D_0 \rightarrow {}^7F_1$, $^5D_0 \rightarrow {}^7F_2$ transitions of Eu^{3+} ions [20]. The schematic energy diagram that illustrates possible transitions is highlighted schematically, in Fig. 4c. It may be noted that, $^5D_0 \rightarrow {}^7F_1$ transition originates from magnetic dipole transition and it is permitted only on the condition that the Eu^{3+} ion occupies a site with an inversion center and is not dependent on the site symmetry. Whereas, $^5D_0 \rightarrow {}^7F_2$ transition is associated with the electric dipole
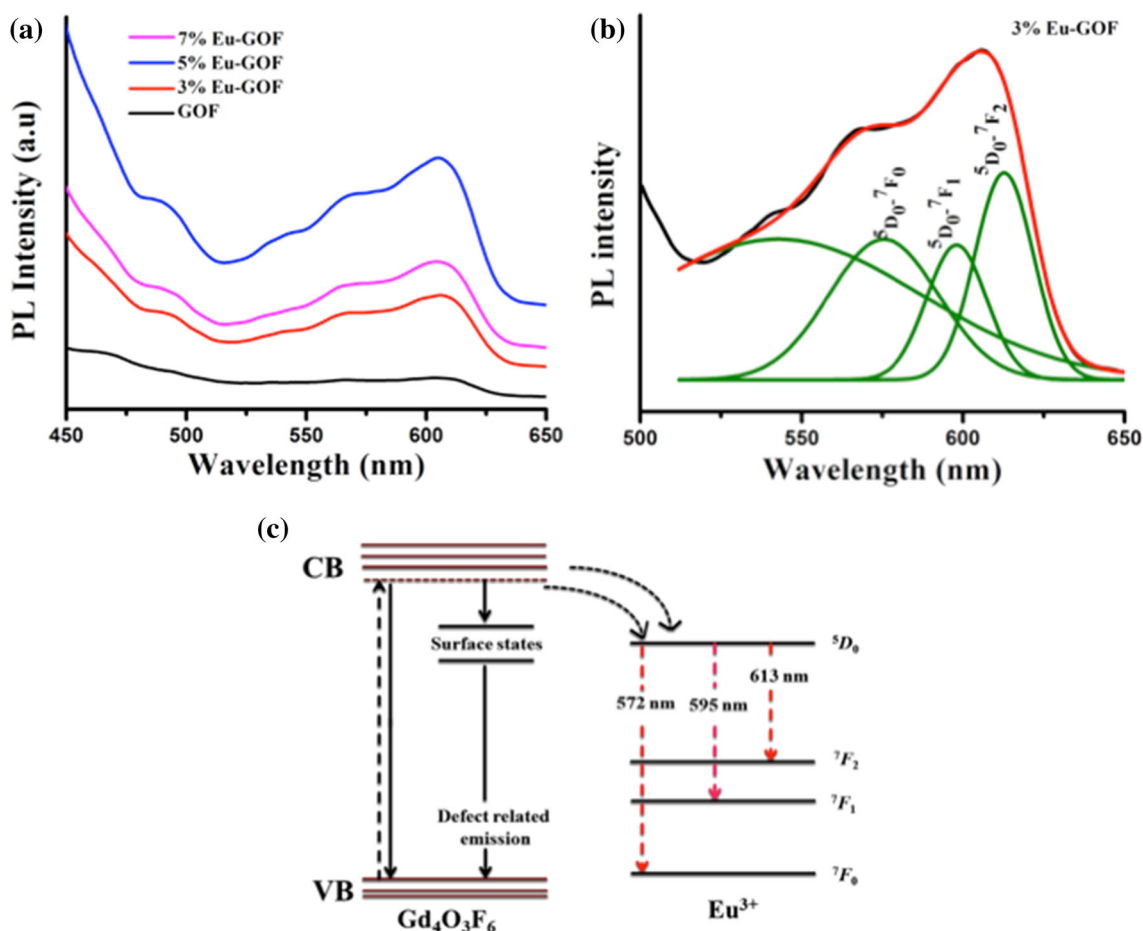

Fig. 4 **a** PL emission spectra ($\lambda_{\mathrm{ex}} = 400$ nm) of the undoped and Eu^{3+} doped GOF nanosystems. The deconvoluted PL curves of 3% Eu^{3+} doped GOF nanosystem is shown in (**b**). The schematic diagram as regards various radiative transitions is illustrated in figure (**c**)

transition and is allowed only when Eu^{3+} is occupied in low symmetries without any center of inversion. Consequently, it is hypersensitive to the environmental effect. The intensities of $^5D_0 \rightarrow {}^7F_1$ and $^5D_0 \rightarrow {}^7F_2$ mediated emissions, for different Eu^{3+} concentrations, are computed from the integrated area under each of the deconvoluted curves, e.g., in the range of 572–625 and 586–638 nm, respectively. In general, transition metal and rare–earth oxides possess numerous defects, which give emissions through non-radiative pathways. Moreover, since the rare earth oxides and oxyfluorides feature similar Gd–O networks, there can be ample surface defects common to both these systems. Apparently, the emission peak at ~610 nm can be due to surface defects (like, Schottky and Frenkel types) reported for gadolinium oxide nanoscale system [22]. With Eu doping, the emission intensity increases because of the overlapping contributions of the defect emission and $^5D_0 \rightarrow {}^7F_2$ transitions of Eu^{3+}, located at 613 nm. However, in case of a higher doping level (7% Eu^{3+}), the ~613 nm red emission peak declines considerably as a result of concentration quenching. At a relatively low doping level, the quenching effect is insignificant because of the fact that, (1) Eu^{3+} could easily occupy Gd^{3+} sites of the $Gd_4O_3F_6$ lattice owing to similar ionic radii of both the ion types, (2) the Eu–Eu interionic distance is fairly large to retain the radiative events. The quenching effect comes from the cross relaxation among Eu^{3+} ions which increases with decreasing distance between Eu^{3+} and Eu^{3+} ions [20]. The asymmetric ratio (A_{sy}) which is defined as the ratio of integrated intensities of electric dipole transition to the magnetic dipole transition experiences a marginal drop from 1.36 to 1.25 with increasing Eu^{3+} content (Table 2). A suppressed value of A_{sy} at a higher doping level could have arisen due to concentration quenching effect.

To assess the influence of local environment and bonding in the proximity of a RE ion, Judd–Ofelt (J–O) intensity parameter, Ω_J ($J = 2$) has been calculated. Essentially, Ω_2 characterizes a short range parameter that gives information about the degree of covalency and polarizability of chemical environment experienced by the RE ions. The radiative emission rate and intensity of emission corresponding to $^5D_0 \rightarrow {}^7F_2$ transition can be formulated as [23]:

Table 2 Judd-Ofelt intensity parameters (Ω_2) and asymmetric parameters obtained from the PL spectra

Samples	Ω_2 (10^{-20} cm^2)	Asymmetric ratio, A_{sy}
3%Eu^{3+}:Gd$_4$O$_3$F$_6$	3.21	1.36
5%Eu^{3+}:Gd$_4$O$_3$F$_6$	2.91	1.30
7%Eu^{3+}:Gd$_4$O$_3$F$_6$	2.65	1.25

$$A_{0-J} = A_{0-1} \frac{I_{0-J}}{I_{0-1}} \frac{hv_{0-1}}{hv_{0-J}}, \tag{3}$$

where I_{0-1} and I_{0-J} are integral intensities for $^5D_0 \rightarrow {}^7F_1$ (pure magnetic dipole) and $^5D_0 \rightarrow {}^7F_J$ transitions and hv_{0-1} and hv_{0-J} are associated energies (in cm^{-1}), respectively. Note that magnetic dipole transition $^5D_0 \rightarrow {}^7F_1$ is not much affected by the local environment and its transition rate is constant with an approximate value of 50 s^{-1}. On the other hand, the electric dipole transitions $^5D_0 \rightarrow {}^7F_J$ ($J = 2$, 4 and 6) are expressed as [23]

$$A_{0-J} = \frac{64\pi^4 e^2 K^3}{3h(2J+1)} \frac{n(n^2+2)^2}{9} \sum \Omega_\lambda <\psi J |U^\lambda| \psi' J' >^2. \tag{4}$$

Here n is the refractive index of the medium, e is the electronic charge, K is the transition energy of the electric dipole transitions in cm^{-1}, Ω_λ is the J–O intensity parameter and $<\psi J|U^\lambda|\psi' J'>^2$ values are the squared reduced matrix elements whose values are 0.0032 and 0.0023 for $J' = 2$ and 4, respectively [23]. A relatively high value of Ω_2 in case of 3% Eu^{3+} doped GOF sample indicate a strong asymmetric environment of the dopant ions in the host (Table 2).

3.3 IR active vibrational characteristics

FT-IR spectra of the undoped and Eu^{3+} doped $Gd_4O_3F_6$ nanoparticles are highlighted in Fig. 5. The data were acquired within a wavenumber range 400–4000 cm^{-1}. In the spectra, several IR active bands have been resolved at ~452, 512, 734, 1016, 1317, 1640, 2915, and 3432 cm^{-1}. The prominent bands at ~3432 and 1640 cm^{-1} are attributed to the O–H stretching vibration and bending of water molecules [24]. The band at ~2915 cm^{-1} can be
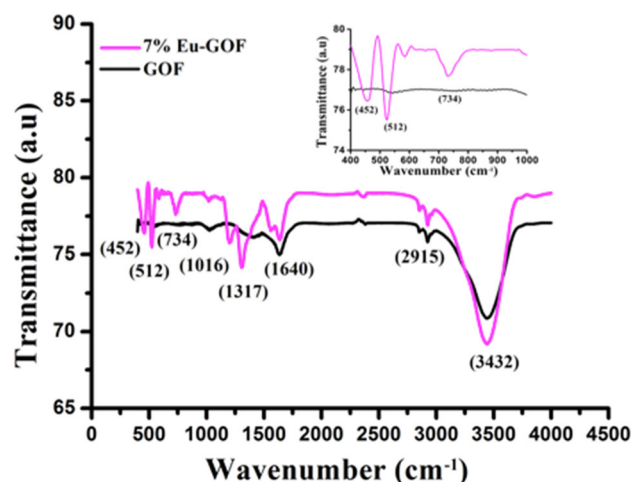

Fig. 5 FTIR spectra of the undoped and 7% Eu^{3+} doped $Gd_4O_3F_6$ nanosystems

attributed to the asymmetric vibration of –CH_2, whereas the dip at ~ 1317 and 1016 cm^{-1} represent characteristic C–O bonding. The low frequency bands at ~ 512 and ~ 452 cm^{-1} have arisen due to the stretching vibration of Gd–O bonds within GOF system [14]. Moreover, the band at ~ 734 cm^{-1} was believed to have appeared due to the C–O stretching vibration. For clarity, the Gd–O vibration related peaks are shown as inset of Fig. 5.

3.4 Manifestation of Raman active modes

Raman spectroscopy is a powerful non-invasive technique based on inelastic scattering of light with molecular systems. In general, IR active modes are not Raman active and, therefore, the latter finds a special place to uncover lattice vibrational characteristics of the material under study. According to the group theory, the normal lattice vibration at the Γ point of the Brillouin zone can be formulated as [25]:

$$\Gamma_{tg} = A_{1g} + 2B_{1g} + 2A_{2u} + 3E_g + 2E_u \tag{5}$$
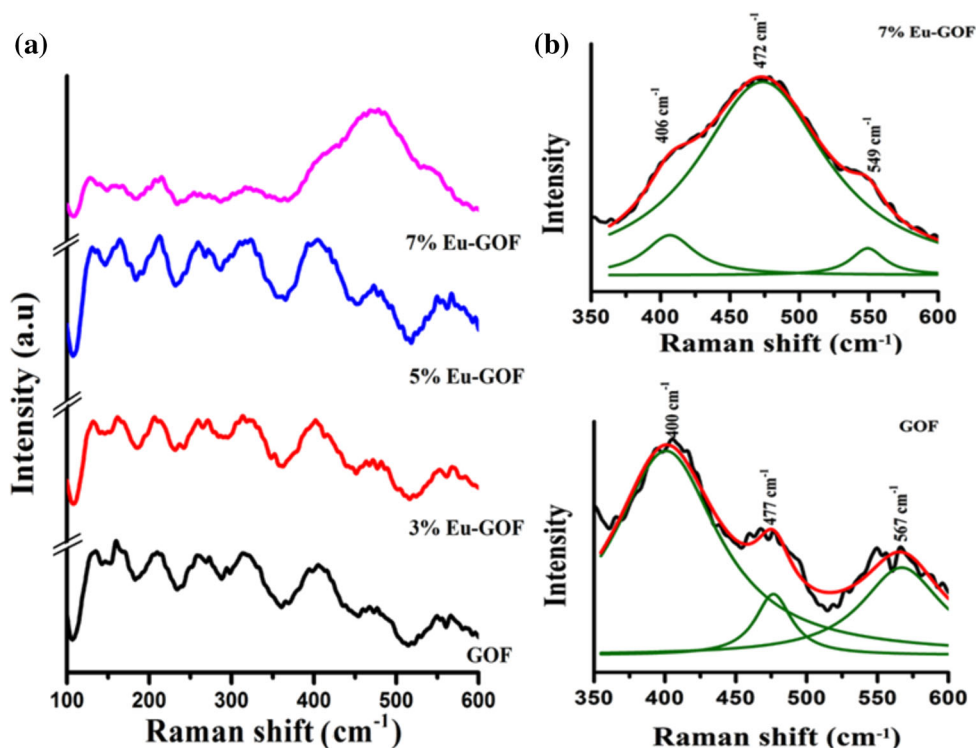
On the basis of group theory selection rules applicable to the RE oxyfluorides, $A_{1g} + 2B_{1g} + 3E_g$ are Raman active, whereas $2A_{2u} + 2E_u$ are IR active modes [25]. The Raman spectra of the undoped and Eu^{3+} doped $Gd_4O_3F_6$ nanoparticles are shown in Fig. 6a. Eight distinct peaks, located at the Raman shift of ~ 128, 165, 210, 266, 319, 407, 477, and 567 cm^{-1} are witnessed in the spectra. The first four peaks (at ~ 128, 165, 210, and 266 cm^{-1}) can be attributed to the movement of heavy atom Gd–Gd pairs as predicted by an earlier group [14]. Similar Raman signature has also been detected for a LaOF system possessing tetragonal crystal structure [25]. Notably, the peak at ~ 477 and 567 cm^{-1} can account for phononic vibration of Gd-O groups [14]. As a general trend, the peak at ~ 477 cm^{-1} tend to shift to higher values with increasing content of Eu^{3+} ions, and with a maxima of 481 cm^{-1} for 5% doping case (not shown). At a 7% Eu^{3+} doping, the peak downshifts to ~ 472 cm^{-1} and gives a much improved signal strength (Fig. 6b). Moreover, the ~ 567 cm^{-1} peak of the undoped GOF system has been shifted to ~ 549 cm^{-1}. At a higher doping level, we anticipate involvement of surface phonon modes exhibited by the symmetrically located dopants in the GOF lattice. In fact, the shifting of the Raman peak toward a higher frequency side can also be due to effective particle size reduction (see also XRD analysis on the trend of crystallite size with doping, Table 1). According to the Heisenberg's uncertainty principle, we have [26]

$$\Delta x \Delta p \geq \hbar/2, \tag{6}$$

where Δx is the particle size, Δp is phonon momentum distribution and $\hbar$ is the reduced Planck's constant. With particle size reduction, phonon confinement and hence phonon energy tend to upsurge significantly. This results in the Raman peak broadening of the scattered phonons according to the law of conservation of momenta [26]. From XRD analysis, the average crystallite size of GOF

Fig. 6 **a** Raman spectra of the undoped and Eu^{3+} doped $Gd_4O_3F_6$ nanosystems, **b** deconvoluted Raman spectra of the undoped and 7% Eu^{3+} doped GOF nanosystems

nanoparticles was found to decrease from ~ 25 to 22 nm with increasing Eu^{3+} doping (from 0 to 5%). Conversely, the 7% Eu^{3+} doped GOF system has a larger crystallite size (~ 26 nm) and much improved Raman band. In semiconductor oxide nanomaterials, the peak shift and line broadening are normally assigned to the crystal defects, oxygen vacancies and inhomogeneous strain [27]. In the present case, the manifested Raman intensity and peak shift in certain wavenumber region can be ascribed to the local distortion of crystal structure of GOF with incorporation Eu^{3+} ions [25]. The symmetric environment provided by the dopants could support confinement of surface optic phonons, resulting in intense Raman band.

4 Conclusions

Nanocrystalline undoped and Eu^{3+} doped $Gd_4O_3F_6$ have been synthesized by a modified Pechini method. The Lotgering factor which accounts for the extent of crystallite orientation along the preferred plane was found to get enhanced for a higher doping level. The orange emission located at ~ 595 nm and red emission at ~ 613 nm are assigned to $^5D_0 \rightarrow {}^7F_1$ and $^5D_0 \rightarrow {}^7F_2$ transitions, respectively. Both J–O parameter and asymmetric ratio tend to fall with increasing Eu^{3+} doping concentration. The electrically driven $^5D_0 \rightarrow {}^7F_2$ transitions being hypersensitive to local environment get suppressed by concentration quenching, as witnessed for 7% Eu^{3+} doping. The low frequency Gd–O bonding has been revealed in the FT-IR spectra between 450 and 550 cm^{-1}. Raman active modes of highly doped GOF samples have revealed intense peaks owing to association of surface optic modes. More works in this direction is necessary to link these modes with non-radiative centers of the nanoparticle systems.

References

1. E. Hosono, S. Fujihara, T. Kimura, Langmuir **20**, 3769 (2004)
2. M. Vijayakumar, S. Selvasekarapandian, T. Gnanasekaran, S. Fujihara, S. Koji, Appl. Surf. Sci. **222**, 125 (2004)
3. M. Vijayakumar, S. Selvasekarapandian, T. Gnanasekaran, S. Fujihara, S. Koji, J. Fluorine Chem. **125**, 1119 (2004)
4. F. Vetrone, R. Naccache, A. Juarranz de la Fuente, F. Sanz-Rodríguez, A. Blazquez-Castro, E. Martin Rodriguez, D. Jaque, J. García Solé, J.A. Capobianco, Nanoscale **2**, 495 (2010)
5. R. Kumar, M. Nyk, T.Y. Ohulchanskyy, C.A. Flask, P.N. Prasad, Adv. Funct. Mater. **19**, 853 (2009)
6. J. Hölsä, B. Piriou, M. Räsänen, Spectrochim. Acta **49A**, 465 (1993)
7. F. Cornacchia, A. Di Lieto, M. Tonelli, Appl. Phys. B **96**, 363 (2009)
8. J. Hölsä, E. Kestilä, J. Alloys Compd. **225**, 89 (1995)
9. E. Antic-Fidancev, J. Hölsä, J.C. Krupa, M. Lastusaari, J. Alloys Compd. **380**, 303 (2004)
10. L. Armelao, G. Bottaro, G. Bruno, M. Losurdo, M. Pascolini, E. Soini, E. Tondello, J. Phys. Chem. C **112**, 14508 (2008)
11. S. Fujihara, S. Koji, T. Kimura, J. Mater. Chem. **14**, 1331 (2004)
12. A. Antuzevics, M. Kemere, R. Ignatans, J. Noncryst, Solids **449**, 29 (2016)
13. T. Passuello, F. Piccinelli, M. Pedroni, M. Bettinelli, F. Mangiarini, R. Naccache, F. Vetrone, J.A. Capobianco, A. Speghini, Opt. Mater. **33**, 643 (2011)
14. T. Grzyb, R.J. Wiglusz, V. Nagirnyi, A. Kotlov, S. Lis, Dalton Trans. **43**, 6925 (2014)
15. J. Hölsä, Acta Chem. Scand. **45**, 583 (1991)
16. Y. Zhang, X. Kang, D. Geng, M. Shang, Y. Wu, X. Li, H. Lian, Z. Cheng, J. Lin, Dalton Trans. **42**, 14140 (2013)
17. R. Li, Y. Liu, N. Zhang, L. Li, L. Liu, Y. Liang, S. Gan, J. Mater. Chem. C **3**, 3928 (2015)
18. P.S. Archana, A. Gupta, M.M. Yusoff, R. Jose, Appl. Phys. Lett. **105**, 153901 (2014)
19. F.K. Lotgering, J. Inorg. Nucl. Chem. **9**, 113 (1959)
20. R.S. Ningthoujam, R. Shukla, R.K. Vatsa, V. Duppel, L. Kienle, A.K. Tyagi, J. Appl. Phys. **105**, 084304 (2009)
21. A.T.M. A. Rahman, K. Vasilev, P. Majewski, J. Coll. Interf. Sci. **354**, 592 (2011)
22. N. Dhananjaya, H. Nagabhushana, B.M. Nagabhushana, B. Rudraswamy, S.C. Sharma, D.V. Sunitha, C. Shivakumara, R.P.S. Chakradhar, Spectrochim. Acta Mol. Biomol. Spectrosc. **96**, 532 (2012)
23. L. Liu, X. Chen, Nanotechnology **18**, 255704 (2007)
24. P. Du, L. Song, J. Xiong, Z. Xi, D. Jin, L. Wang, Nanotechnology **22**, 035602 (2011)
25. J. Hölsä, E. Säilynoja, H. Rahiala, J. Valkonen, Polyhedron **16**, 3421 (1997)
26. H.C. Choi, Y.M. Jung, S.B. Kim, Vib. Spectr. **37**, 33 (2005)
27. S. Sahoo, A.K. Arora, V. Sridharan, J. Phys. Chem. C **113**, 16927 (2009)